STATUS OF THESIS

Title of thesis	An Electromagnetics Water Flooding System With Nanofluid For EOR

I _____ MUHAMMAD KASHIF _____

hereby allow my thesis to be placed at the Information Resource Center (IRC) of UniversitiTeknologi PETRONAS (UTP) with the following conditions:

1. The thesis becomes the property of UTP.

2. The IRC of UTP may make copies of the thesis for academic purposes only.

3. This thesis is classified as

    [✓] Confidential

    [ ] Non-confidential

If this thesis is confidential, please state the reason:

_____

_____

The contents of the thesis will remain confidential for _____ years.

Remarks on disclosure:

_____

_____

                                                            Endorsed by

_____   _____
Signature of Author   Signature of Supervisor

Permanent address: Name of Supervisor

P-1405 Main Bazar Faizabad   Dr. A'fza Shafie

38900 Faisalabad, Pakistan

Date: _____   Date: _____

UNIVERSITI TEKNOLOGI PETRONAS

AN ELECTROMAGNETICS WATER FLOODING SYSTEM WITH NANOFLUID

FOR EOR

By

MUHAMMAD KASHIF

The undersigned certify that they have read, and recommend to the Postgraduate Studies Programme for acceptance of this thesis for the fulfillment of the requirements for the degree stated.

Signature: _____

Main Supervisor: _Dr. A'fza Shafie_____

Signature: _____

Co-Supervisor: Professor Dr. Noorhana Yahya_____

Signature: _____

Co-Supervisor: Associate Professor Dr. Hasnah Mohd Zaid___

Signature: _____

Co-Supervisor: Associate Professor Dr. Nor Hisham Hamid___

Signature: _____

Head of Department: Associate Professor Dr. Rosdiazli Bin Ibrahim

Date: _____

AN ELECTROMAGNETICS WATER FLOODING SYSTEM WITH NANOFLUID

FOR EOR

by

MUHAMMAD KASHIF

A Thesis

Submitted to the Postgraduate Studies Programme

as a Requirement for the Degree of

DOCTOR OF PHILOSOPHY

ELECTRICAL AND ELECTRONIC ENGINEERING

UNIVERSITI TEKNOLOGI PETRONAS

BANDAR SERI ISKANDAR

PERAK

MAY 2014

DECLARATION OF THESIS

Title of thesis	An Electromagnetics Water Flooding System With Nanofluid For EOR

I _____ MUHAMMAD KASHIF _____

hereby declares that the thesis is based on my original work except for quotations and citations which have been duly acknowledged. I also declare that it has not been previously or concurrently submitted for any other degree at UTP or other institutions.

Witnessed by

_____   _____

Signature of Author   Signature of Supervisor

Permanent address: Name of Supervisor

P-1405 Main Bazar Faizabad

38900 Faisalabad, Pakistan   Dr. A'fza Shafie

Date : _____   Date : _____

DEDICATION

To my late father Muhammad Ismail and my mother Asifa Ismail.

ACKNOWLEDGEMENTS

I would like to thank ALLAH Almighty who is the most beneficent and most merciful who gave me the opportunity and health to complete my research.

First of all I would like to thank the person who started it all, Dr. A′fza Shafie, my Supervisor, because she gave me the opportunity to conduct this research under her guidance and supervision. I received motivation in the research area and support from her during my research. Her encouragement, supervision, valuable suggestions and intellectual activities, from preliminary to the concluding level has enabled me to complete everything. I am extremely grateful to my co-supervisors Professor Dr. Noorhana Yahya, Associate Professor Dr. Hasnah Mohd Zaid, and Associate Professor Dr. Nor Hisham Hamid for their keen interest, guidance and moral support.

I want to start saying my gratitude to a very key person in my life who is always there for me no matter what, my father, Muhammad Ismail. A major part of my life; are my father and my mother, these two wonderful persons through all my life have provided the help and support in order for me to achieve my success. Special thanks to my wife Farzana Kashif for her help and patience, for every period I was away. Also I want two say thanks to my brothers and sisters for supporting me.

During my PhD studies in Universiti Teknologi PETRONAS, my friends and my research group members have helped me in my research. I would like to thank all Technicians of Electrical and Electronics Engineering department who had helped me with the laboratory facilities. Finally I would like to extend my appreciation to Universiti Teknologi PETRONAS, Malaysia for the financial and organizational support provided.

ABSTRACT

The major challenge for oil industry is to increase the recovery of oil from the reservoir. EOR by nanofluids induction has been used in water flooding process. This work deals with a new electromagnetics water flooding system using nanofluid for EOR. A simulation on the density of state (DOS) and band structure of zinc oxide (ZnO) and iron oxide (Fe_2O_3) was carried out; it was observed that the band gap value for ZnO is 0.808ev and for Fe_2O_3 is 0.201ev. The percentage difference between the band gap of ZnO and Fe_2O_3 is 301%. For ZnO, Zn 4s state contributes to conduction band and O 2p state contributes to valence band. For Fe_2O_3 valence band is a mixture of O 2p state and the majority is Fe 3d state, while the conduction band consists of Fe 3d state. As Fe_2O_3 has lowest band gap, its dielectric constant is greater than ZnO which has the highest band gap, thus it has the lowest dielectric constant. From the nanoparticles characterization, the XRD results of the ZnO and Fe_2O_3 prepared by sol gel method showed a single phase structure with a [101] and [104] major peaks respectively. From the hysteresis loop, it was observed that Fe_2O_3 sample sintered at 500°C showed a 10.64% high magnetic saturation (Ms) compared to the sample sintered at 400°C. The nanofluids of Fe_2O_3 and ZnO in different concentration were used in this study. The oil recovery through the usage of Fe_2O_3 nanofluid with 0.001wt.% and EM waves generated from the antenna was 71.66% ROIP. The oil recovery through the usage of 0.001wt.% ZnO nanofluid and EM waves was 64.26 % ROIP. This shows that Fe_2O_3 nanofluid in the presence of EM waves has higher polarization due to low band gap, which produced high oil recovery as compared to ZnO which has low polarization due to high band gap and thus lower oil recovery. As the mobility reduction factor of ZnO is greater than Fe_2O_3 therefore the oil recovery due to ZnO is less than iron oxide. The apparent viscosity increases due to the polarization of nanoparticles in the presence of EM waves which increases oil displacement efficiency. This demonstrats that the new electromagnetic water flooding system with nanofluids has potential for application in enhanced oil recovery (EOR).

ABSTRAK

Cabaran besar dalam industri minyak ialah untuk meningkatkan pemulihan minyak dari reserbor. Kerja ini berkaitan dengan satu sistem baru pembanjiran air elektromagnet menggunakan cecair nano untuk EOR Satu simulasi ketumpatan keadaan (DOS) dan struktur jalur Zink oksida (ZnO) dan Besi oksida (Fe_2O_3) telah dijalankan; diperhatikan nilai sela jalur untuk ZnO adalah 0.808ev dan untuk Fe_2O_3 adalah 0.201ev. Untuk ZnO, Zn keadaan 4s menyumbang kepada jalur konduksi dan O keadaan 2p menyumbang kepada jalur valens. Untuk Fe_2O_3, jalur valensnya adalah dari campuran O keadaan 2p dan majoritinya ialah Fe keadaan 3d, manakala jalur konduksinya terdiri dari Fe keadaan 3d. Oleh kerana Fe_2O_3 mempunyai sela jalur terendah, pemalar dielektriknya adalah lebih besar dari ZnO yang mempunyai sela jalur tertinggi, oleh kerana itu ia mempunyai pemalar dielektrik yang terendahBerdasarkan pencirian nanopartikel, keputusan XRD untuk ZnO dan Fe_2O_3 yang disediakan menggunakan kaedah sol gel menunjukkan struktur fasa tunggal dengan puncak utama masing-masing pada [101] dan [104]. Dari gelung histeresis , diperhatikan sampel yang disinter pada 500°C menunjukkan penepuan magnet (Ms) yang tinggi iaitu 10.64% berbanding sampel yang disinter pada 400°C. Cecair nano Fe_2O_3 dan ZnO dalam kepekatan yang berbeza telah digunakan dalam kajian ini Perolehan minyak melalui penggunaan cecair nano Fe_2O_3 pada kepekatan 0.001wt. % dengan gabungan gelombang EM yang ddipancarkan dari antena adalah 71.66 % ROIP. Manakala perolehan minyak melalui penggunaan 0.001wt. % cecair nano ZnO dan gelombang EM ialah 64.26 % ROIP. Ini menunjukkan bahawa di dalam kehadiran gelombang EM, cecair nano Fe_2O_3 mempunyai polarisasi yang lebih tinggi disebabkan oleh sela jalur rendah, yang mana meyumbang kepada perolehan minyak yang tinggi berbanding dengan ZnO yang mempunyai polarisasi rendah, disebabkan oleh sela jalur tinggi, maka perolehan minyak yang lebih rendah. Oleh kerana faktor pengurangan mobiliti ZnO adalah lebih besar dari Fe_2O_3 maka perolehan minyak kerana ZnO adalah kurang dari besi oksida. Peningkatan kelikatan yang ketara diperhatikan kesan polarisasi partikel nano dalam kehadiran gelombang

EM yang mana meningkatkan kecekapan sesaran minyak. Ini menunjukkan bahawa sistem baru pembanjiran air elektromagnet dengan cecair nano mempunyai potensi untuk kegunaan di dalam perolehan minyak tertingkat (EOR).

In compliance with the terms of the Copyright Act 1987 and the IP Policy of the university, the copyright of this thesis has been reassigned by the author to the legal entity of the university,

Institute of Technology PETRONAS Sdn Bhd.

Due acknowledgement shall always be made of the use of any material contained in, or derived from, this thesis.

TABLE OF CONTENT

LIST OF FIGURES

LIST OF TABLES

LIST OF ABBREVIATIONS

2D	Two Dimensional
3D	Three Dimensional
EM	Electromagnetic
IFT	Interfacial tension
OOIP	Original oil in place
ROIP	Residual oil in place
NF	Nanofluid
WF	Water flooding
RF	Radio frequency
MW	Microwave
emf	Electromotive force
SDS	Sodium dedecyl sulfate
CMC	Critical micelle concentration
a.c	Alternating current
DEP	Dielectrophoretic
T_c	Curie temperature
T_N	Neel temperature
FESEM	Field Emission Scanning Electron Microscope
EDX	Energy dispersive X-ray
XRD	X-ray diffraction
HRTEM	High Resolution Transmission Electron Microscope

LIST OF SYMBOLS

ω	Angular frequency
A	Ampere
μ_B	Bohr magneton
σ	Conductivity
H_c	Coercive force
T_c	Curie temperature
N_c	Capillary number
E	Electric field strength
q	Flow rate
f	Frequency
Hz	Hertz
m	Magnetic moment
B	Magnetic flux density
H	Magnetic field strength
mN/m	milli–Newton/meter
T_N	Neel temperature
γ	Propagation constant
ε	Permittivity
μ	Permeability
k	Plane wave number
Φ	Phi
ρ	Resistivity
s	Seconds
δ	Skin depth
T	Tesla
η	Viscosity
χ	Susceptibility
V	Volts
$V_{p\text{-}p}$	Voltage peak to peak

| W | Watt |
| λ | Wavelength |

CHAPTER 1

INTRODUCTION

This chapter mostly emphasis on the motivation of this research work for enhanced oil recovery using nanofluids, and establishes the issues in the current technique of enhanced oil recovery method on which this research work is carried out, and the objectives to be accomplished. Electromagnetic methods used for oil recovery is offshore oil recovery process are briefly described. The thesis organization is also provided at the end of this chapter.

1.1 Enhanced Oil Recovery

The most important problem that the human race face today is energy deficiency, which is due to the fall of oil reserve by conventional oil production fall, unstable oil prices and increase in demand of oil for energy consumption [1]. The price of fuel produced from oil will most likely increase as a result of oil production reduction. The chances of discovering new reservoirs decrease due to a mismatch between production costs and available practical solutions, and economic, environmental, social, and political issues [2, 3]. Enhanced oil recovery (EOR) has become significant in the industry for extracting oil from reservoirs after they have reached their optimal production [3, 4].

1.1.1 Primary Recovery

In primary recovery, the natural pressure of the reservoir due to the presence of gas cap forces the oil out from the reservoir.

1.1.2 Secondary Recovery

In secondary recovery, water flooding or gas injection is used to maintain the reservoir pressure so that more oil can be recovered from the reservoir compared to the primary oil recovery method.

1.1.3 Tertiary Recovery

Tertiary recovery is also known as enhanced oil recovery (EOR). In this method, external fluid is injected into the reservoir which helps to reduce the oil viscosity and improves oil flow. The fluid can be steam, surfactant, polymer or gases which are miscible with oil such as carbon dioxide, air or oxygen.

1.2 Conventional Enhanced Oil Recovery Methods

Enhanced oil recovery processes are used to increase the production of total recoverable oil from the reservoir as compared to conventional methods through which the production declines with time as shown in Figure 1.1. EOR processes generally involve the addition of materials not normally present in the reservoir (polymers, foams, surfactants, solvents, etc.). They are classified as thermal, chemical, or solvent methods. A flow chart of all possible methods for improving oil production is shown in Figure. 1.2.
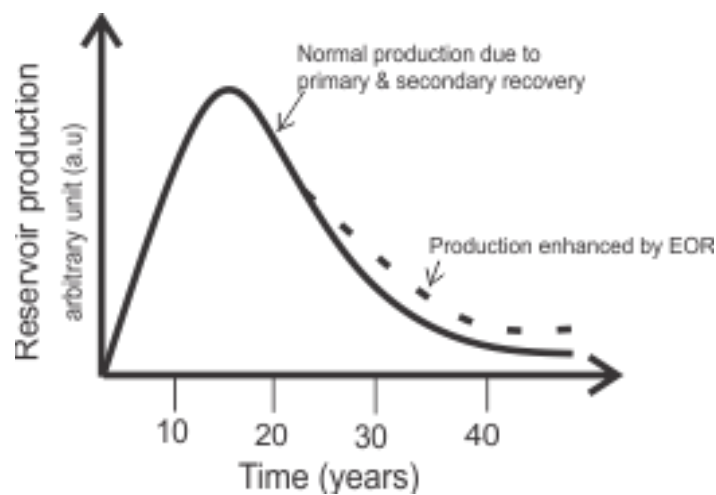
Figure 1.1: Typical production life of reservoir by conventional recovery method [4]
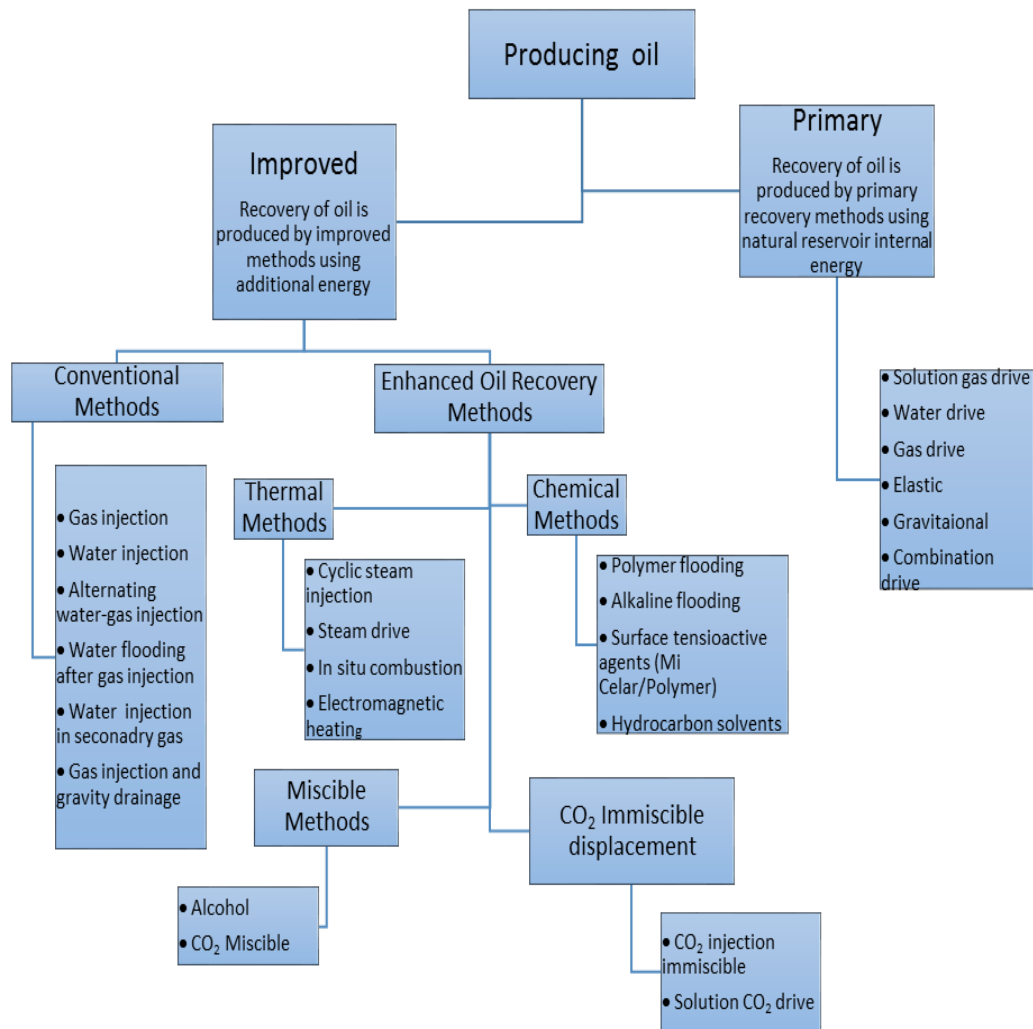
Figure1.2: Flow chart of oil production methods [5]

1.2.1 Thermal EOR

Thermal EOR is a process in which heat plays the main role. Thermal EOR method consists of steam injection, in situ combustion, and cyclic steam injection. In steam injection, heat is injected into a reservoir to reduce the viscosity of oil. The reduction of oil viscosity increases displacement efficiency which increases the oil recovery from the reservoir. There are many other methods for this process such as cyclic steam injection in which steam is first injected followed by injection of hot water, and steam assisted gravity drainage (SAGD) which is used in horizontal wells. However, these

methods will result in failure for deep reservoirs due to excessive heat dissipation. In such situation, generating and injecting steam may be uneconomical due to the tremendous reduction of recovery [6, 7].

1.2.2 Gas Injection EOR

Gas injection process can be miscible and immiscible. In miscible gas injection process, a gas is injected at or above the minimum miscibility pressure (MMP). At the minimum miscibility pressure, the gas becomes miscible with oil. In the immiscible method, gas is injected below the MMP. This injection of gas is used to maintain the reservoir pressure to prevent production cut-off which in turn increases the oil recovery.

In miscible CO_2 process, the interfacial tension between oil and CO_2 is reduced effectively and CO_2 dissolves in oil causing swelling of the oil, and reduces the viscosity of oil. Compressed nitrogen is used in deep and high pressure reservoirs as compared to CO_2. In some large hydrocarbon reserves, gases are used for miscible oil displacement. For immiscible oil, displacement, CO_2, nitrogen, hydrocarbon gases, and flue gases have also been used [6, 7].

1.2.3 Chemical EOR

Chemical EOR process is carried out by adding additives or chemicals to the displacing fluid or to the residual oil to control viscosity and interfacial tension. These chemicals include polymer, surfactant-polymer, and alkaline-surfactant-polymer (ASP). In the polymer flooding method, water-soluble polymers are used for increasing the viscosity of injected water which increases the effective displacement of moderately viscous oil. The addition of surfactant to the polymer solutions reduces the oil-water interfacial tension which increases the oil recovery. In another type of this process, alkaline is added to surfactant-polymer solution. These alkaline can convert some acids in the oil to surfactant which increases oil recovery. Alkaline can also be used to reduce the retention of surfactant by the rock. For all chemical flooding processes, the addition of

a viscosifier (usually a water-soluble polymer) is essential to cause an efficient sweep of the chemicals through the reservoir.

However, there are serious environmental concerns over the use of chemicals in injection water. Therefore, efforts must be carried out through research and development to evaluate these impacts and these effects must be avoided as much as possible. The use of cost effective chemicals is required to reduce the cost of this process and the amount of the surfactant required must be predicted. For offshore fields, large amount of surfactant is required which is a constraint in offshore environment [6, 7].

1.3 Nanofluids in Oil and Gas Industry

Recently there is growing interest on nanoparticles in many applications of the oil and gas industry, such as enhanced oil recovery, reservoir sensing and reservoir intervention. Nanoparticles are very valuable due to their high specific surface area, high adsorption potential and heat conductivity [8].

There are many different types of nanofluids that can be made by using different nanoparticles and base fluid combinations. Some of the most common nanoparticles are alumina oxide (Al_2O_3), copper oxide (CuO), zinc oxide (ZnO), and silica oxide (SiO_2). The most common base fluids used for nanofluids are de-ionized water and ethanol. All nanofluids follow a basic preparation technique. Once the desired weight or volume fraction has been determined, the nanoparticles are added into the base fluid and mixed. Mixing is usually done by ultrasonication to avoid settling of the particles. The amount of time spent on mixing the nanofluids depends on many factors such as the ratio of base to nanoparticles, how long the experiment will last, and the weight or volume fraction used.

In one study, aqueous dispersion of iron-oxide nanorods were used with a non-magnetizable fluid (air, dodecane) [9]. An alternating magnetic field was applied to the aqueous dispersion of iron-oxide nanorods and non-magnetizable fluid. It was observed that the iron-oxide nanorods showed a displacement of the fluid/fluid interface under a

magnetic field. The displacement was larger for large cluster size, larger density difference at the interface of fluid/fluid, higher strength of magnetic field and stronger magnetization [9]. This study has shown some potential of using nanoparticles and electromagnetic field in reservoir for enhanced oil recovery purpose.

A magnetic particle in fluid, when subjected to a magnetic field, will be influenced by several factors. Magnetic particles in a suspension in an external magnetic field experience a force, depending on the magnetization of the particle and the magnitude of the field and gradient of the magnetic field. The particle will move towards the higher field strength and accelerate due to increasing magnetization and gradient of the field [10].

1.4 Electromagnetic Method for Oil Recovery

Electromagnetic energy heats the oil in the reservoir and subsequently moves the oil toward the producing well. For volumetric heating of reservoir, an antenna must be designed such that it provides a uniform electric field in order to achieve complete volumetric heating.

An antenna like exciter can be used for a the uniform electromagnetic heating of oil reservoir due to a uniformed distribution of electric field [11]. A uniform heating can also be obtained from a uniform electric field that can be generated by parallel plates which can achieved by inserting arrays of tubular conductors are inserted in the reservoir region. If alternating voltage is applied to these plates, it will produce a uniform electric field between the plates [12]. In these high frequency electromagnetic methods substantial confinement of electromagnetic energy is required because most of the generated energy can be absorbed by the surrounding materials.

Another problem associated with this method, is that requires a large numbers of boreholes for the antenna separated by distance a quarter of a wavelength in order to get uniform heating. In offshore environment, these problems can be avoided if a horizontal antenna is towed close to the seabed which maximizes the electromagnetic energy transferred from the overburden to the reservoir [11-20].

An array of compact parametric antennas is used on or below the surface of the well and is positioned so that electromagnetic energy is transferred to the oil region. The impartment of electromagnetic energy on oil produces a molecular change in the oil molecules. In this process the electromagnetic energy imparted from the EM antenna on to the oil molecules causes the individual molecules this implies that the smaller molecules agglomerate to form a larger molecule. This molecular change to larger molecules causes a reduction in the oil viscosity without increasing the temperature. The magnetic field component of the electromagnetic waves show sufficient effect on oil molecules to reduce viscosity [21].

A triaxial linear induction antenna can be extended into a hydrocarbon formation and be located within the hydrocarbon formation. An electromagnetic waves signal in the RF region is applied to the linear antenna, which generates a circular magnetic field relative to the radial axis of the linear antenna. The magnetic field produces eddy currents within the hydrocarbon formation, which heats the formation and causes heavy hydrocarbons to flow [22].

To overcome the major challenge of oil recovery oil industry use enhanced oil recovery methods. Enhanced oil recovery by nanofluids induction has been used in water flooding process. The objective of this work is to use metal oxide nanofluids in water flooding enhanced oil recovery application. For this purpose, zinc oxide and iron oxide nanoparticles were synthesized and the nanofluids were prepared using the nanoparticles. These nanofluids in the presence of electromagnetic waves are used for the oil recovery efficiency measurement.

1.5 Problem Statement

In certain oil trapped region in an oil reservoir, the application of electromagnetic waves in that particular region is possible in an effort to recover more oil. However, very little research has been conducted on the use of nanofluids subjected to electromagnetic waves for oil recovery purpose. This is due to the absence of such a system.

1.6 Aim

This work deals with a new electromagnetic water flooding system with nanofluid for enhanced oil recovery. Nanofluid with good magnetic and dielectric properties will be injected into the system and its impact on the recovery will be studied. Simulation of ZnO and Fe_2O_3 to evaluate the performance was conducted for the fundamental properties of metal oxide. A high density electromagnetic waves will be irradiated to activate the nanoparticles.

1.7 Objectives

The objectives of this research are:

1. A simulation of ZnO and Fe_2O_3 nanostructures will be performed for evaluation of density of state (DoS) and band structures.

2. To synthesize and characterize the zinc oxide (ZnO) and iron oxide (Fe_2O_3) nanoparticles for nanofluid preparation.

3. To design a new electromagnetic water flooding system that consists of an EM antenna together with nanofluids.

4. To evaluate the performance of the new system for improved oil recovery in the presence of electromagnetic waves.

1.8 Thesis Overview

This dissertation is organized as follow. Chapter 1 serves as an introduction for the study.

Chapter 2 reviews the relevant issues in electromagnetic oil recovery in general and nanofluids in oil recovery in particular and the use of nanoparticles in its administration. An introduction of an electromagnetic oil recovery is presented.

Chapter 3, includes a theoretical background. It will cover the most important aspects of the theory used for this thesis as well as the basic density of state and band structures of the material, and including some principles of electromagnetic waves.

The simulation parameters, synthesis methods and characterization techniques relevant to nanoparticles are presented in Chapter 4.

Chapter 5 presents simulation results and analyses of zinc oxide and iron oxide. This chapter presents the results of nanoparticles which were prepared using sol gel method. The results of oil recovery using the new system of electromagnetic waves are discussed. This chapter also explains how energy is imparted to the nanoparticles in glass bead sample and also provides an estimate of oil recovery using electromagnetic waves in a water flooding system.

Chapter 6 presents the conclusions of the thesis. The conclusions on the work completed, and the improvements achieved on each structure are expressed. Finally, the future work that can be performed on this subject is discussed.

CHAPTER 2

LITERATURE REVIEW

This chapter presents the literature review related to the study. A comprehensive discussion is delivered on the basic concepts in electromagnetic oil recovery. The application of nanoparticles and nanofluids in oil field is discussed. A review on electromagnetic waves method for oil recovery is also discussed in this chapter. At the end of the chapter, the summary of the chapter is given.

2.1 Conventional Enhanced Oil Recovery Methods

EOR processes usually involve the addition of materials not normally present in the reservoir (polymers, foams, surfactants, solvents, etc.). They are classified as thermal, chemical, or solvent methods.

2.1.1 Thermal EOR

Steam injection is the most widely used method for enhanced oil recovery. The heat of steam or hot water effectively reduces the viscosity of oils which help to make the flow of oil easier as shown in Figure 2.1. An example of steam injection method is cycle steam injection in which steam is first injected, followed by soaking after that oil is produced from the same well as shown in Figure 2.2. Another examples are injection of hot water, steam assisted gravity drainage (SAGD), all of which are more suitable for applications in horizontal wells [6, 7].

Another type of thermal method consists of in situ combustion or "fire flooding", where air or oxygen is injected into the reservoir. In this method, the oxidation of some part of the oil in place produces heat which reduces the viscosity of the remaining oil.

This method also cracks some high-molecular weight hydrocarbons into lighter weight molecules and evaporates some of the lighter hydrocarbons to aid miscible oil displacement [6, 7].
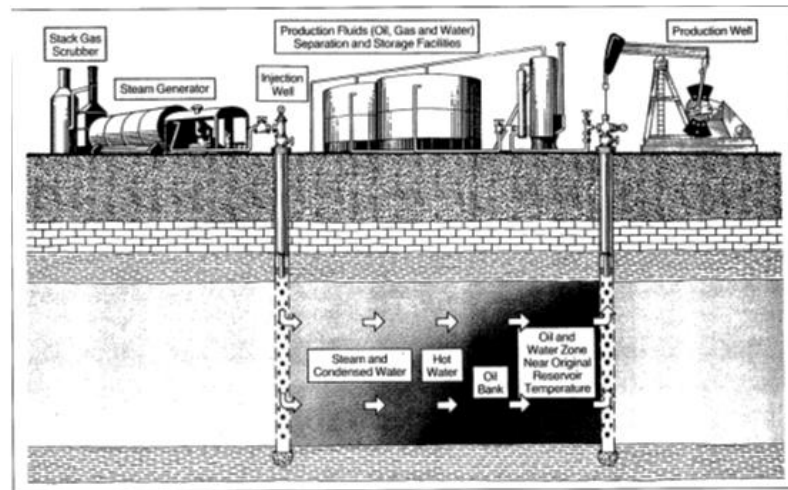
Figure 2.1: Steam injection process [7]
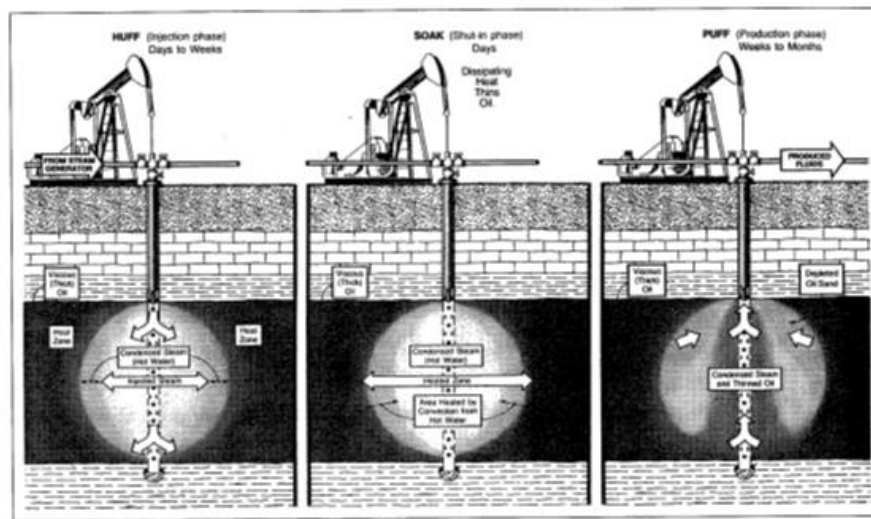
Figure 2.2: Cyclic steam injection process [7]

A pilot test for in-situ thermal method was conducted by [23]. This project was implemented after evaluation of the field and investigating the suitability for this process; about 77% (OIP) original oil in place was recovered.

2.1.2 Gas Injection EOR

Gas injection EOR is either a miscible or an immiscible process. Whether it is a miscible and or an immiscible gas injection method depends on the properties of oil and gas, and also on the temperature-pressure condition of the gas which is to be injected. For miscible gas injection method, supercritical CO_2 is used to move oil from depleted oil reservoirs which contain light oil. The properties of carbon dioxide can change with changes in pressure and temperature therefore, carbon dioxide can take the form of gas, liquid, solid, or supercritical fluid. At or above the critical pressure and temperature, the supercritical CO_2 has the properties of gaseous CO_2 but the density of liquid. In miscible CO_2 injection, the CO_2 injected into the reservoir, mixes with the oil and reduces the interfacial tension between oil and CO_2 effectively as shown in Figure 2.3. The dissolution of CO_2 in oil causes swelling of the oil which reduces the density and viscosity of oil. In deep and high pressure reservoirs, compressed nitrogen is used instead of CO_2. In some large hydrocarbon reserves, gases are used for miscible oil displacement.

For immiscible oil displacement CO_2, nitrogen, hydrocarbon gases, and flue gases have also been used. These gas injections at some extreme conditions are used to maintain pressure inside the reservoir. These displacements have a range of efficiencies which become close to a miscible displacement depending on oil properties, gas composition, and pressure, and temperature. CO_2 injection can also be used in cyclic injection mode, like cyclic steam injection [6, 7].
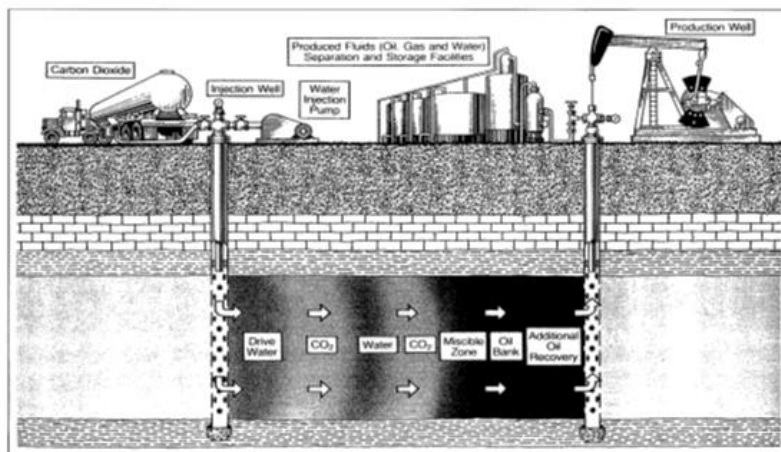
Figure 2.3: CO_2 miscible process [7]

12

An experimental study was conducted by [24] for a carbonate oil reservoir in which CO_2 was injected into a core sample at 4200 psi and 250°F. The oil recovery from this experiment was 97% of the initial oil in place (IOIP). By using CO_2 slug of 0.15, 0.3 and 0.45HCPV, the recovery factor which were got 91.72, 92.78 and 94.85% respectively.

2.1.3 Chemical EOR

Chemical enhanced oil recovery method consists of injection of different chemical compound which can change the petrophysical characteristic of the oil reservoir. There are three famous chemical flooding processes such as polymer, surfactant-polymer, and alkaline-surfactant- polymer (ASP). The chemical flooding method is shown in Figure 2.4. In polymer flooding, water polymers are used to increase the mobility ratio between oil-water fronts. The main characteristics of such polymers is high viscosity at low concentration. The polymers, suitable for enhanced oil recovery applications, are polyacrylamides (PAM), biopolymer, and xanthan gum (XG). In alkaline flooding the pH of injection water is increased in order to increase oil recovery from the reservoir. In alkaline flooding, the chemicals used are sodium carbonate, sodium hydroxide and sodium silicate. Alkaline flooding reduce the interfacial tension of oil-water and alters the rock wettability. In alkaline-surfactant–polymer (ASP) method, alkaline is added to the polymer solution to decreases the amount of surfactant which decrease the surfactant adsorption [6, 7].

An investigation by [25] looked into a sequence of branched alcohol propoxylate sulfate surfactants in enhanced oil recovery application. It was observed that the number of propoxylate groups has substantial effect on the interfacial tension, optimum salinity and adsorption. With the number of propoxy groups, the optimum salinity increases and adsorption decreases. In this study the experiments are performed at diluted surfactant concentrations, both with and without cosurfactants.
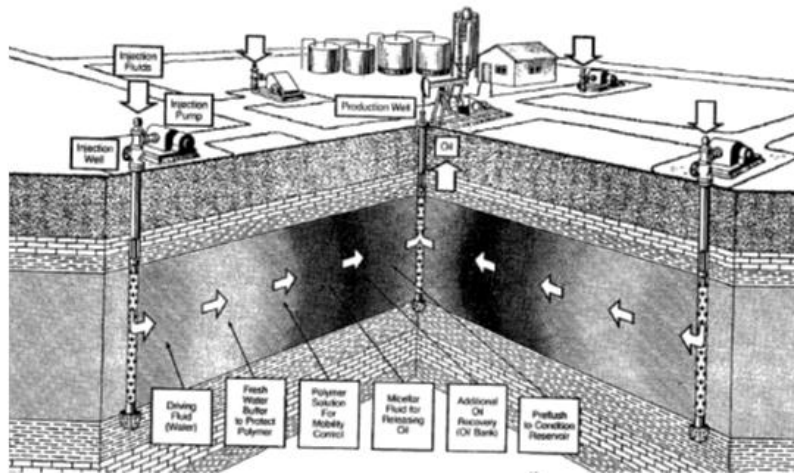
Figure 2.4: Surfactant/polymer flooding process [7]

2.2 Electromagnetic Oil Recovery

Electromagnetic energy can be transferred to oil reservoir in order to reduce the viscosity of oil in an oil reservoir which improves the oil production. This electromagnetic energy heats water in the reservoir due to its dipolar nature and subsequently the heat energy is transferred to oil. This transfer of energy depends on some parameters such as the frequency of electromagnetic waves, temperature, dielectric properties of materials and saturation of brine in the oil reservoir. In EM oil recovery process, a heat transporting fluid as in steam or hot fluid injection process is not required for heating the oil reservoir. This avoids many complications related with generating and transporting a heated fluid [26-34].

Electromagnetic energy can be transferred to oil reservoirs in two ways: high frequency (radio frequency and microwave (RF&MW)) and low frequency. At high frequencies (RF&MW), the electromagnetic waves dielectrically heat the dielectric materials in the oil reservoir. These dielectric materials consist of dipole molecules which tend to align themselves with the electromagnetic waves. Due to the alignment of molecules with the electromagnetic waves, a rotational movement is produced in the dipolar molecules with a velocity proportional to the frequency of the electromagnetic waves. This rotational movement of the dipolar molecules generates of heat from the

14

molecules. In the case of low frequency (50Hz) resistive heating takes place when low-frequency alternating current is used in oil reservoir. Heat dissipation is produced due to ohmic loss ($P_{dissipated} = I^2R$) in the reservoirs. This is the basic theory involved in electromagnetic heating process in oil reservoir before the possible oil recovery is achieved.

2.2.1 Previous Research Work on Electromagnetic Oil Recovery

Several authors have discussed the possibility of using EM method to enhance recovery from oil reservoirs. The application of EM waves can be a real opportunity to recover heavy oil, gas from hydrates or for EOR application in carbonate reservoirs.

Abernethy presented an analytical model for the effect of electromagnetic radiation on the temperature distribution in oil reservoir [35]. Using a mathematical model with steady state condition a comparison of flow performance to the unheated case was discussed. It was concluded that in four weeks of radiation heating, the flow rate could be doubled under various operating conditions. Moreover using 20KW power, the flow rate can be increased from 50% to 300% in different absorption coefficient of the medium.

A feasibility study for electromagnetic irradiation of oil reservoir heating was presented by Franchi by using a numerical simulator [36]. In this study, a simple algorithm was reported which presented the temperature profile of the oil reservoir after electromagnetic irradiation. From this study, it is concluded that the absorption of electromagnetic waves increases the temperature of reservoir and the electromagnetic energy decreases exponentially in a linear, homogenous and dielectric medium. It was further reported that temperature increase is inversely proportional to the area in which irradiation takes place and is directly proportional to time of the irradiation and frequency of electromagnetic waves. The application of this algorithm in a feasibility study of hypothetical reservoir shows that temperature profile depends on electrical conductivities, water saturation and relative permeability.

Gunal investigated the level of thermal alteration of crude oil properties due to electromagnetic waves [28]. The presence of asphaltenes produced some irreversible alterations in oil rheology with oil viscosity reduction due to electromagnetic waves. The viscosity reduction was slow even though the electrical power output was doubled. The study also reported that EM heating can be used in carbonate reservoir as well as crude oil without the presence of water.

Numerical model were developed to study the effect of electromagnetic waves by using some experimental results [37, 38]. Microwave irradiation can eliminate the problem of asphaltene and paraffin precipitation out of the crude oil in horizontal wells. A similar study of microwave irradiation on different concentrations of crude oil, parafin wax, betonite and gypsum showed that temperature change decreases with time and increases the density of the fluid. It is concluded that heterogeneous mixture in oil reservoir can act as a homogeneous mixture, for reservoir fluid in which the crude oil content is about 10% and high water content.

The function of ultrasonic and microwave irradiation on the separation of oil and water from a stable emulsion was investigated by [39]. In this study, the movement of frontal distance due to electromagnetic heating was discussed and it was concluded that this technique has the possibility of increasing oil production when used in wellbore.

The microwave heating of different fluids using water, oil and mixture of water and oil was investigated by [29]. They showed that the mixture of oil and water produced the highest amount of heat as compared to oil alone. The smallest amount of heat produced by the oil alone is due to its low dielectric constant which gave a weak absorption of the microwave. It is concluded that heating oil in the reservoir is a complex phenomenon because reservoir fluid has a mixture of several components. Each component has different physical, electrical and chemical properties. Therefore, the absorption and dielectric properties of fluid as well as the medium play a major role in oil recovery mechanism.

A new method for recovering heavy oil from the bottom water reservoirs was presented by [40]. In this method, an inert gas is injected followed by electromagnetic heating. Although this method was found to be very operational in recovering heavy oil

from bottom water reservoirs, the same method could be applied to oil reservoirs without bottom water.

A new concept of electromagnetic heating in horizontal wells and using gravity stable nitrogen gas was investigated by [41]. This technique overcomes the problem of small heating radius produced due to electromagnetic waves in the case of vertical wells. The horizontal wells allow heating of large area with small heating radius. In this study, the wells were 300m long and 30-50m apart from each other. The oil recovery was dependent of viscosity reduction as the effect of gas injection coupled with EM irradiation, and water flooding following the preheating. Using 120KW/m power, oil recovery of 60% of oil in place was achieved for the oil with the lowest viscosity using gas injection and for the lower viscosity oil, the oil recovery achieved was more than 70% [41].

A model for the electromagnetic heating in the presence of multiple phases was reported by [42]. This model was used to determine the temperature distribution and improvement in production due to electromagnetic heating. Imaginary reservoirs with different fluid and rock properties were used for this study especially where steam injection is difficult to use. A comparison was done for the oil produced by the electromagnetic heating, cold production and steam injection methods. It is concluded that electromagnetic heating increased the production between 5.1 and 19 times more than the cold production. In the case of different reservoir, the thermal efficiency was between 3 and 9. Thin pay zone reservoir gave the largest efficiency and extra heavy oil reservoir gave the smallest efficiency. In comparison to steam injection, electromagnetic method produces more oil with the same power consumption [42].

Some applications of electromagnetic waves heating have been implemented in the fields. A field test at North Midway field, United states, a test well was located where the diatomite interval is relatively homogeneous, starting at 500 ft. A 13.56 MHz generator with 25kW power was used in a mobile set up of RF heating system. The RF applicator used was 25ft in length and placed at a depth of 620 ft. After 40 hours of RF heating, the temperature measured at 605 ft depth, rose to approximately 220°F (approximately 130°F above the formation temperature of 90°F) [43].

17

In a low frequency field test at Rio Panan field, Brazil it was observed that after 70 days of applying electrical energy of 30kW across neighboring producing wells (328 ft apart) , the production increased from 1.2 Bbls/day to 10Bbls/day [44].

Field tests in tar sands of Utah showed that 40 and 75 kW RF power of 13.56 MHz input to the tar sand increased the temperatures from about 120°C to 200°C. Field tests in the oil shale's of Utah showed that a 40 kW RF transmitter at a frequency of 13.56 MHz was used. The RF power used was in the range of 5 kW to 20 kW and it was observed that the temperature increased from 340°C to 400°C [45].

2.3 Antenna for Electromagnetics Oil Recovery

In the current practice of electromagnetic method, dipole antennas are used in RF band of electromagnetic waves. These antennas are inserted in a well close to the producing well. When these antennas obtain energies from the power source, they radiate electromagnetic fields into the oil reservoir. At these frequencies, the intensity of the electromagnetic fields drops rapidly as the distance from the antennas increases. As a result non uniform heating is produced in the reservoirs.

For uniform volumetric heating of reservoir, an antenna must be designed such that it provides uniform electromagnetic fields so that uniform volumetric heating can be obtained. Uniform electromagnetic heating of the oil reservoir can be obtained by using an antenna like exciter which produces uniform distribution of the electric field [11]. Another method to obtain uniform heating is by using parallel plates; uniform distribution of electric field can be produced when alternating voltage is applied to the plates. These parallel plates can be realized when an array of tubular conductors is inserted in the formation region [12] .

In these current methods, a considerable amount of electromagnetic energy is required in confined reservoir region but most of the energy will be absorbed by the neighbouring medium. Therefore, the current methods result in non-uniform temperature distribution and inefficiency due to overheating of some reservoir regions.

Furthermore, these localized heating converts water into steam which negatively affect the propagation of electromagnetic waves. A problem associated with these methods is that it requires a large number of boreholes for the antenna, which should be positioned at a distance of a quarter of a wavelength in order to get uniform heating. Although RF heating has been used for heating oil reservoir in the past, there remains a need for improvement. Any new method needs to address the issue of producing uniform heat, in addition to avoiding the substantial need for large number of boreholes for antennas.

Currently in high frequency electromagnetic wave heating an antenna is inserted in a well close to the producing well. Electromagnetic energy heats the oil in the reservoir and improves the oil flow toward the production well. For volumetric heating of reservoir, an antenna must be designed such that it provides a uniform electric field so as to achieve complete volumetric heating.   The uniform electromagnetic heating of the oil reservoir is due to a uniform distribution of electric field provided by the antenna [12].

It is reported by [12] that if parallel plates are used, uniform heating can be obtained from a uniform distribution of electric field in the reservoir region. Alternating voltage is applied to the plates to produce uniform electric fields between the plates.

It was investigated by [21] that electromagnetic energy is transferred to the oil region by an array of compact parametric antennas when they are used on or below the surface of the well. A molecular change in the oil molecules is produced due to the electromagnetic energy. In this method the electromagnetic energy transferred from the antenna to the oil molecules causes the individual molecule to join together. The viscosity of the oil is reduces due to this molecular change to larger molecules without increasing the temperature. The magnetic field exhibits favorable effect on the oil particles to reduce viscosity.

It is reported by [22] that an electromagnetic wave signal in the RF region is applied to a triaxial linear antenna, which produces a circular magnetic field relative to the radial axis of the linear antenna. Eddy currents are produced due to the magnetic field

within the hydrocarbon formation, which heats the formation and causes heavy hydrocarbons to flow.

Table 2.1: A summary of earlier studies by different authors as discussed in the literature review on EOR

Researchers	Parameters	Results
Abernethy [35]	• An analytical model for the electromagnetic radiation effects on the temperature distribution of the oil reservoir.	• 4 weeks of radiation heating flow rate 2 times. • Using 20KW, power flow rate can be increased 50% to 300% in different absorption coefficient of the medium.
Franchi [36]	• A simple algorithm which accounts the temperature profile of the oil reservoir after electromagnetic irradiation.	• Power of generator 60KW • For a reservoir at 1000 ft. of depth, the power loss will be about 27% of the surface power.

Gunal [28]	• Frequency 2000MHz and 20KHz • Power 250W • 3%, 8% and 13% concentrations of asphaltene.	• 8% asphaltene causes more loss to the crude oil rheology than does 13% asphaltene.
Bjorndalen [38]	• Using microwave or ultrasonic irradiation • Different concentration of crude oil, paraffin wax, betonite and gypsum • Crude oil with 0%, 10%, 100%.	• The 100% crude oil • A very steady linear rise with no alternating trend • Samples with water (0%, 1% and 10%) becomes almost horizontal after 60s.
Soliman [39]	• Separation of oil and water from a stable emulsion function with ultrasonic and microwave irradiation.	• Energy absorbed at the front 38% • 62% energy dissipates ahead of the front.

Chhetri [29]	• Investigated microwave heating of different fluids using water, oil and a mixture of water and oil.	• The lowest heat produced in the oil alone is due to its low dielectric constant which gives weak absorption of microwave.
Islam and Chakma [40]	• Oil/water-zone thickness ratio, • oil viscosity • horizontal-well placement • inert-gas injection rate • Production-well temperature.	• 77 % oil in place (OIP) in the presence of a bottom water reservoir.
Islam [41]	• Electromagnetic heating in horizontal wells combined with gravity stable inert gas • Wells 300m long and 30-50m separated from each other.	• 120KW/m power oil recovery of 60% of oil in place was achieved for oil of the lowest viscosity. • With gas injection and oil with lower viscosity, the oil recovery

		• achieved was more than 70%.
Kasevich [43]	• 13.56 MHz generator with 25kW power. • The RF applicator used was 25 feet long and placed at a depth of 620 feet.	• 40 hours of RF heating, temperature measured at 605 feet depth, rose to approximately 220°F (approximately 130°F above formation temperature of 90°F).
Pizarro [44]	• 70 days of applying electrical energy of 30kW.	• Production increased from 1.2 Bbls/day to 10Bbls/day
Bridges [45]	• 40 and 75 kW RF power. • 13.56 MHz	• Increased the temperature from about 120°C to 200°C.

2.4 Nanoparticles for Enhanced Oil Recovery

Recently, the oil and gas industry has shown great interest on nanoparticles in many applications of the industry such as enhanced oil recovery, reservoir sensing and intervention. Nanoparticles are very valuable due to their high specific surface area, high adsorption potential and heat conductivity [8]. The first requirement for the application of nanoparticles in oil reservoir is the transport of nanoparticles through reservoir rock.

A transport study of Si-Zn-DTPMP nanoparticles in calcite and sandstone porous media exhibited a reasonable migration in these porous media and this migration can be improved by pre-flushing the media with a surfactant solution [46].

A study for long-standing dispersion stability and morphology of surface-treated iron oxide nanoparticle was conducted by [47]. It is concluded that these nanoparticles can be transported long distance with the smallest retention in a given reservoir rock. Using nanoparticles, stabilized emulsions can be produced which give the smallest retention and easy transport through the reservoir rock. In the extreme conditions of reservoirs the irreversible adsorption of nanoparticles makes nanoparticle stabilized emulsions highly stable [48].

Cross-linked polymeric nanoparticles were prepared and characterized for enhanced oil recovery application by [49]. Theoretical study of lipophobic and hydrophilic polysilicon (LHP) nanoparticles was conducted to analyze the wettability changes of porous media for enhanced oil recovery. Numerical simulations were conducted for nanoparticles distribution, retention, and porosity reduction due to nanoparticles, absolute permeability and oil recovery performance. It is concluded that LHP concentration from 0.02 to 0.03 is suitable for enhance oil recovery [50].

An experimental study was conducted by [51] for the lipophobic and hydrophilic polysilicon (LHP) nanoparticles to testify the wettability changes of porous media and nanoparticles retention. A mathematical model was developed for transport study of nanoparticles through porous media and it was observed that water-phase permeability

of sandstones increased from 1.6 to 2.1 times of their original values but there was a reduction in absolute permeability due to nanoparticles retention [51].

The effect of alternating magnetic field on aqueous dispersion of iron-oxide nanorods and non-magnetizable fluid was studied by [9]. It was investigated that iron-oxide nanorods showed a displacement at the fluid/fluid interface under a magnetic field. This displacement depend on cluster size, density difference at the interface of fluid/fluid, strength of magnetic field and stronger magnetization. This study shows that there is potential of using nanoparticles and electromagnetic field in oil reservoir for oil recovery.

Table 2.2: A summary of the studies on nanoparticles in EOR

Researchers	Parameters	Results
Zhang [46]	• Si-Zn-DTPMP nanoparticles in calcite and sandstone porous media.	• Exhibited a reasonable migration in these porous media.
Yu [47]	• Nanoparticle loading ranges. • Concentrated (10 wt %) and dilute (0.1 wt %).	• 95% of the injected particles extracted in post-flush.
Manasir [49]	• Cross-linked polymeric nanoparticles.	Stabilization of microgelsdepends on the factors • Adding ionic surfactant to uncharged particles • The amount of charged groups in the polymer, and/or pH.

Ju [50]	• Lipophobic and hydrophilic polysilicon (LHP) nanoparticles.	• LHP concentration from 0.02 to 0.03. • Wettability changes of porous media for enhanced oil recovery.
Ju [51]	An experimental study • lipophobic and hydrophilic polysilicon (LHP) nanoparticles. • Wettability changes of porous media and nanoparticles retention.	• Water-phase permeabilities in sandstones increased from 1.6 to 2.1 times of their original values. • Reduction in absolute permeability due to nanoparticles retention.
Prodanovic [9]	• Aqueous dispersion of iron-oxide nanorods • Alternating magnetic field.	• Iron-oxide nanorods shows a displacement at the fluid/fluid interface under a magnetic field.

2.5 Nanofluids

Nanofluids are made by using different nanoparticles and base fluid combinations such as alumina oxide (Al_2O_3), copper oxide (CuO), zinc oxide (ZnO) and iron oxide.

All nanofluids follow a basic preparation technique. Once the desired weight or volume fraction has been determined, the nanoparticles are added into the base fluid and mixed. Mixing is usually done by ultrasonication to avoid settling of the particles. The amount of time spent mixing the nanofluids depends on many factors such as the ratio of base to nanoparticles, how long the experiment will last, and the weight or

volume fraction used. The results of the first research on nanofluids conducted by Choi showed that these new nanofluids had tremendous heat transfer applications because of their improved heat transfer properties [52, 53]. A lot of research has gone into finding exactly why nanoparticles have such enhancement on heat transfer properties of the fluid but no definitive answers have been found. Jang [53] and Chon [54] have theorized that micro convection induced by Brownian motion of the nanoparticles is one of the driving mechanisms behind the thermal enhancements of nanofluids. The random motion of the nanoparticles would create a source of fluid convection that would increase the thermal properties of the base fluid. Most researchers agree that nanofluids have been shown experimentally to have better heat transfer properties than the base fluid alone. Another advantage of utilizing nanofluids is that at the nano-scale, the particles are small enough to stay in suspension, under the right conditions they can stay in suspension indefinitely, effectively eliminating sedimentation, clumping, and clogging.

It is reported by [55] that the nanoparticles of ZnO nanofluid with average size of 10 nm (volume fraction 1.5%) in ethanol shows an unusual frequency dependent enhancement of the heat transport parameter. The enhancement is considerable at low frequency. The enhancement also depends on the concentration of ZnO and temperature. It is suggested that this frequency dependence is due to local aggregation.

The convective heat transfer of ZnO/water nanofluid was investigated experimentally by [56]; the results give rise the effect of two shapes of nanoparticles. Heat transfer coefficients and pressure drop were measured at two different temperatures (20, 50°C) and various flow rates (200 < Re < 15,000). By using thermal conductivity and viscosity measurement the Reynolds and Nusselt numbers were obtained.

CuO nanofluid was synthesized by [57] through microwave irradiation in which an unstable $Cu(OH)_2$ precursor is transferred to CuO in water under an ultrasonic vibration. In this study, the effect of different type of precursor, ultrasonic vibration, microwave irradiation, and dispersant were also discussed, and the thermal conductivity of CuO nanofluid was studied. It was observed that the synthesized CuO nanofluid had a higher thermal conductivity than those synthesized by dispersing method.

CuO nanoparticles was synthesized by [58] and it was observed that the average diameter of the nanoparticles was 8 nm by a simple precipitation technique. The thermal properties of the suspensions were also investigated. From the experimental results it was observed that the nanoparticle size, polydispersity, cluster size, and the volume fraction of the particles have a substantial effect on thermal conductivity.

It is investigated by [59] the preparation of several suspensions containing Al_2O_3 nanoparticles with specific surface areas in a range of 5–124 m^2g^{-1}. Thermal conductivities were studied by using a transient hot-wire method. The results showed that thermal conductivity substantially increased with increasing volume fraction of Al_2O_3 nanoparticles. This increase in conductivity was also observed with increasing pH difference between the aqueous suspension and the isoelectric point of Al_2O_3 particle.

An experimental investigation was carried out by [60] on iron oxide (Fe_2O_3) nanofluid consisting of water in concentrations ranging between 5 and 20%. In this study thermal conductivity and dynamic viscosity of these fluids were measured. Zeta potential and pH measurements were used to observe the stability of the nanofluids. The mean nanoparticle diameters were obtained by a dynamic light scattering (DLS) technique. It was observed that thermal conductivity and viscosity of these nanofluids increased with temperature and particles concentration.

A study on the thermal conductivities of iron oxide (Fe_3O_4) nanofluids with average particles size of 8 nm stabilized with a monolayer of surfactant consisting of aqueous and nonaqueous stable nanofluids was conducted by [61]. Iron oxide (Fe_3O_4) nanoparticles were synthesized by a coprecipitation technique. It was observed that the thermal conductivity of aqueous nanofluids increased with temperature but it decreased with nonaqueous nanofluids.

Table 2.3: A summary of the studies on nanofluids

Researchers	Parameters	Results
Neogy [55]	- ZnO nanofluid. - Particle size of average size of 10 nm (volume fraction 1.5%) in ethanol.	- An unusual frequency dependent enhancement of the heat transport parameter. - The enhancement depends on the concentration of ZnO and temperature.
Ferrouillat [56]	- ZnO/water nanofluid. - Heat transfer coefficients and pressure drop were measured at two different temperatures (20, 50°C) and various flow rates (200 < Re < 15,000).	Using thermal conductivity and viscosity measurement the Reynolds and Nusselt numbers were obtained.
Zhu [57]	- CuO nanofluid. - Synthesized by microwave irradiation.	The synthesized CuO nanofluid has a higher thermal conductivity than those synthesized by dispersing method.

Karthikeyan [58]	• CuO nanofluid • Average diameter 8 nm.	• Nanoparticle size, polydispersity, cluster size, and the volume fraction of the particles have a substantial effect on thermal conductivity.
Xie [59]	• Al_2O_3 nanofluid. • Specific surface areas in a range of $5–124\ m^2g^{-1}$.	• Thermal conductivity substantially increase with increasing the volume fraction of Al_2O_3 nanoparticles. • Increase in conductivity is also observed with increasing difference between the pH values of aqueous suspension and the isoelectric point of Al_2O_3 particle.
Colla [60]	• Iron oxide (Fe_2O_3) nanofluid in water. • Concentrations ranging between 5 and 20%.	• Thermal conductivity and viscosity of these nanofluids increased with temperature and particles concentration.

Shima [61]	• Iron oxide (Fe_3O_4) nanofluids. • Average particles size of 8 nm. • Synthesized by coprecipitation technique.	• Thermal conductivity of aqueous nanofluids increases with temperature but it decreases with nonaqueous nanofluids.

2.6 Summary

Oil recovery in offshore oil reservoirs is inhibited by reservoir lithology, as well as by surface facilities and environmental regulations. The availability of oil recovery choices in offshore fields is more restricted than the onshore oil reservoirs. Deep reservoir will result in the failure of thermal method due to excessive heat dissipation. In this situation, generating and injecting steam may be uneconomical due to the tremendous reduction of recovery. An alternative method to solve these problems is the electromagnetic method. But this method requires a large number of boreholes for the antenna. Nanoparticles are used in the oil and gas industry for various applications such as enhanced oil recovery, reservoir sensing and intervention. One potential alternative to electromagnetic method for offshore environment is the application of antenna near the seabed, which can provide strong electromagnetic waves vertically downward to the oil reservoir as well as for injection of the nanofluid. The injected nanofluid will interact with the electromagnetic waves to produce more oil.

CHAPTER 3

THEORETICAL BACKGROUND

This section covers the theoretical background related to this research work. This chapter largely emphasizes on the density of state and band structure of the materials. A discussion on interfacial tension measurement is also included. Dielectric and magnetic nanoparticles in the electric and magnetic fields are also discussed. Electromagnetic wave propagation is also briefly described.

3.1 Density of State

The number of quantum states per unit energy are called density of state. In a particular system it represents densely packed quantum states. It is denoted by $g(E)$ [62-68].

Let's suppose we take the expression $g(E)dE$. The number of states between E and dE can be obtained by integrating the density of the quantum states over a range of energy

$$N(E) = \int_{E}^{\Delta E} g(E)dE$$

(3.1)

The number of quantum states is used for evaluating the optical properties of materials. The energy of a particle by the Schrodinger equation is given by

$$E = \frac{k^2 \hbar^2}{2m}$$

(3.2)

Where k represents the momentum of the wave. The energy of a particle is represented by

$$E = \frac{1}{2}mv^2 = \frac{m^2 v^2}{2m} = \frac{p^2}{2m}$$

(3.3)

Comparing these two equations we get

$$E = \frac{k^2\hbar^2}{2m} = \frac{p^2}{2m} \rightarrow k = \frac{p}{\hbar} \tag{3.4}$$

Due to vector property of the momentum it is represented with its components in the x, y, and z directions. Therefore, the components of k are k_x, k_y, and k_z. Energy is represented as;

$$E = \frac{|k|^2\,\hbar^2}{2m} \tag{3.5}$$

Thus, the total energy in three dimensional system is given by

$$E = \frac{\hbar^2}{2m}\left(k_x^2 + k_y^2 + k_z^2\right) \tag{3.6}$$

The wave function of an electron in a potential well is given by

$$\psi(x) = A\cos(kx) + B\sin(kx)$$
where:
$$k = \frac{n\pi}{a} \tag{3.7}$$

where a represents the width of the potential barrier, n is odd integer for the cosine function and n is even for the sine function.

The components of k are represented in each coordinate as;

$$k_x = \frac{n_x\pi}{a},\ k_y = \frac{n_y\pi}{a},\ \text{and}\ k_z = \frac{n_z\pi}{a} \tag{3.8}$$

Therefore at the regular intervals of $\frac{\pi}{a}$ the wave function is valid.

The density of these states can be obtained if we know the unit cell and its volume. A lattice is obtained by repeating the unit cell which is the smallest shape of the lattice. For the simplest unit cell we take a cube whose volume is

$$V_0 = \left(\frac{\pi}{a}\right)^3 \tag{3.9}$$

As the density of state represents the number of states in the range of E and $E+dE$. Therefore, in k-space, the range is represented by k and $k+dk$. In three dimensions, k

33

denotes the radius of a sphere in k-space and dk represents the thickness of the sphere. Therefore, a shell is formed which possess a certain amount of quantum states in an infinitesimal range. If we consider a sphere as k is directly related to E therefore equal energy can be considered on all points on the sphere. Since we are interested to find the density of states in an infinitesimal range of energy, the boundaries of the interval are essentially at equal energies.

The volume of the shell is given by,

$$V = 4\pi k^2 dk \tag{3.10}$$

Instead of this, the volume can be obtained by taking the difference of the volume of the inner sphere and the volume of the outer sphere (of radius $k + dk$).

$$\begin{aligned} V &= \frac{4}{3}\pi (k + dk)^3 - \frac{4}{3}\pi (k)^3 \\ &= \frac{4}{3}\pi (k^3 + 3k^2 dk + 3k dk^2 + dk^3 - k^3) \end{aligned} \tag{3.11}$$

Ignoring dk^2 and dk^3, the volume is given by

$$= \frac{4}{3}\pi (3k^2 dk) = 4\pi k^2 dk \tag{3.12}$$

The wave function is valid for all positive values of k_x, k_y, and k_z. So the whole volume of shell is needless. For all positive values of k_x, k_y, and k_z the volume of shell is represented by,

$$\begin{aligned} V &= \left(\frac{1}{8}\right) 4\pi k^2 dk \\ &= \frac{1}{2}\pi k^2 dk \end{aligned} \tag{3.13}$$

The density of state or the number of quantum states in a range of dk is obtained by dividing the volume of the shell and the volume of unit cell.

$$g(k)dk = (2)\frac{\frac{1}{2}\pi k^2 dk}{\left(\frac{\pi}{a}\right)^3}$$

$$= \frac{a^3}{\pi^2}k^2 dk \tag{3.14}$$

As we know

$$k = \sqrt{\frac{2mE}{\hbar^2}}$$

$$dk = \frac{1}{2}\left(\frac{2m}{\hbar^2}\right)\left(\frac{2mE}{\hbar^2}\right)^{-\frac{1}{2}}dE$$

$$= \frac{m}{\hbar^2}\left(\frac{2mE}{\hbar^2}\right)^{-\frac{1}{2}}dE \tag{3.15}$$

Using the equation (3.15) the density of states in the form of energy is given by

$$(3.16)$$

$$g(k)dk = \frac{a^3}{\pi^2}k^2 dk$$

$$g(E)dE = \frac{a^3 m}{\pi^2 \hbar^2}\left(\frac{2mE}{\hbar^2}\right)\left(\frac{2mE}{\hbar^2}\right)^{-\frac{1}{2}}dE$$

$$g(E)dE = \frac{a^3}{\pi^2}\frac{2\left(2^{-\frac{1}{2}}\right)m^2\left(m^{-\frac{1}{2}}\right)E\left(E^{-\frac{1}{2}}\right)}{\hbar^4\hbar^{-1}}dE$$

$$(3.17)$$

$$= \frac{a^3}{2\pi^2}\frac{2^2\left(2^{-\frac{1}{2}}\right)m^{\frac{3}{2}}}{\hbar^3}\sqrt{E}dE$$

$$g(E)dE = \frac{a^3}{2\pi^2}\left(\frac{2m}{\hbar^2}\right)^{\frac{3}{2}}\sqrt{E}dE \tag{3.18}$$

3.2 Band Structures

In an isolated atom, electrons occupy different orbitals. These orbitals are discrete set of energy levels. If many atoms come close to each other to form a molecule the atomic orbitals split and generate a number of orbitals which are equal to the number of atoms. If a large number of atoms come close to each other to form a solid, the atomic orbitals

become very large because the difference in energy levels becomes very small. Due to this small difference in energy levels, these discrete energy levels become a continuous band of energy. There exist some energy levels which consist of no orbitals even though a large number of atoms come close; these energy levels form band gaps. If the material is in nanoscale crystals, located in the middle a molecule and in solid form, the change of discrete energy levels into continuous bands in this regime can be studied. The electronic and optical properties of a nanoscale material can be studied by understanding of its energy level structure [62-68].

Band structure is very important to the study of relationship between energy levels and periodicity of the crystal lattice in bulk crystalline solid. The band structure represents quantized energy levels that an electron is 'allowed' or 'forbidden' to occupy.

The energy values E of such a system is given by the Schrödinger equation

$$E\psi(r) = \left(-\frac{h^2}{2m}\nabla^2 + V(r)\right)\psi(r)$$
(3.19)

Where ∇^2 is the Laplacian operator, $V(r)$ is the potential energy and $\psi(r)$ is the wave function. Bloch waves are solutions (eigen functions) for the energy levels (eigen values) which are obtained from the periodicity of crystal lattice and is represented by

$$\psi_{nk}(r) = e^{ik\cdot r}u_{nk}(r)$$
(3.20)

Where k is the wave vector and represents the direction of motion of the electron in the crystal, and n denotes the band index and shows the number of energy bands. Bloch function $u_{nk}(r)$ represents the periodic potential of the crystal lattice. A Bloch wave contains a plane wave envelope function modulated by a periodic Bloch function $u_{nk}(r)$. The Born–von Karman boundary conditions for periodic systems are given by,

$$\psi(r + N_i a_i) = \psi(r)$$
(3.21)

36

Where a is the primitive lattice vector and N is any integer, k can have quantized values and is given by

$$k = \frac{2\pi n}{Na} \quad n = 1, 2, 3, \ldots \quad (3.22)$$

The effective mass approximation can be used to study effect of the lattice potentials in the band structure. When a particle is moving in the crystal field its relative mass is called effective mass m*. Electrons and holes in a crystal react to electric and magnetic field similar to free particles in free space but with a different mass. If there is no interaction with other electrons on free particles its Hamiltonian is represented as

$$\hat{H} = \left(-\frac{\hbar^2}{2m}\nabla^2 + V(r) \right) = -\frac{\hbar^2}{2m*}\nabla^2 \quad (3.23)$$

Where $V(r)$ represents the average potential the adjacent employs on the electron and is interpreted within the effective mass m*. Considering the effective mass for electrons the effect of the lattice potential can be deliberated through changes in momentum as given by the expression,

$$E = \frac{p^2}{2m*} = \frac{\hbar^2 k^2}{2m*} \quad (3.24)$$

In a real crystal, the condition is very complicated. The optical properties are obtained by the energy levels around the Fermi level (band gap). A parabolic band profile is obtained due to extremes of the valence and conduction bands as shown in Figure 3.1. There are numerous theories which can be used to predict the complete band structure in crystals such as Nearly–free electron approximation and the Tight–Binding Model.
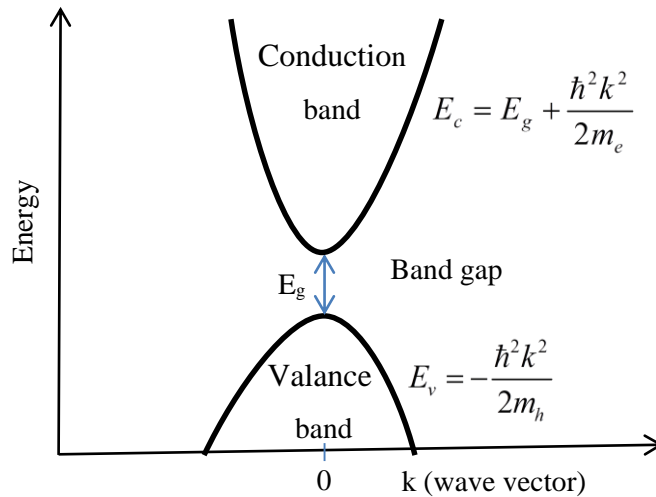
Figure 3.1: Single particle energy states as a function of the wave vector k

3.3 Crystal Structure of Zinc Oxide (ZnO)

Zinc oxide is an oxide of group II metal Zinc that belongs to P63mc space group. Zinc is in the transition metal row which has 3d10 moments and hence it does not have any unpaired electron orbiting around the nucleus [69, 70]. Zinc oxide is a semiconductor material with a hexagonal wurtzite crystal structure [71] as shown in Figure 3.2. It has been reported that ZnO has a very large exciton binding energy of 60 meV [72] at room temperature which makes it a promising candidate for short wavelength Light Emitting Diode (LED) [73].
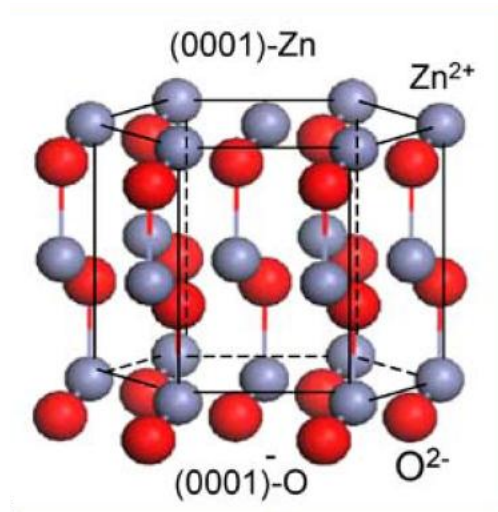
Figure 3.2: The wurtzite structure model of ZnO [71]

3.4 Crystal Structure of Iron Oxide (Fe_2O_3)

The most stable form of iron oxide is Fe_2O_3 and it is the most common iron oxide mineral in nature. Pauling and Hendricks in 1925 discovered the crystal structure of Fe_2O_3. Its structure is similar to corundum and has a rhombohedrally centered hexagonal unit cell [74, 75] as shown in Figure 3.3. The structure of Fe_2O_3 is close-packed oxygen lattice in which two-thirds of the octahedral sites are occupied by Fe^{3+} ions. The space group of Fe_2O_3 is $R\bar{3}c$ six formula units per unit cell and its lattice parameters are $a = 5.0356$ Å, $c=13.7489$ Å. Fe_2O_3 exhibits the magnetic properties of ferromagnetism as well as antiferromagnetism below the Néel temperature of 950 K. At the Morin temperature (TM) around 260 K, Fe_2O_3 is weakly ferrimagnetic [76, 77].
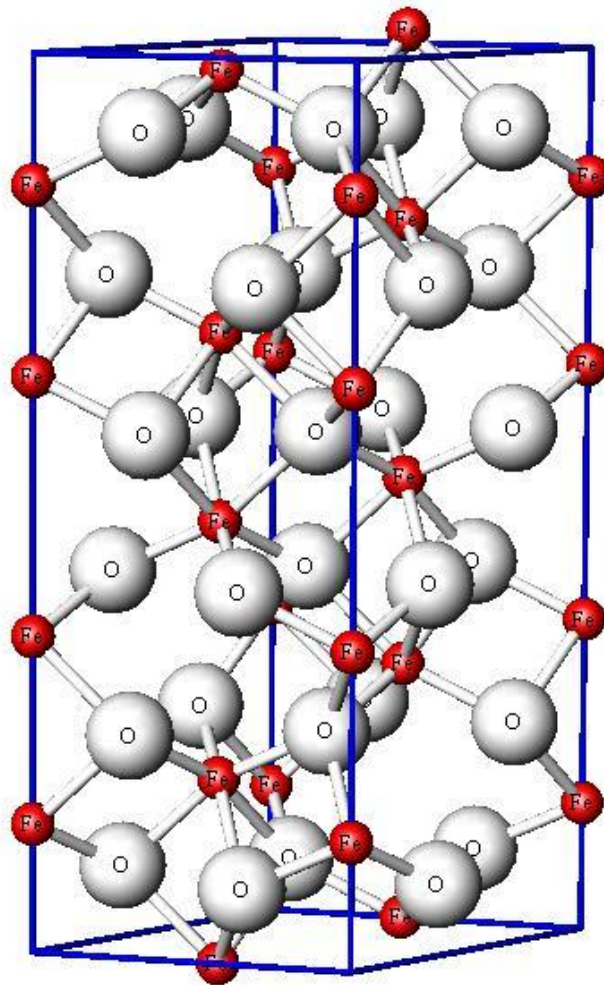
Figure 3.3: Crystal structure of Fe_2O_3 [78]

3.5 Ferrimagnetisms

In ferrimagnetic materials, the total magnetizations of the materials is non zero in the absence of a magnetic field and exhibits some spontaneous magnetization [63]. In ferromagnetic materials, the magnetic moments are antiparallel and unequal in magnitude to neighboring magnetic moments. Ferrimagnetic materials are similar to ferromagnets because they show spontaneous magnetization below the Curie temperature (T_c). Above the Curie temperature (T_c) these materials show magnetic disorder. Ferrites and magnetic garnets show ferrimagnetisms [76, 79-81].

3.5.1 Magnetic Hysteresis

In a ferromagnetic material, magnetization can be changed from zero to a maximum value or saturation value (M_s) when a magnetic field is applied to it. A graph for the magnetizing and demagnetizing process of the ferromagnetic materials which is called a hysteresis curve is as shown in Figure 3.4. In the region of 0 to 1, if the applied field is moderate, a reversible change in the magnetization of the material will occur when the applied magnetic field is removed, returning the magnetization to its initial state. Further increase in the applied field leads to saturation of magnetization M_S of the magnetic moments region 1 to 2 and all the magnetic moments are parallel to the direction of the applied magnetic field. After this point (2), the material is magnetically saturated and no further change in magnetization takes place. As the applied field decreases to zero, magnetization M of the material starts decreasing slowly and decreases to a finite value (point 3), called remanent magnetization (M_r) or remanence. The magnetization becomes zero if the applied magnetic field is opposite in direction (point 4) and the material becomes completely demagnetized. This magnetic field value where magnetization becomes zero is called the coercive field or coercivity (H_c).
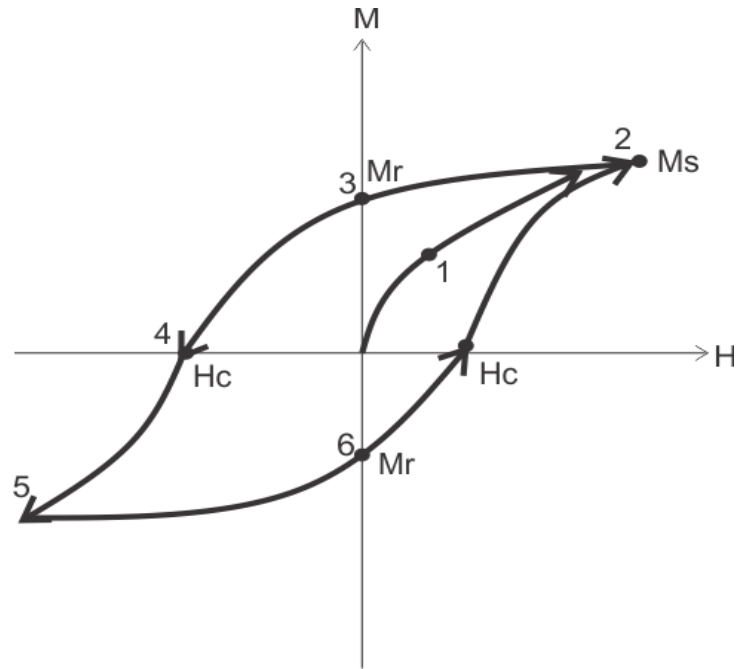
Figure 3.4: Hysteresis curve

If the applied field is gradually increased in the negative direction, magnetization again starts to realign with the applied magnetic field until it reaches the saturation value M_S (point 5) in the opposite direction. Once again, as the applied field decreases to zero, magnetization M of the material starts decreasing slowly and decreases along negative remanence axis. (Point 6). The magnetization becomes zero if the applied magnetic field is increased to the positive direction to coercive field (H_c). If the applied field is further increased in the positive direction, magnetization again starts to realign with the applied magnetic field and reaches saturation value M_S (point 2) in the positive direction.

3.5.2 Core Losses

Core losses or iron losses are produced in ferromagnetic materials due to time varying magnetic fluxes. The core losses can be classified as eddy current losses and hysteresis losses. These two losses produce heat dissipation in the magnetic circuit [82]. Therefore,

$$P_{core} = P_h + P_e \qquad\qquad (3.25)$$

3.5.2.1 Hysteresis Loss

When an external magnetic field is applied to a magnetic material, the material becomes magnetized and its domains oriented in the direction of the applied magnetic field. If the direction of the applied field is reversed in the opposite direction, the domains also will reverse their direction to orient themselves in opposite direction of the applied field. If applied field changes periodically the domains also will rotate periodically. Due to this process, power loss occurs which is called Hysteresis loss. Hysteresis loss produces heat dissipation and therefore increases the temperature of the magnetic material.

It is not easy to calculate the area of the Hysteresis curve because the B-H curve is nonlinear, multivalued and there is no simple mathematical equation for this curve. However, there are many empirical formulas for calculating the Hysteresis loss. For example, the formula described by Metz is commonly used [82].

$$P_h = v K_h B^n_m f \qquad\qquad (3.26)$$

Where v = volume of core,

K_h = constant whose value depends upon the ferromagnetic material,

B_m = maximum value of flux density,

f = frequency of variation of current,

The value of exponent is 1.5 to 2.5 which depends on the type of magnetic material.

3.5.2.2 Eddy Current Loss

An induced voltage is generated in a conducting material when changes occur in the magnetic flux that is link with the conducting material. For example, if a solid iron core

42

is used and a magnetic flux is varied through the iron core. If this iron core consists of concentric shells these shells can be consider as closed coil. Therefore due to closed circuit of each shell, the magnetic flux is linked with this closed circuit, thus producing induced voltage in each shell. Due to this induced voltage, a current starts flowing through the shell. As these currents do not flow through any definite path therefore these current are called eddy currents. These eddy currents cause heat dissipation in the iron core. The power loss is termed as eddy current loss [82]. The eddy current loss is given by,

$$P_e = \left(\frac{1.645}{\rho}\right) * t^2 f^2 B_m{}^2 \frac{w}{m^3} \qquad (3.27)$$

Where B_m = maximum value of flux density,

f = frequency,

t = thickness of core,

ρ = resistivity of the core material,

Power loss increases with increasing eddy current and additional rise in temperature is generated. Eddy current loss can be reduced if the core is made of a few thin sheets called laminations which are tightly insulated from each other. Therefore, the length of the closed path in which the eddy currents are flow is considerably reduced.

3.6 Study of the Modes of Stabilization in Nanofluid

There are two mechanisms namely electrostatic stabilization and steric stabilization to overcome the attractive forces between the particles which cause particle aggregation.

3.6.1 Electrostatic Stabilization

The key source to kinetic stability of particles is achieved due to the existence of electric charge on the surface of the particles. Electrostatic stabilization is achieved by the

adsorption of ions onto the surface of electrophilic metal particles. The adsorption takes place as an electrical double/multi-layer which create a Coulombic repulsion force between the nanoclusters [83]. This method is pH sensitive and of restricted use.

3.6.2 Steric Stabilization

Polymers or surfactant in the form of layers can be used to sterically stabilize the metal center by surrounding it due to sterically bulky property of the polymer/surfactantas shown in Figure 3.5 [84-86]. These adsorbed polymers or surfactant substances deliver a steric barrier which inhibits the metal particles from joining together [87].
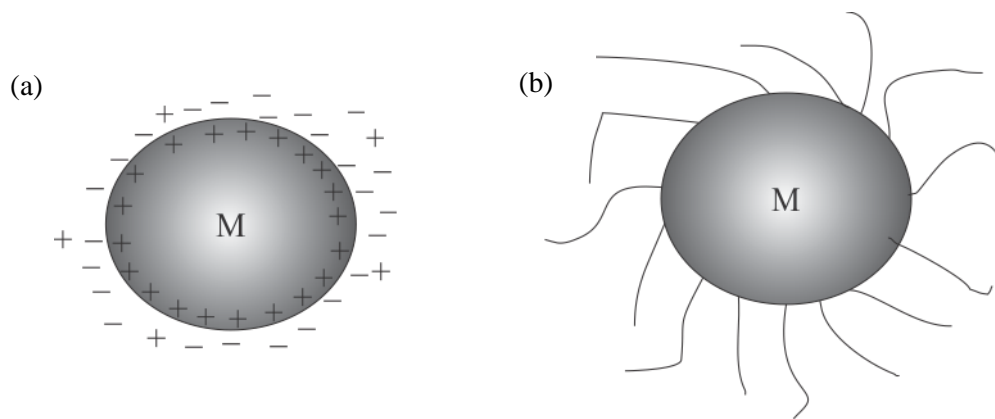
Figure 3.5: Schematic illustration for (a) electrostatically stabilized particle and
(b) a sterically stabilized particle

Colloidal stabilization can be achieved by a mechanism of haloing of nanoparticles. It contains the accumulation of charged nanoparticles to microspheres, which are likely to agglomerate due to their Van der Waals attractions. Therefore, colloidal stabilization is achieved by the accumulation of small nanoparticles, which brings an operative repulsion, countering the Van der Waals attractions between the particles.

3.7 Surfactants

Surfactants are compound with low or moderate molecular weight. Surfactant consist of two parts a hydrophobic part and a hydrophilic part. The hydrophobic part exhibit

high oil solubility but low water solubility. While the hydrophilic (or polar) shows high water solubility but low oil solubility [87], as shown in Figure 3.6.
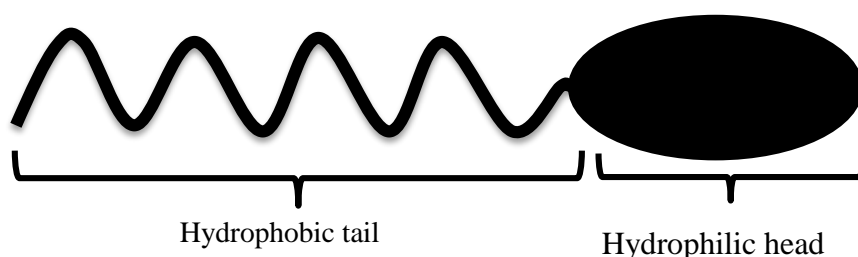
Figure 3.6: Schematic illustration of a surfactant molecule

The classification of surfactants is based on the hydrophilic headgroup. They are divided into two types ionic or nonionic. Surfactant shows the ability of self-joining to form micellar structures when the surfactant concentration in the solution exceeds a limiting value known as the critical micelle concentration (CMC) [88]. Surfactants are broadly used as additives to adjust the properties of polymeric systems for a diversity of applications [89-91].

3.7.1 Sodium Dodecyl Sulfate

Sodium dodecyl sulfate (SDS) ($NaC_{12}H_{25}SO_4$) is a common anionic surfactant,   as shown in Figure 3.7 , with a CMC of about 8.0 mM in pure water solution at 25°C [91, 92].

Figure 3.7: Chemical structure of SDS

3.8 Interfacial Tension (IFT)

Interfacial tension (IFT) is defined as excess of free energy or lateral stress at the interface of two phases. Interfacial tension is created due to excessive cohesive forces among the molecules of the same fluid and adhesive forces of unlike molecules at phase boundaries. Therefore, the surface area of new interface is minimized. Interfacial tension is denoted in milli–Newton/meter (mN/m as dynes/cm). IFT can be changed by adding of surface–active material known as surfactants at fixed temperature. In enhanced oil recovery, the properties of the three phases such as oil/aqueous/formation interfaces are very important. These properties are interfacial tension, contact angle, wettability, capillary forces, and viscous forces. These are characterized by a dimensionless group called the capillary number, N_c. The capillary number relates the mobilization of the blocked oil and enhanced oil recovery [93].

$$N_c = \frac{\mu v}{\sigma \cos \theta}$$

(3.28)

Where 'μ' is the dynamic viscosity of the liquid, 'ν' is the velocity, 'θ' is the contact angle and 'σ' is the interfacial tension between the oil and water phases. The capillary number, N_c, can be increased by increasing the viscosity or decreasing the interfacial tension in order to obtain better oil recovery in enhanced oil recovery process.

IFT can be reduced by adding certain additives and the reduction in IFT between crude oil and water increases the oil mobilization and lowers the capillary forces which results in increased oil recovery. Interfacial tension can significantly affect the other important rock properties such as wettability, capillary pressure, and relative permeabilities, which in turn affect the recovery of oil from petroleum reservoirs [94]. For more than a century, a range of techniques have been used to and a pendant drop measure interfacial tensions between fluid phases. The commonly used methods are pendant drop and spinning drop.

In a pendant drop method [95], two parameters of the pendant drop are be experimentally determined such as the diameter 'd' at the distance 'D' from the top of

the drop as shown in Figure 3.8. The following equation can be used to calculate the interfacial tension.

$$\gamma = \frac{\Delta\rho gD^2}{H}$$

(3.29)

Where γ = interfacial tension, D = equatorial diameter, $\Delta\rho$ = density difference, H = shape dependent parameter

The shape dependent parameter (H) depends on a value of the ''shape factor''

$$S = \frac{d}{D}$$
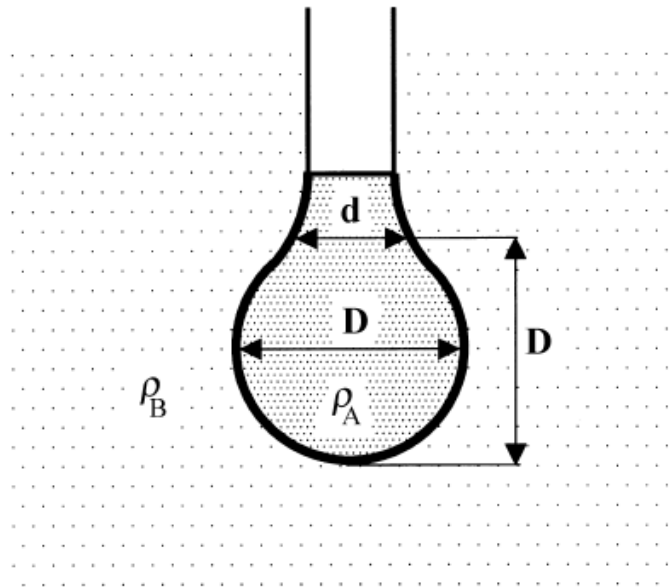
Figure 3.8: Pendant drop method [95]

For the measurements of ultralow interfacial tensions, the spinning drop technique has been established at both laboratory and commercial scales.

In this method, a drop of the oil (whose IFT is to be measured) and liquid are contained in a horizontal tube which spun about its longitudinal axis, considering the fact that gravitational force has a slight effect on the shape of a drop suspended in the liquid as shown in Figure 3.9.The fluid drop takes an ellipsoidal shape at low rotational velocities (ω), and it becomes cylindrical at sufficiently high rotational velocities. Under this condition, a relationship can be obtained between the interfacial tension, the radius (r) of the cylindrical drop, the density difference ($\Delta\rho$) between the drop and the

adjoining fluid, and the rotational velocity of the drop. The interfacial tension is measured from the following equation,

$$\gamma = \frac{1}{4} r^3 \Delta \rho \omega^2 \qquad (3.30)$$

Where γ = interfacial tension, ω = rotational velocities, $\Delta \rho$ = density difference, r = radius
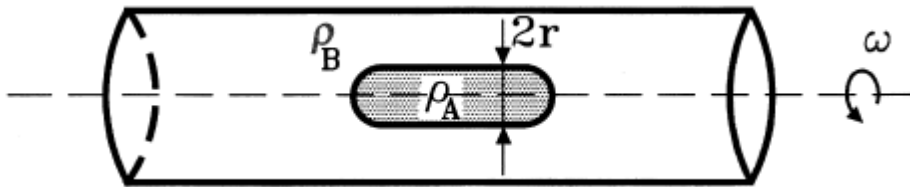
Figure 3.9: Schematic of the spinning drop method [95]

3.9 Magnetic Particle in a Magnetic Field

A magnetic particle in a fluid experiencing a magnetic field will be affected by several factors. These magnetic particles in a suspension when placed in a magnetic field experience a force and torque which depend on the magnitude of the magnetic field, and the magnetization of the particles due to slow movement of these particles [10]. The movement of particles in the fluid produces another force which is called drag force. Therefore, the particles experience another force due to the dragging of particles in the fluid. The effect of the magnetic force and the viscous drag force on the magnetic particles in the fluid is presented below. There are other factors which influence the particles in fluid such as particle-fluid interactions, buoyancy force, inter particle effects (magnetic dipole interactions), inertia, gravity, and thermal kinetics or Brownian motion.

The forces experienced by magnetic particles in a fluid in an external magnetic field are the magnetic and fluidic forces. The relationship of these forces is balanced according to Newton's second law:

48

$$m_p \frac{dv_p}{dt} = F_m + F_f \tag{3.31}$$

Where Fm = magnetic force, F_f = fluid force, m_p = mass of particle, v_p velocity of particle

The left hand side of the equation can be ignored because the mass of the particles is very small.

For simplicity, the magnetic particles can be replaced with an equivalent point like dipole moment which is placed at its center. The magnetic force and torque on a particle due the presence of the magnetic field are given by:

$$F_m = \mu_o V_p (M_p \cdot \nabla) H \tag{3.32}$$

$$F_m = (\mu \cdot \nabla) B \tag{3.33}$$

Here 'μ' is the magnetic moment of the particle and 'B' is the magnetic flux density.

$$T_m = \mu \times B \tag{3.34}$$

Due to the magnetic torque, the particle will align itself with the magnetic field.

According to the Brillouin function magnetization is given by:

$$M = N g \mu_B J \cdot B_j(x) \tag{3.35}$$

Here 'N' represents the number of atoms per unit volume, g is the g-factor or dimensionless magnetic moment, μ_B is the Bohr magneton, and x is the ratio of the Zeeman energy of the magnetic moment in the external field to the thermal energy. The value of x can be computed using the equation below,

$$x = \frac{g \mu_B J B}{k_B T} \tag{3.36}$$

49

Where k_B is the Boltzmann constant and 'T' is the temperature.

In the case of a large number of particles when averaged over or for time periods longer than the (Brownian and Néel) magnetic relaxation time, the function can be replaced in the Langevin function to relate µ to B.

$$m = \frac{M_{sat}B}{|B|}L(|B|) \quad L(|B|) = \coth(\varepsilon|B|) - \frac{1}{\varepsilon|B|}, \varepsilon = \frac{M_{sat}}{k_B T} \tag{3.37}$$

Where m_{sat} represents the saturation magnetization of the magnetic particle. If the magnetic particles are free to rotate in weak fields, the Langevin function can be linearized, therefore the magnetic force is given by

$$F_m \approx \frac{\varepsilon M_{sat}}{3}(B \cdot \nabla)B = \frac{\varepsilon M^2_{sat}}{3k_B T}(B \cdot \nabla)B \tag{3.38}$$

The drag force on the magnetic particles in fluid flow is dependent on their motion in the fluid. In a cylindrical vessel which has a radius *Rbv*, and having a laminar flow parallel to the axis with average velocity, the velocity profile is given by:

$$v_f(x) = 2\overline{v}_f(1 - (\frac{x}{Rbv})^2) \tag{3.39}$$

Stokes' law can be used to determine the fluidic drag force on a sphere in a laminar flow field with Reynolds number smaller than 1,

$$F_f = -6\pi\eta R_p(V_p - V_f) \tag{3.40}$$

Where 'η' is the viscosity of fluid and V_p and V_f are the velocity of the particle and the fluid, respectively, R_p is the radius of the particle [96].

3.10 Dielectric Particle in an Electric Field

The electromagnetic response of a dipolar particle in an electric field which causes polarization is explained by the models given below. These models discuss the

polarizations of the particles, forces/torques and motions of the particles of various shapes.

3.10.1 Polarization Model for Spherical Particles

3.10.1.1 Lossless dielectric spherical particle in lossless dielectric medium in a uniform field

A simple electrostatic polarization model can be considered if a dielectric spherical particle is suspended in an insulating liquid phase and the conductivities of both are neglected. Polarizations of the dielectric spherical particle in an external electric field takes place due to the bound charges. If we assume the particle is a perfect sphere, electric field induced dipole moments as given by the Laplace's equation gives the electric potential.

$$\nabla^2 \psi = 0 \tag{3.41}$$

In a constant applied electric field,

$$\vec{E}_o = E_o \vec{e}_z \tag{3.42}$$

Using these boundary conditions of the fluid and particle,

$$\psi_i = \psi_o \tag{3.43}$$

$$\varepsilon_p \nabla \psi_i \cdot \vec{n} = \varepsilon_f \nabla \psi_o \cdot \vec{n} \tag{3.44}$$

Where ε_p and ε_f are electric permittivities of particle and fluid respectively, and $\vec{n}$ represents the unit normal vector of the interface. The potential inside and outside the particles are represented by the superscript 'i' and 'o'.

The electrical potential in the solution form is

$$\psi_i = -E_o r \frac{3\varepsilon_f}{\varepsilon_p + 2\varepsilon_f} \cos\theta \qquad (3.45)$$

$$\psi_o = E_o r \left[1 - K \left(\frac{a}{r} \right)^3 \right] \cos\theta \qquad (3.46)$$

Where, $K = \dfrac{\varepsilon_p - \varepsilon_f}{\varepsilon_p + 2\varepsilon_f}$ is the Clausius-Mossotti function, 'a' is the radius of the particle, and 'r' is the distance from the center of the spherical particle to an arbitrary point in the electric field. The induced polarization due to the induced potential outside the particle is the same as that of a dipole oriented along the z-axis whose moment is given below [97-105].

$$p_{eff} = 4\pi\varepsilon_f K a^3 E_o \qquad (3.47)$$

Where, $K = \dfrac{\varepsilon_p - \varepsilon_f}{\varepsilon_p + 2\varepsilon_f}$ is the Clausius-Mossotti function, 'a' is the radius of the particle, and ε_f is fluid permittivity.

3.10.2 Dielectric Sphere with Ohmic Loss in Dielectric Medium with Ohmic Loss in an AC Field

In this case, we assume that the spherical particle and the fluid have finite electrical conductivities σ_p and σ_f respectively. If an electric field is applied to the suspension then free and bound charge is produced in the medium and in the particle. The value of the electric field in the case of the alternating electric field of magnitude 'E_o' and frequency 'f' is given by,

$$\vec{E}(t) = \mathrm{Re}\left[E_o \vec{e}_z \exp(j\omega t) \right] \qquad (3.48)$$

In this case Laplace's equation given in (3.41) and the boundary condition at the interface given in (3.43) are the same as in the lossless case.

Due to the time dependence and free charge accumulation on the interface, the continuity of the normal component of the displacement flux vector is replaced by the instantaneous charge conservation.

The effective moment is given as the Clausius-Mossotti function in a complex form

$$p_{eff} = 4\pi\varepsilon_f K a^3 E_o \tag{3.49}$$

Where $K = \dfrac{\varepsilon_p - \varepsilon_f}{\varepsilon_p + 2\varepsilon_f}$ \hspace{2cm} (3.50)

and the complex permittivities are

$$\vec{\varepsilon}_p = \varepsilon_p - \frac{\sigma_p}{\omega} j \tag{3.51}$$

$$\vec{\varepsilon}_f = \varepsilon_f - \frac{\sigma_f}{\omega} j \tag{3.52}$$

Using the characteristic relaxation time or Maxwell-Wagner time scale τ_{mw} the equation (3.50) can be rewritten as,

$$\vec{K}(\omega) = \left(\frac{\varepsilon_p - \varepsilon_f}{\varepsilon_p + 2\varepsilon_f} \right) \left[\frac{j\omega\tau_o + 1}{j\omega\tau_{mw} + 1} \right] \tag{3.53}$$

where

$$\tau_{mw} = \left(\frac{\varepsilon_p + 2\varepsilon_f}{\sigma_p + 2\sigma_f} \right) \tag{3.54}$$

and

$$\tau_o = \left(\frac{\varepsilon_p - \varepsilon_f}{\sigma_p - \sigma_f} \right) \tag{3.55}$$

The direction of the dielectrophoretic force at the low and high frequencies can be determined by using two limiting cases which depend on the relative magnitude of the characteristic relaxation time constant τ_{mw} and the frequency of the electric field.

$$\lim_{\omega\tau_{m\omega}\to 0} \vec{K} = \left(\frac{\sigma_p - \sigma_f}{\sigma_p + 2\sigma_f} \right) \tag{3.56}$$

and

$$\lim_{\omega\tau_{m\omega}\to 0} \vec{K} = \left(\frac{\varepsilon_p - \varepsilon_f}{\varepsilon_p + 2\varepsilon_f} \right) \tag{3.57}$$

In high frequency, limiting the difference of the electric permittivities affects the effective moments and at low frequency the difference of the electrical conductivities affects the effective moments.

3.10.3 Electrostatic Forces and Torques Applied on a Particle with Ohmic Loss in a Dielectric Medium in an AC Field

As in external electric field, the polarization of the particles takes place due to the force and torque in the presence of the electric field which tries to move and rotate the particles.

3.10.3.1 Force and torque applied by the external electric field

In the time dependent electric field, the instantaneous force and torque applied on a dipole are given by

$$\vec{F}_{dep}(t) = \vec{p}_{eff} \cdot \nabla\vec{E}(t) \tag{3.58}$$

$$\vec{T}^e(t) = \vec{p}_{eff} \times \vec{E}(t) \tag{3.59}$$

$\vec{F}_{dep}$ is called the dielectrophoretic (DEP) force. This dielectrophoretic (DEP) force is experienced by the polarizable particle in the presence of the electric field. The magnitude of the dielectrophoretic (DEP) force is influenced by the particle electric properties, surrounding medium, the particle's size, and the frequency of the electric field. The torque applied by the electric field is represented by $\vec{T}^e$ which pushes the particle to rotate and align in the direction of the electric field.

The general form of the DEP force and the torque applied by the electric field according to the effective moment method is given by [106]

$$\vec{F}_{dep}(t) = \text{Re}\left[\vec{p}_{eff}\exp(j\omega t)\right] \cdot \nabla \text{Re}\left[\vec{E}\exp(j\omega t)\right] \tag{3.60}$$

and

$$\vec{T}^e(t) = \text{Re}\left[\vec{p}_{eff}\exp(j\omega t)\right] \times \text{Re}\left[\vec{E}\exp(j\omega t)\right] \tag{3.61}$$

3.11 Electromagnetic Waves

The transmission of electromagnetic energy is described by Maxwell's equations which show that electromagnetic energy travels in the form of electromagnetic waves from the time-varying sources of current and charges. The electromagnetic waves are solutions of the Maxwell's equations [107-112].

All EM waves are time-dependent electromagnetic fields and obey the Maxwell's equations. If the EM waves are time-harmonic fields with sinusoidal time-variation, they have the form as:

$$\bar{E}(t) = \bar{E}_o\cos(\omega t + \varphi_E) \tag{3.62}$$

$$\bar{H}(t) = \bar{H}_o\sin(\omega t + \varphi_H) \tag{3.63}$$

Where ω is the angular frequency (rad), φ_E is the initial phase of E and φ_H is the initial phase of H. If vacuum is considered as the medium, the equations can be transformed to the Helmholtz equations, which are also the general solution for EM waves propagating in 3D space.

$$\nabla^2 \bar{E} + \omega^2 \mu\varepsilon\bar{E} = 0$$
(3.64)

$$\nabla^2 \bar{H} + \omega^2 \mu\varepsilon\bar{H} = 0$$
(3.65)

ε and μ are complex tensors in the Helmholtz equations. These two equations are uncoupled. Only one of the two equations needs to be solved in order to completely describe the whole problem.

3.11.1 Power flow of EM waves

The time-dependent power flow density of the EM wave is given by the instantaneous Poynting vector:

$$\bar{P}(t) = \bar{E}(t) \times \bar{H}(t)$$
(3.66)

The time-average power flow density for time-varying fields is given by:

$$\left\langle \bar{P}(t) \right\rangle = \frac{1}{T}\int_0^T \bar{P}(t)dt = \frac{1}{T}\int_0^T \bar{E}(t) \times \bar{H}(t)dt$$
(3.67)

Where T is the period of the EM wave.

If the EM waves are time-harmonic fields and E and H are represented in phasor forms, the complex Poynting vector is defined as:

$$\bar{P} = \bar{E} \times \bar{H}^*$$
(3.68)

where H* is the complex conjugate vector of H.

It can be shown that:

56

$$\left\langle \bar{P}(t) \right\rangle = \mathrm{Re}\left\{ \bar{P} \right\}$$

<div align="right">(3.69)</div>

In a lossy medium, the field E and H are attenuated as the factor of $e^{-j\alpha z}$, the power density is attenuated as the factor of $e^{-j2\alpha z}$.

CHAPTER 4

METHODOLOGY

The methodology adopted for this research work is briefly described. The design of the water flooding system for the electromagnetic enhanced oil recovery by using nanofluids is presented. The CASTEP simulations for zinc oxide and iron oxide is discussed in this chapter. In this chapter the synthesis of nanoparticles by sol gel method as well as the preparation of the nanofluids are discussed. The application of nanofluids for oil recovery in water flooding system is also explained.

4.1 Scope of Work

The scope of this research work includes a simulation study of zinc oxide and iron oxide using Accelrys software, CASTEP for determining the band structure which describes the range of energy of an electron within a solid structure and the density of state which describes the number of quantum state per unit energy. The scope of work also covers the synthesis and characterizations of two different types of metal oxides nanoparticles i.e. ZnO and Fe_2O_3 for EOR application. The dipole antenna was then used to provide the electromagnetic waves to the glass bead packed sample saturated with oil and nanofluids.

The nanoparticles were synthesized by using sol-gel method. The structural properties of ZnO and Fe_2O_3 were analyzed using XRD, FESEM, EDX and TEM. Both nanoparticles were then dispersed into the base fluid to form a colloidal suspension of nanofluids of different concentrations. After that the designing of the experimental setup for the measurement of oil recovery with and without electromagnetic wave was carried out. The porous medium consisting of glass bead packed sample was prepared and characterized for its petro physical properties e.g. porosity, permeability and pore volume. The feasibility of this proposed technique was tested using a glass bead packed column of porous medium

connected with inlet and outlet tubings which were fed to the pump and oil collector. The porous medium was immerses in a water tank. The experiments were performed at 60°C and ambient pressure, electromagnetic waves from generated from the antenna during the water flooding experiment.

4.2 Methodology Flow Chart

This part focuses on the overall research workflow of using nanofluids combined with electromagnetic waves for oil recovery application. A new electromagnetic water flooding system was designed to study the oil recovery using nanofluids. The nanofluids were prepared using by nanoparticles of iron oxide and zinc oxide which were then used in the new water flooding system. A flow chart of the methodology is shown in Figure 4.1.
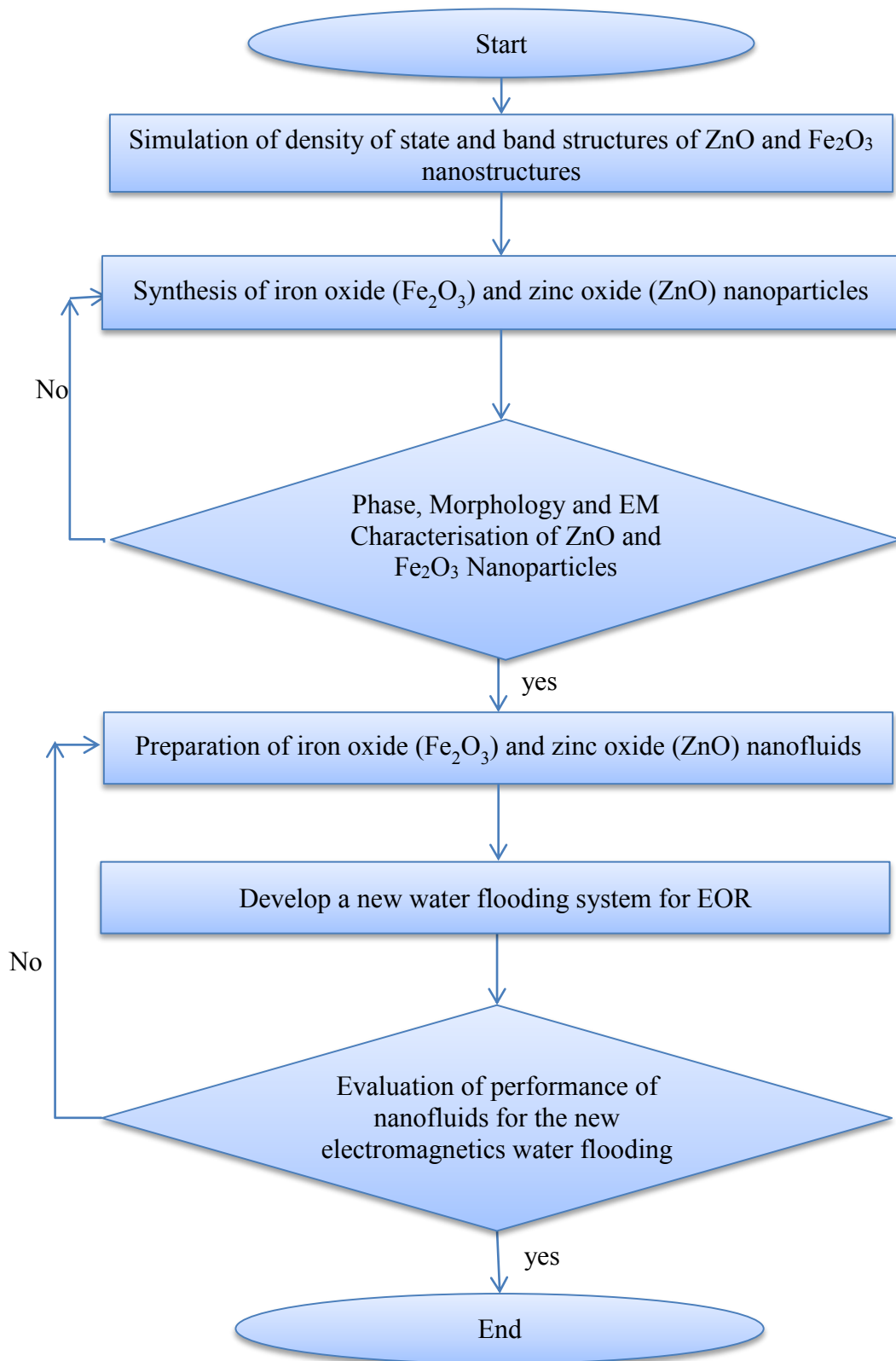
Figure 4.1: Flow chart of the methodology

4.3 Computational Method

The geometry optimizations were performed using Cambridge Serial Total Energy Package (CASTEP) provided by the Material Studios 6.1 by Accelrys. CASTEP is a first-principle pseudo-potential method based on Density-Functional Theory (DFT). In CASTEP, pseudo-potential is replaced with the ionic potential and the wave function is described by a plane wave. A generalized gradient approximation (GGA) is used to improve the exchange and correlative potential of electronic-electronic interactions [113-117] .

The DFT calculations were performed using plane wave (PW) basis sets and ultrasoft pseudopotentials [118]. In the simulation, the exchange correlation functional used was the generalized gradient approximation (GGA) which was developed by Perdew, Burke and Ernzerhof (PBE) [113, 114, 119]. The ultrasoft pseudo-potentials represent the interactions between valence electrons and the ionic core. The valence electron configurations used in the study included 3d104s2 for Zn, 3p6d64s2 for Fe, and O 2s2p4 for O.

For ZnO and Fe_2O_3 the kinetic energy cut-off is 340 eV for the plane wave basis. The Brillouin zone was sampled using Monkhorst and Pack special k-points of a $9 \times 9 \times 6$ grid ZnO and $5 \times 5 \times 5$ grid for Fe_2O_3 for surface calculation [120]. The convergence criteria for ZnO for structure optimization and energy calculation met the conditions of (a) an energy tolerance of 0.1000×10^{-4} eV/atom; (b) maximum force tolerance of 0.3000×10^{-1} eV/Å; and (c) maximum displacement tolerance of 0.1000×10^{-2} Å. The convergence criteria for Fe_2O_3 for structure optimization and energy calculation met the conditions of (a) an energy tolerance of 0.2000×10^{-4} eV/atom; (b) maximum force tolerance of 0.5000×10^{-1} eV/Å; and (c) maximum displacement tolerance of 0.2000×10^{-2} Å.

4.4 Synthesis of Nanoparticles

This section will discuss the preparation for zinc oxide (ZnO) and iron oxide (Fe_2O_3) nanoparticles using sol-gel method.

4.4.1 Preparation of Iron Oxide (Fe₂O₃) / Zinc Oxide (ZnO) Nanoparticles by Sol Gel Method

Iron oxide (Fe_2O_3) and zinc oxide (ZnO) nanoparticles were prepared by sol-gel method using iron nitrate nonahydrate and zinc nitrate hexahydrate ($Fe(NO_3)_3$ $9H_2O$)/($Zn(NO_3)_2$ $6H_2O$),and nitric acid (HNO_3). The iron nitrate nonahydrate ($Fe(NO_3)_3$ $9H_2O$) / zinc nitrate hexahydrate (Zn $(NO_3)_2$ $6H_2O$) was dissolved separately in aqueous solution of 80 ml nitric acid HNO_3.

4.4.2 Zinc Oxide (ZnO) nanoparticles

Using the sol gel method, ZnO nanoparticles were prepared by dissolving zinc nitrate hexahydrate ($Zn(NO_3)_2 6H_2O$) in an aqueous solution of 80 ml nitric acid HNO_3. The solution was stirred at 250 r.p.m for 7 days. After the 7 day period, the solution was heated using a hot plate stirrer; gradual heating was applied to reach the desired temperature of 80ºC. After 30 min, temperature reached 80ºC and gel was formed. The gel was dried in the oven at 120ºC for 2 days, after which the dried powder was ground for 4 hours. Following that, the powder was sintered at 200ºC and 300ºC for 2 hours to get ZnO nanoparticles.
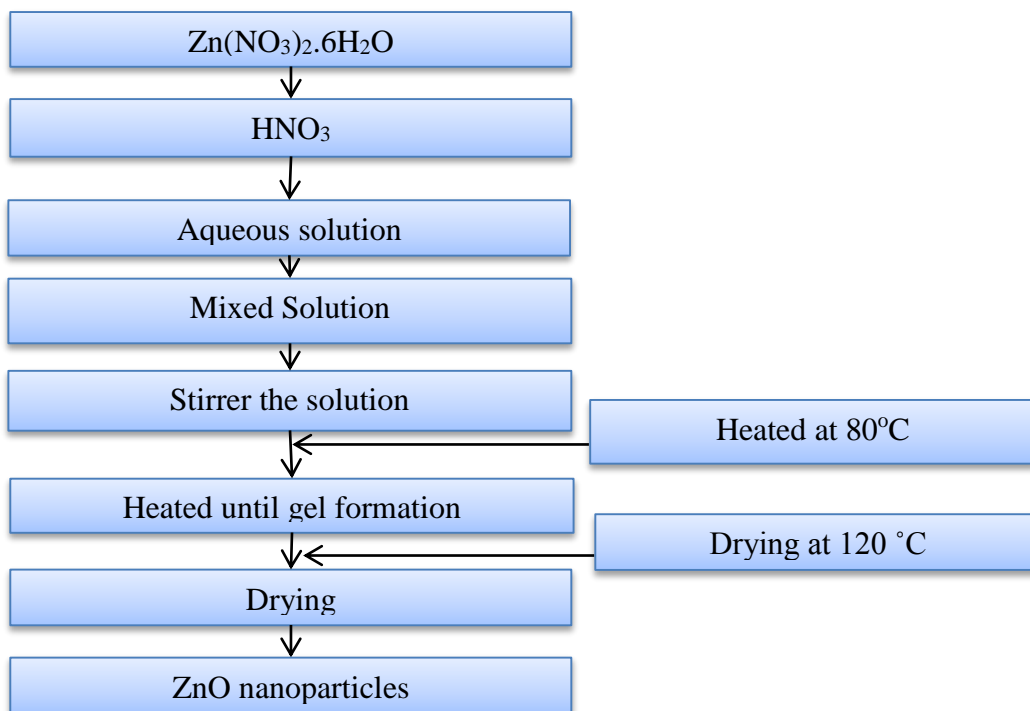
Figure 4.2: Flow chart for preparation of ZnO nanoparticles by sol gel method

4.4.3 Iron Oxide (Fe₂O₃) nanoparticles

Fe_2O_3 nanoparticles were prepared by sol-gel method using iron nitrate nonahydrate $(Fe(NO_3)_2 .9H_2O)$ and nitric acid (HNO_3). Iron nitrate nonahydrate $(Fe(NO_3)_2 .9H_2O)$ was dissolved in the aqueous solution of 80 ml nitric acid HNO_3. The solution was stirred at 250 rpm for 7 days. The solution was subjected to gradual heating using the hot plate stirrer until the temperature reached 80°C and gel was formed. The gel was then dried in the oven at 120°C for 2 days and the dried powder was ground for 4 hours. After that, the powder was sintered at 200°C and 300°C for 2 hours to get Fe_2O_3 nanoparticles.
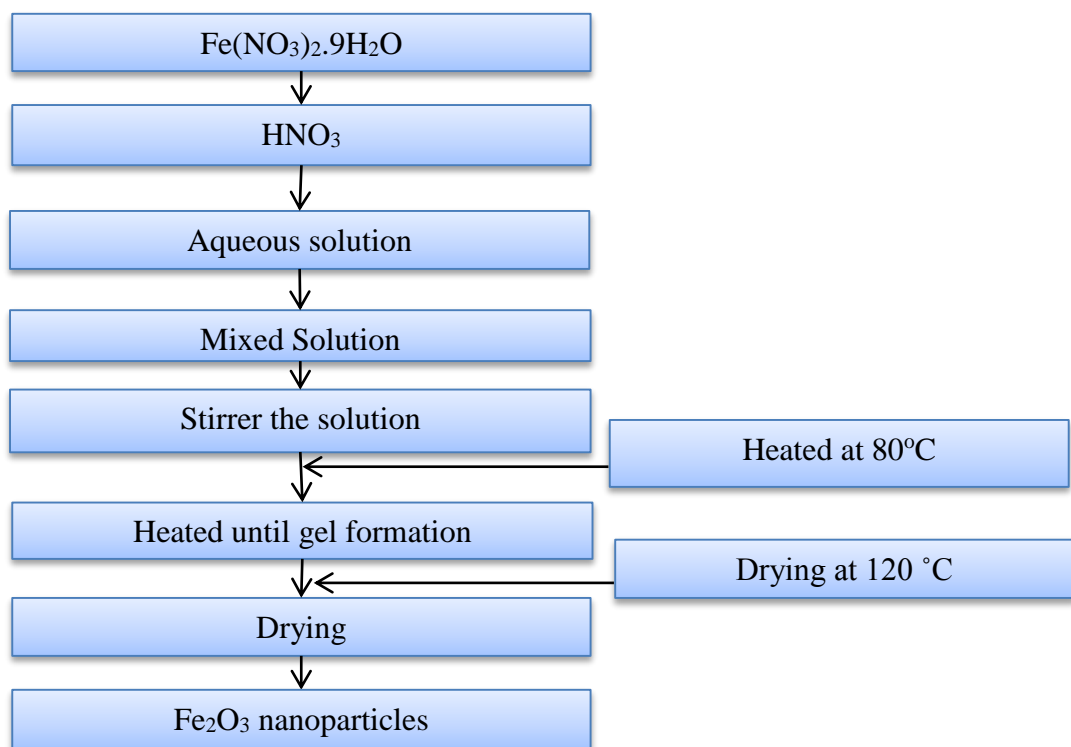
Figure 4.3: Flow chart for preparation of Fe₂O₃ nanoparticles by sol gel method

4.5 Nanofluid Preparation

The nanofluids were prepared by directly mixing the stabilizer with the nanoparticles. Firstly, the nanoparticles were synthesized in the form of powders, and secondly, these powders were introduced into the stabilizing fluid. The best samples of single phase

ZnO, and Fe_2O_3 nanoparticles were selected for our study. ZnO and Fe_2O_3 nanoparticles were prepared at three different concentrations of 0.001 %, 0.05 % and 0.1 %, with sodium dodecyl sulphate (SDS) stabilizer of concentration 0.05%. In order to get further dispersion of ZnO, and Fe_2O_3 in sodium dodecyl sulphate (SDS), they were sonicated for 2 hours.

4.6 Core Flooding Experimental Setup

The oil recovery due to the zinc oxide (ZnO), and iron oxide (Fe_2O_3) nanofluids were investigated by utilizing an acrylic column packed with glass beads. The experimental setup was comprised of an acrylic column, injection pump, antenna with magnetic feeders and a water tank; the setup is shown as in Figure 4.4. The water tank was filled with salt water of 30000 ppm salinity and has a density of 1.006g/cc to simulate reservoir environment. There are three sections in the experimental setup namely injection section, displacement section and collection section. The injection section consists of injection pump, valve, and pressure gauge and injection fluids such as brine, oil and nanofluids. In the injection section, all the components are connected with suitable connectors and nylon tubing. The displacement section consists of a porous medium made of glass beads packed in acrylic column, and the collection section consists of measuring cylinder, pressure gauge on the outlet and a control valve. A temperature controller is used to keep the temperature of the water at 60°C.

Electromagnetic waves were produced by connecting a function generator to supply electromagnetic waves to the antenna at a frequency 30MHz and 10V_{pp} voltage. The experiments were conducted with the injection of zinc oxide (ZnO), and iron oxide (Fe_2O_3) nanofluids into the packed acrylic column which was exposed to EM waves.
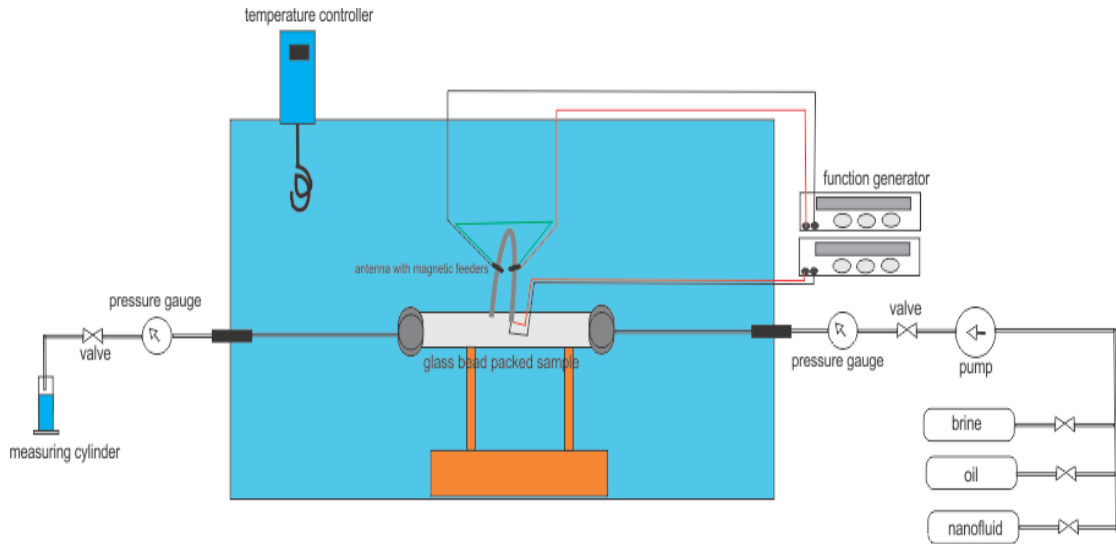
Figure 4.4: Schematic diagram of the experimental setup for ZnO and Fe_2O_3 nanofluids enhanced oil recovery

4.7 Reservoir Rocks Characterization

The acrylic column packed with glass beads was saturated with brine of salinity 30000 ppm until a constant pressure was achieved. Brine was prepared by dissolving NaCl in deionized water. The flow rate (q), brine density (μ), length (L) and area (A) of the PVC column were fixed using the following values,

$$q= 1ml/min,$$

$$μ= 1.02cp,$$

$$L= 9cm,$$

$$A = 7.0686 \text{ cm}^2.$$

Brine filled the pore/empty space between the glass beads in the PVC column. By using Darcy formula in equation 4.1, the permeability of the PVC column was calculated.

$$\text{Permeability, } k = \frac{q\mu L}{A\Delta P} \tag{4.1}$$

At a constant pressure (P), the permeability of the acrylic column packed with glass beads was calculated. When the pressure was constant, crude oil with the properties as shown in Table 4.1 was injected into the column. The crude oil replaced the brine in the column and the displaced brine was collected in a measuring cylinder. The volume of the displaced brine represents the volume of crude oil occupying the pores between the glass beads in the column. This volume of oil represents the amount of original oil in place (OOIP). Water flooding was carried out by injecting brine for the second time into the column until it was confirmed that no more oil dropped from the outlet tube.

Due to water flooding, some amount of oil was displaced from the column which represents the volume of oil recovered after water flooding. The amount of oil that remained in the column represents the residual oil in place (ROIP).

The nanofluid was injected into the column following the water flooding. During the injection of nanofluid, the column was exposed to electromagnetic waves emitted from the antenna. Such a condition is a simulation of enhanced oil recovery process by water flooding using nanoparticles combined with electromagnetic wave. During the nanofluid injection, the oil recovered was collected and the experiment was ceased when it was confirmed that no more oil dropped from the outlet tube.

Table 4.1: Details of the crude oil used in the water flooding experiment

Type of crude oil	Arabian heavy
Origin	Saudi Arabia
Density @ 25°C	0.889
API Gravity	28.1
Viscosity (mm2/s @ cSt)	20.25

4.7.1 Porosity

It is the ratio of empty space in the rock to the matrix. This is an important petrophysical property which determines the amount of oil in the reservoir. More oil is likely to be present in more porous reservoir compared to less porous reservoir. Therefore, in reservoirs with high porosity, higher residual oil after the primary and secondary recoveries can be expected. The formula to calculate porosity is given in equation 4.2 below,

$$\text{Porosity} = \frac{\text{pore volume}}{\text{bulk volume}}$$

$$\varphi = \frac{V_p}{V_b} \tag{4.2}$$

Where φ = reservoir porosity, V_b = bulk volume , V_p = pore volume

4.7.2 Permeability

Permeability indicates the flow of fluids through the reservoir rocks due to a given pressure gradient. It is measured in Darcies (D) or millidarcies (mD). It depends on the size, shape and the interconnection between the pore spaces. Permeability can be calculated from Darcy's law (equation 4.3).

$$\text{Permeability, } k = \frac{q\mu L}{A\Delta P} \tag{4.3}$$

Where q = flow rate, μ = density, L = Length, and A = area, ΔP = pressure gradient

4.8 Core Flooding Test

In the core flood experiments, four main stages were carried out to determine the effect of using nanofluid for oil recovery as shown in Figure 4.5. There are two approaches used in the experiments in order to classify the role of nanofluids in improving oil recovery, which are:

67

1. Injection of ZnO nanofluid and Fe_2O_3 nanofluid without electromagnetic waves to detect the role of nanoparticles alone in recovering more oil.

2. Injection of ZnO nanofluid and Fe_2O_3 nanofluid with electromagnetic waves to examine the role of electromagnetic waves in stimulating nanoparticles.

These experiments were done at the temperature of 60°C and ambient pressure, by using the setup as shown in Figure 4.4. To simulate the reservoir condition the glass bead packed column was firstly saturated with brine by injecting brine of concentration 30,000 ppm at a rate of 1 ml/min into the column. When the differential pressure between the inlet and outlet had stabilized, the permeability of the column was calculated using equation 4.3. Then Arabian heavy crude oil was injected into the brine saturated column to flush out brine until some droplets of oil appeared from the outlet and were collected. The initial amount of oil held in the porous medium (acrylic column packed with glass beads) was also determined by water flooding process carried out by injecting brine at the same flow rate as before to duplicate the secondary recovery stage. During water flooding process, about 40% of the initial (original) oil in place will be displaced before reaching residual oil saturation.

During the experimental enhanced oil recovery (EOR) in the laboratory, up to 4 pore volumes of nanofluids were injected at a rate of 1 ml/min in the presence of electromagnetic waves; 30 MHz square wave at 10vpp was imparted to the glass bead packed column during both nanofluid injections. The recovery efficiency for each stage, ER was calculated by equation 4.4 using the volume of oil recovered after the nanofluid injection for both with and without electromagnetic waves application as a percentage of the oil present after water flooding (ROIP).

$$E_R (\% ROIP) = \left(\frac{\text{volume of oil recovered in EOR fluid injection}}{\text{volume of remaining oil in place (ROIP)}} \right) \times 100 \qquad (4.4)$$
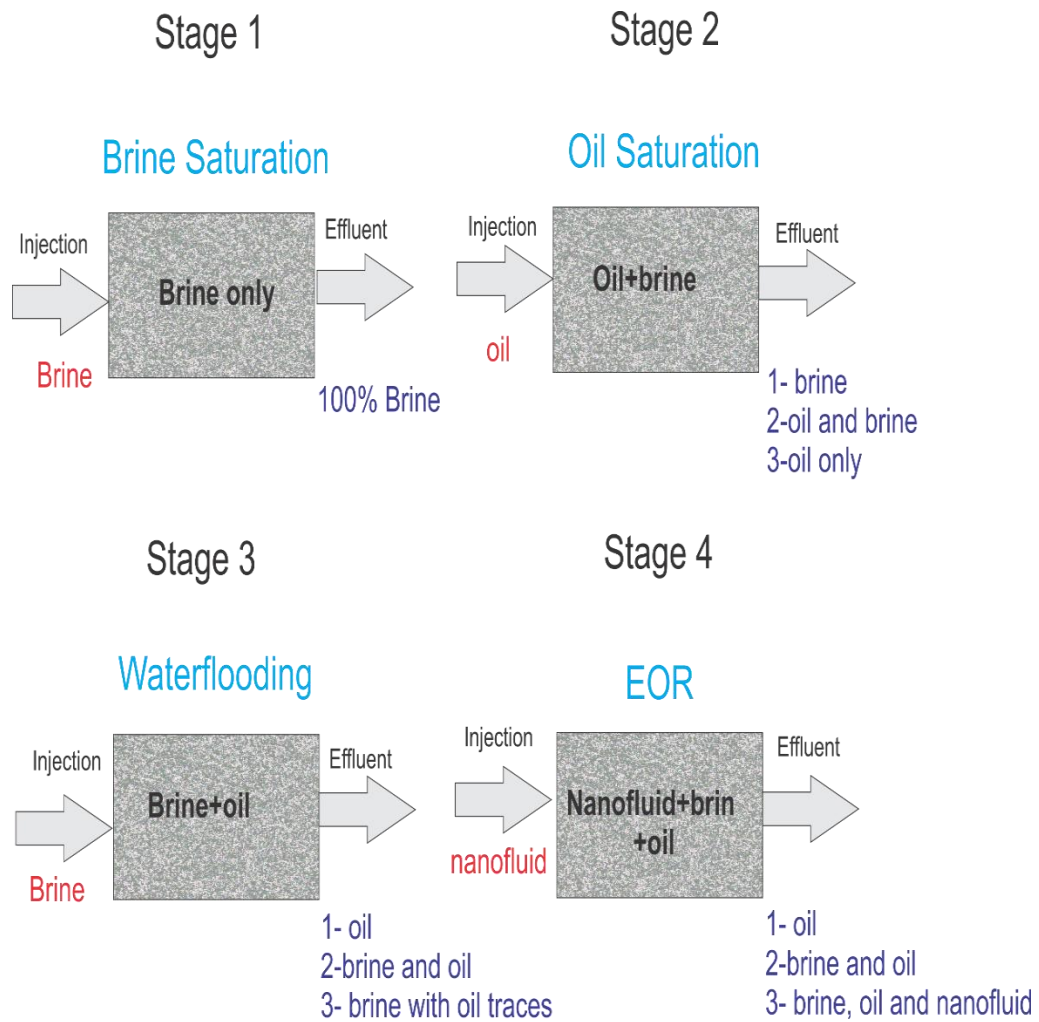
Figure 4.5: Four stages of core flooding test

4.9 Characterization of the Nanoparticles

The synthesized nanoparticles are characterized by using equipment such as X-ray powder diffraction (XRD) which is used to observe the crystallization of the nanoparticles, Field Emission Scanning Electron Microscope (FESEM), Energy Dispersive X-ray (EDX) for the morphology analysis of powders sample and its composition. Transmission electron microscope is used to observe the morphology and electron diffraction patterns of materials.

4.9.1 X-Ray Diffraction (XRD)

X-ray diffraction is a method that discloses detailed information about the crystallography and composition of materials. The principle of X-ray diffraction is based on the interference of the monochromatic X-ray waves from the crystalline sample. When incident rays interact with the crystallographic planes of the crystalline sample, the incident rays are diffracted from the sample and interfere constructively when the Bragg's law conditions are satisfied (Figure 4.6). Bragg's law relates the wavelength of X-rays to the lattice spacing between the crystallographic planes and the diffraction angle [121-124]. Bragg's law is defined as,

$$2dsin\theta = m\lambda \qquad\qquad (4.5)$$
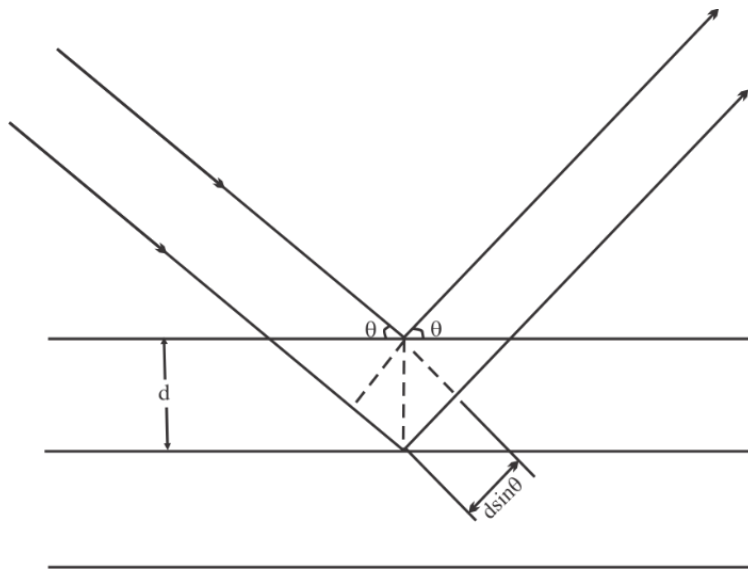
Figure 4.6: Schematic description of Bragg's diffraction law

These diffracted rays are detected by a detector by scanning the sample through 2θ angles range. In the case of powder samples, all possible diffraction directions of the crystallographic planes must be obtained due to random orientation. The diffracted peaks obtained from the diffraction pattern can be used to obtain d-spacing between the crystallographic planes. These d-spacings are used for the identification of the materials by comparison with a standard d-spacing pattern because every material has a unique d-spacing.

For structural properties, X-ray diffraction (XRD) measurements were performed on a Bruker D8 advance X-ray diffractometer by Cu-kα radiation (λ = 1.5406 Å) with an accelerating voltage of 40 kV. From the XRD patterns, the crystallite size of the nanoparticles is calculated according to Scherrer equation (equation 4.6),

$$D = \frac{0.9\lambda}{\omega\cos\theta} \qquad (4.6)$$

Whereas,

θ = Bragg's angle, ω = full width at half maximum (FWHM), λ = wavelength of incident radiation, 0.9 = shape factor for the metal oxide.

4.9.2 Field Emission Scanning Electron Microscopy (FESEM)

The shape, morphology and grain size of the nanoparticles were determined using field emission scanning electron microscopy (FESEM) as shown in Figure 4.7 (b).The scanning electron microscope is used to produce the magnified images by using an electron beam as compared to conventional light microscopes which use light waves. Therefore, SEM discloses 3D images of the samples as compared to light microscope.

With the application of a powerful electric field close to the filament tip, electrons are emitted (Figure 4.7(a)). The size and closeness of the electric field to the filament causes the electrons to flow out. In a field emission scanning electron microscopy (FESEM), field emission cathode in the electron gun of a scanning electron microscope compromises finer probing beams both at low and high electron energy. Due to which, a better-quality spatial resolution is possible as well as reduced sample charging and destruction which is significant for the characterization of organic specimens like polymers. Coating free sample characterization can be done at low voltage which gives high resolution. The working principle of SEM is shown in Figure 4.7(a) [125].

Some of the applications of FESEM are to analyze the cross section of semiconductor devices, determine structure uniformity and coating thickness, measure

small contamination feature geometry, and elemental composition of materials. There are several advantages of FESEM. One of which is it is able to produce clear electrostatically distorted images with spatial resolution down to 1.5 nm. At electron accelerating voltages smaller-area contamination spots can be scanned similar with energy dispersive X-ray spectroscopy. The penetration of low energy electrons can be reduced near to the material surface. Even at low voltage, high quality images are attainable with negligible electrical charging of samples [126-130].
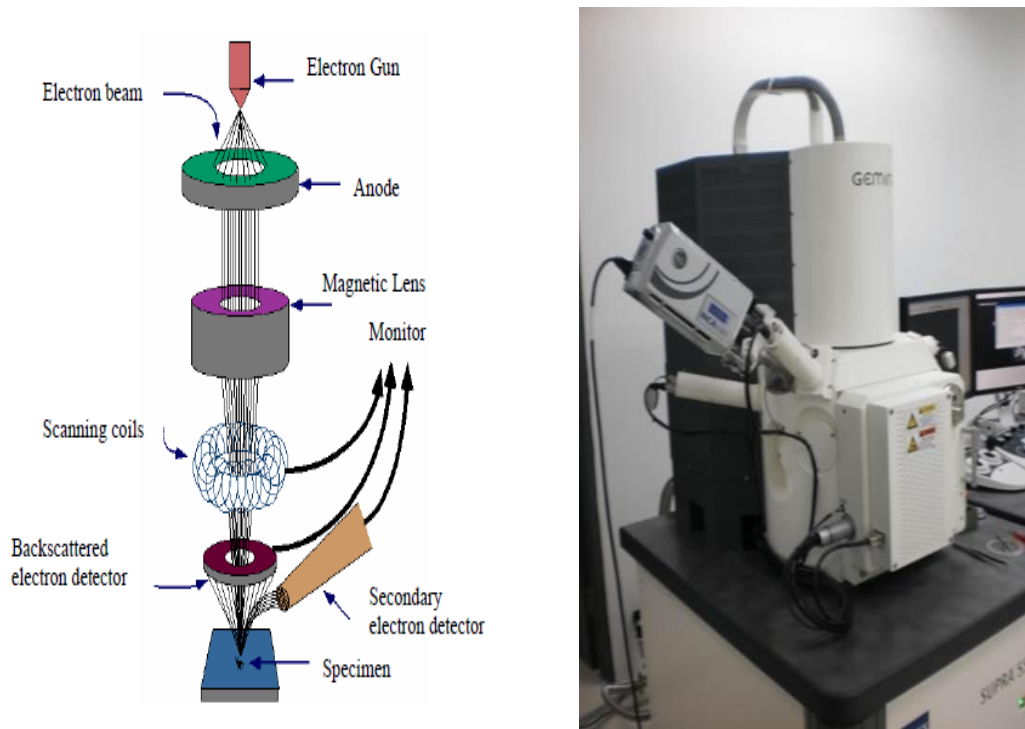
Figure 4.7: (a) A schematic diagram of scanning electron microscopy [125]
(b) ZEISS Supra 55VP field emission scanning electron microscope

4.9.3 High Resolution Transmission Electron Microscopy (HRTEM)

High resolution transmission electron microscopy HRTEM (model Zeiss Libra 200FE) was used to characterize the morphology and structure of the products.

4.9.3.1 Working Principle of the Transmission Electron Microscope (TEM)

In transmission electron microscopy (TEM) technique, beams of electrons interact and pass through a specimen. The magnetic lenses are used to focus and magnify the beams of electrons when emitted from the source. The schematic diagram of the transmission electron microscope (TEM) is shown in Figure 4.8. Two condenser lenses are used to confine the electron beam which also controls the brightness of the beams. These electron beams pass through the condenser aperture and strike the sample surface. The electron beam, which is elastically scattered, is transmitted from the sample and passed through the objective lens. The image of the sample is formed by the objective lens. The elastically scattered electrons are chosen by the objective lens and the selected area aperture that will form the image of the sample. After that, the electron beam passes through the magnifying system which consists of three lenses, two intermediate lenses which controls the magnification of the image and the projector lens. The final image of the sample is shown either on a fluorescent screen or on a monitor [131-134].
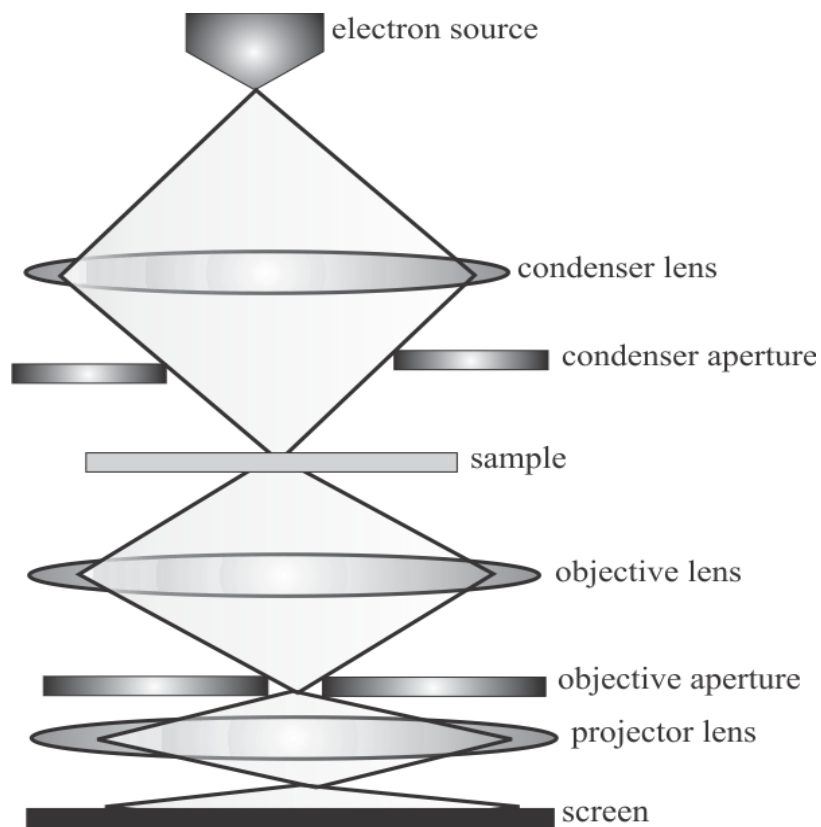
Figure 4.8: A schematic diagram of transmission electron microscope (TEM)

4.10 Vibrating Sample Magnetometer (VSM)

The magnetization of any magnetic sample can be measured with a vibrating sample magnetometer. The working principle of a vibrating sample magnetometer is based on Faraday's law of induction. The sample is magnetized with the help of a large magnet in vibrating sample magnetometer. The magnetized sample is placed in a pickup coil and it is vibrated vertically. Due to this vibration of magnetized sample, an induced emf is produced in the coil. The induced emf represents the value of magnetization in the sample. Due to this emf, an induced current is produced in the coil. The magnetization of sample is proportional to the induced current in the coil. Higher value of current represents a higher value of magnetization in the sample. An amplifier is used to amplify the induced current. All the components are interfaced to a computer for plotting graph. A schematic diagram of a vibrating sample magnetometer is shown in Figure 4.9.
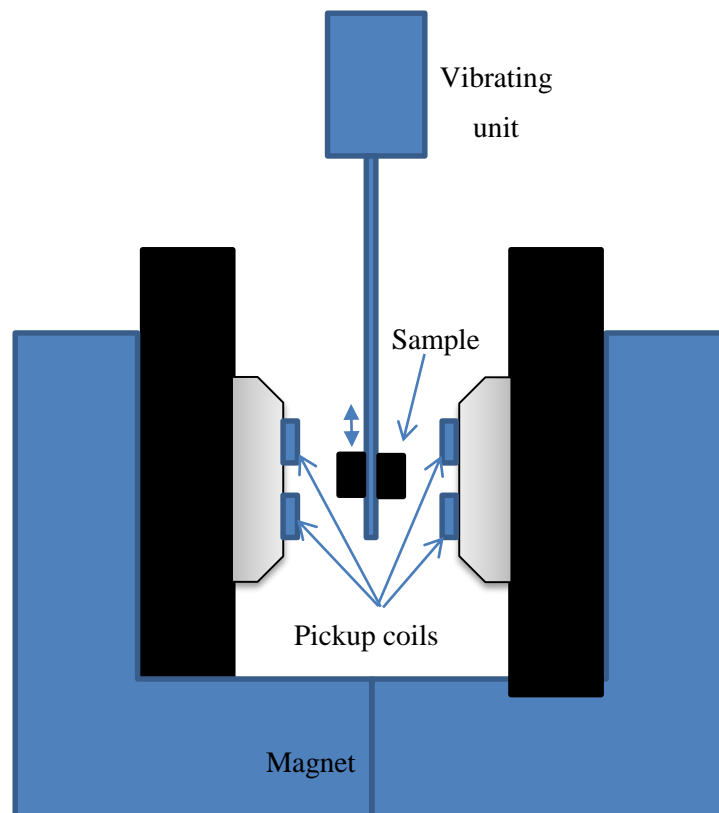
Figure 4.9: Schematic of a vibrating sample magnetometer

CHAPTER 5

RESULTS AND DISCUSSION

This chapter describes the CASTEP simulation of zinc oxide and iron oxide band structure and density of state. The nanoparticles characterization for the application of enhanced oil recovery in water flooding system is also discussed. This chapter is divided into different sections. The first section gives the simulation of the band structure and density of state of iron oxide and zinc oxide. The results and discussion on the characterizations of the nanoparticles and nanofluids are provided in the second section of the chapter. At the end of this chapter, the application of iron oxide and zinc oxide nanofluids for oil recovery with and without electromagnetic waves in water flooding system is presented.

5.1 Band Structure and Density of State of ZnO and Fe_2O_3

The electronic band structures of ZnO and Fe_2O_3 were calculated using density-functional theory (DFT). The electron densities represent the potential with the minimum energy to obtain the Kohn-Sham equation. These electron densities can be solved using a local density approximation (LDA) as well as the generalized gradient approximation (GGA). The linear GGA is approximate because the actual atomic bonds include the exchange and correlation integrals; these integrals may be compared with the LDA. The analysis of density of states (DOS) could give an insight into the surface properties of the mineral at an electronic level. We calculated the band structures of ZnO and Fe_2O_3 using CASTEP code. The model of ZnO is shown in Figure 5.1 and the calculated band structure along with the density of states (DOS) is shown in Figure 5.3 and Figure 5.4. The optimized lattice parameters of ZnO are a = 3.249270, b = 3.249270, c = 5.205440 which are very close to the experimental values. The model of Fe_2O_3 is shown in Figure 5.2, and the calculated band structure along with the density

of states (DOS) is shown in Figure 5.5 and Figure 5.6. The optimized lattice parameters of Fe_2O_3 are a = 5.419021, b = 5.419021, c = 5.419021 which are very close to the experimental values.
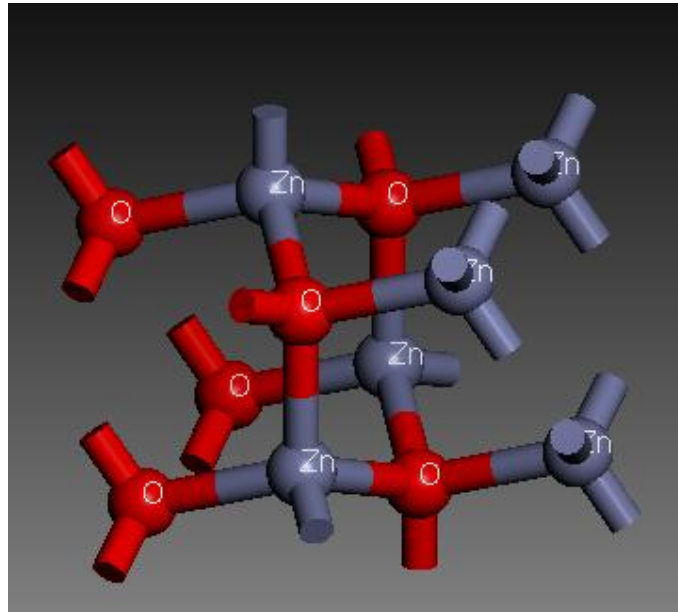
Figure 5.1: The wurtzite structure model of ZnO
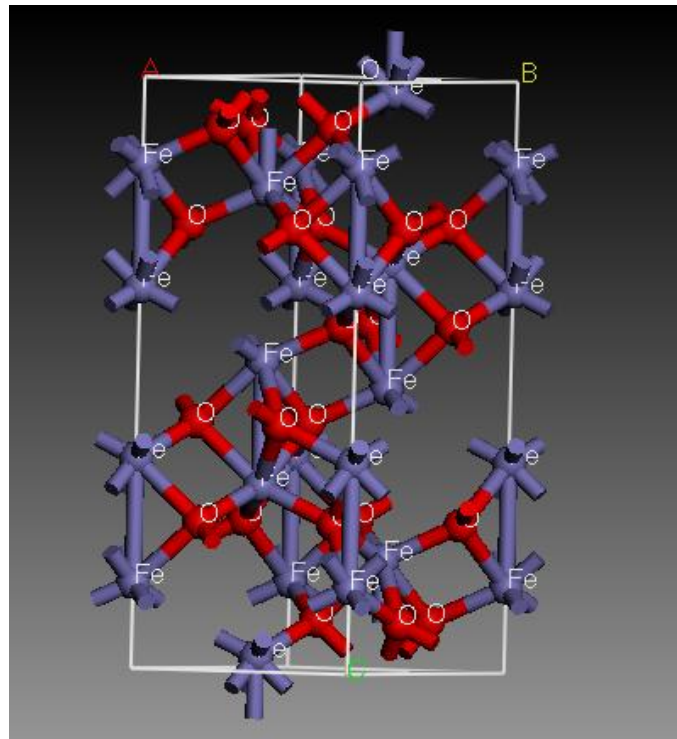
Figure 5.2: Rhombohedrally centered hexagonal model of Fe_2O_3

Figure 5.3 shows the band structure of ZnO. It is observed that the direct band gap is about 0.808 eV at G point, which is in agreement with previous theoretical results. The underestimation of band gap is due to the choice of exchange-correlation energy. It is investigated that the band gap for ZnO calculated with LDA or GGA is about 0.5-1.0 eV. The calculation of band gap using LDA is always larger than the GGA. The valence band mainly consists of the 2p, 2s states of O and 3d state of Zn. O 2p state is predominantly found between -6 and 0 eV in the uppermost valence band as shown in Figure 5.4. But O 2s state is seen in the range from -18.6 to - 16.6 eV, whichis very close to the previous calculated results.

It is observed that due to Zn 3d state, some bands in the energy range of 4-6 eV originated from the valence band maximum (VBM). This is due to splitting and a wave-vector dispersion outside G. Zn 4s state predominates the lowest conduction band. Experimental results also show that it is originated due to O 2p and Zn 4s states. The Fermi energy was set at 0 eV ($E_f = 0$) in the DOS curve. The dielectric constant of the material is related to electronic charge.

The dielectric property of the material represent interaction of the electronic charge in the material with the external electric field. This property shows that adjustment of the electronic charge can shield the external electric field. The highest effective screening can be obtain with larger dielectric constant value. For the adjustment of the electronic charge with effect of external electric field, the movement of the electrons must be easy which shows that each electronic state can change considering the a polarized configuration. Due to the large band gap in the presence of electric field, electronic states in the valence band cannot mix with the electronic states in the conduction band, therefore electrons cannot polarize much and the dielectric constant value is small [135, 136].
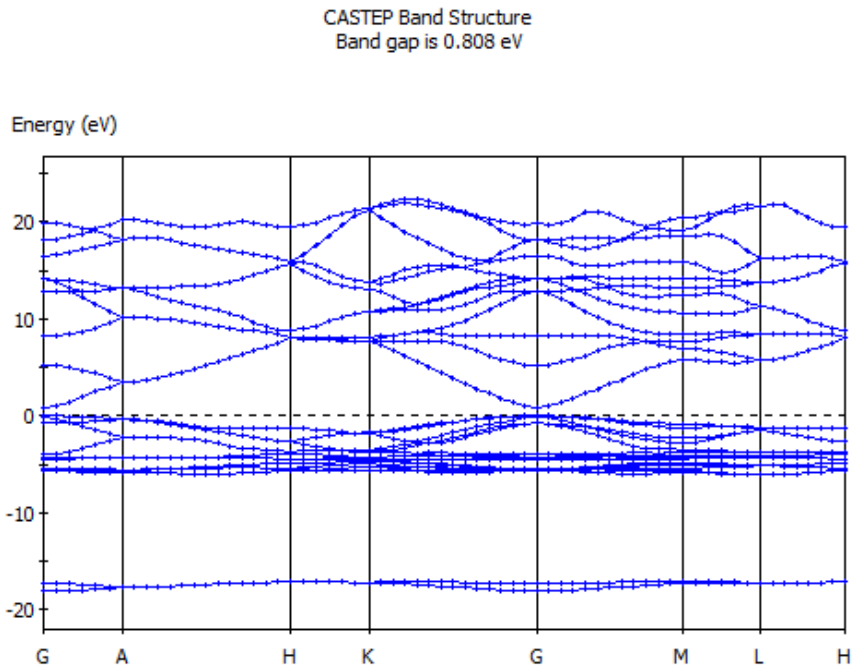
Figure 5.3: The band structure of ZnO
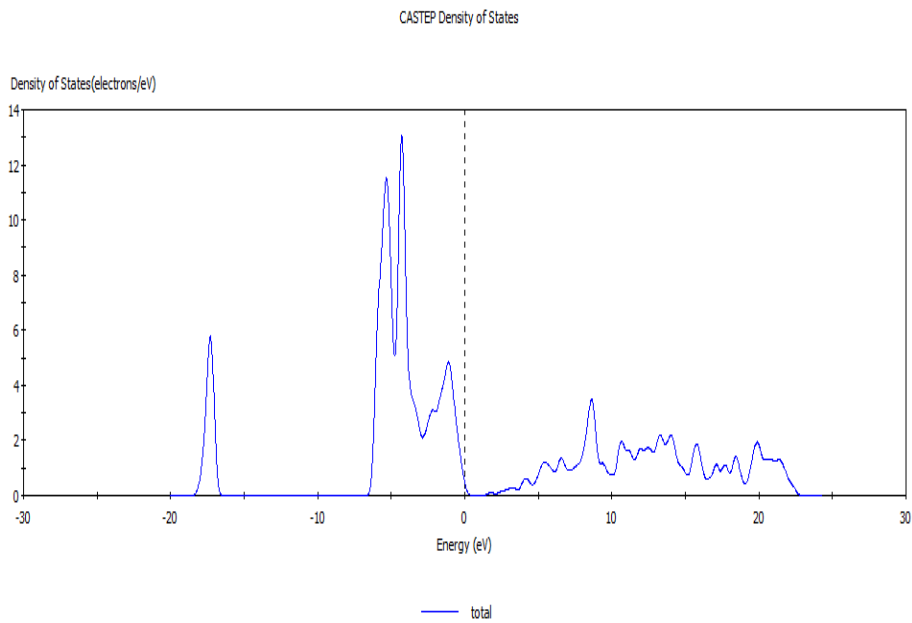
Figure 5.4: The total density of state of ZnO

78

Figure 5.5 shows the band structure of Fe_2O_3. It is observed that the indirect band gap is about 0.201eV; this is a low value as compared to experimental value of 2.1eV. The underestimation of band gap is due to the choice of exchange-correlation energy. The density of states is shown in Figure 5.6 and it is observed that the valence band is a mixture of O 2p state and a majority of Fe 3d state orbitals, while the conduction band consists of small amount of Fe 3d state orbitals. The upper part of the valance band ranges from 0 to -9ev and the lower part ranges from -16 to -20ev. The states of Fe 3d and O 2p are strongly hybridized so the ranges in the valance band are contributed by the electronic states of oxygen and iron, which cannot be separated from each other. It is observed that in the valance band, the contribution of Fe 3d state is two times larger than the O 2p state in each range because the ionization cross section of O 2p is less than the ionization cross section of Fe 3d. The upper edge of the valance band is dominated mainly by O 2p state, but the lower part of the conduction band is mainly dominated by Fe 3d state.

Due to the small band gap in the presence of electric field, electronic states in the valence band easily mix with the electronic states in the conduction band, therefore electrons can polarize much and the dielectric constant value is large. Therefore we obtain highest effective screening with larger dielectric constant value [135, 136].
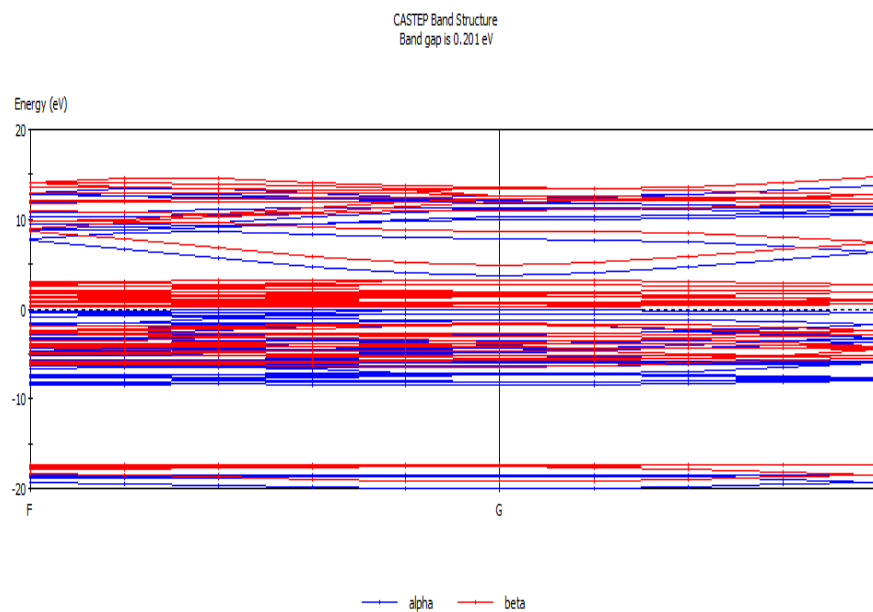
Figure 5.5: The band structure of Fe_2O_3
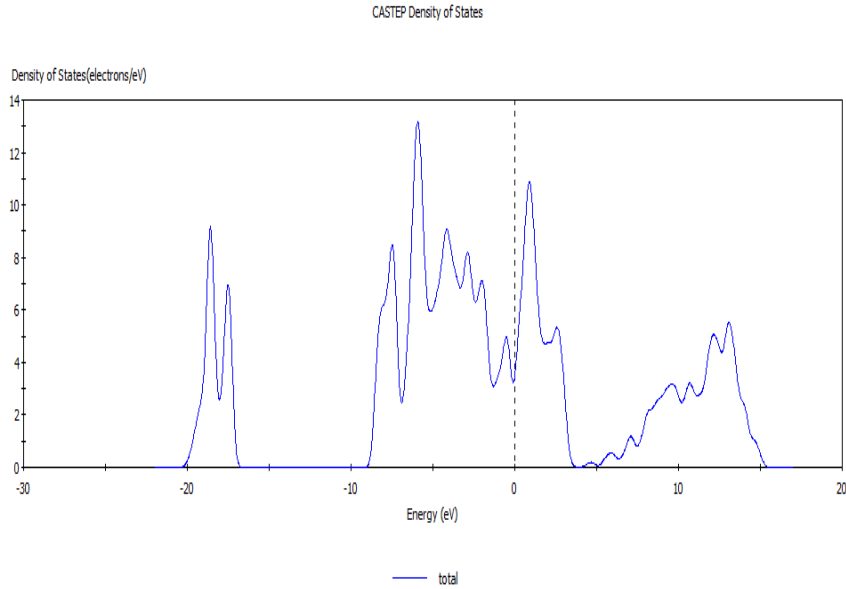
Figure 5.6: The total density of state of Fe_2O_3

5.2 Characterization of Nanoparticles

In this section, the results of the characterizations of zinc oxide and iron oxide samples by XRD, FESEM, HRTEM and magnetic measurements are presented. Also included in this section are the preparation of the zinc oxide and iron oxide nanofluids and the interfacial tension measurement.

5.2.1 Characterization of Zinc Oxide (ZnO) Nanoparticles

Figure 5.7 shows the XRD patterns of ZnO- nanoparticles with their plane number. The peak positions at $2\theta = 31.85^o$, 34.29^o, 36.18^o, 47.55^o, 56.63^o, 62.85^o, 66.38^o, 68.00^o and 69.22^o are assigned to (100), (002), (101), (102), (110), (103), (200), (112) and(201) which show good agreement with those of the JCPDS (card no 80-0075) data of the zinc oxide (ZnO)with hexagonal wurtzite phase (lattice constants a) 3.242 Å and c) 5.176 Å) [137, 138]. The crystallinity of ZnO increases with increasing temperature. The average particles size in nanometers, 'D' was determined by means of an X-ray line-broadening method using Scherer equation

80

$$D = \frac{0.9\lambda}{\omega\cos\theta} \qquad\qquad (5.1)$$

Where,

θ = Bragg's angle, ω = full width at half maximum (FWHM), λ = wavelength of incident radiation, 0.9 = shape factor for the metal oxide. The results show that the ZnO nanoparticles have with an average particle size of 30-39 nm.
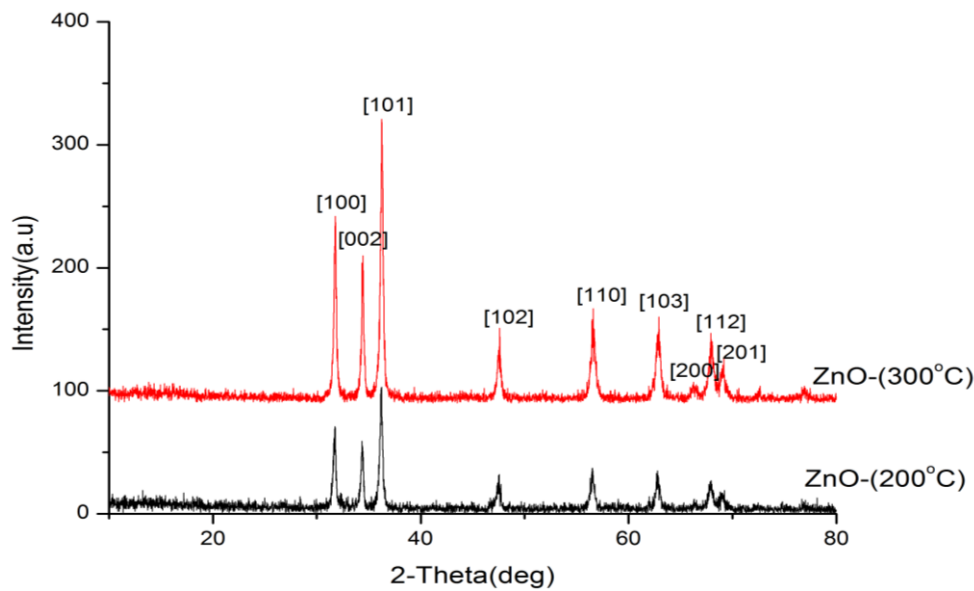
Figure 5.7: XRD patterns of ZnO nanoparticles annealed at different temperatures (200-300°C)

As shown in Table 5.1, it is observed that there is a small change in the lattice parameters when the sintering temperature is increased. The change in lattice parameter can be affected by free charge, impurities, stress, particle size, quantum size effects and temperature. It is also observed that from the angle values, the ZnO crystal structure is hexagonal. There is an increase in d-spacing with increasing temperature.

Table 5.1: d-spacing, lattice parameter, angles of ZnO nanoparticles sintered at different temperatures

Sample	d space (Å)	lattice parameter			α^o	β^o	γ^o	Reference card
		(a)	(b)	(c)				
ZnO 200ºC	2.475	3.250	3.250	5.207	90	90	120	79-2205(C)
ZnO 300ºC	2.473	3.249	3.249	5.205	90	90	120	89-0511(C)

5.2.1.1 FESEM and EDX Results of Zinc Oxide (ZnO)

Field emission scanning electron microscopy (FESEM) is used to obtain the morphology of nanoparticles and the grain size of the samples. The FESEM graphs of zinc oxide (ZnO) samples annealed at 200ºC and 300ºC are shown in Figures 5.8 (a) and (b). From the graphs, it is observed that most of the nanoparticles are agglomerated with other nanoparticles. The average grain size of the samples annealed at 200ºC and 300ºC is 31.32 nm and 51nm respectively. The grain size increases as the temperature increases from 200ºC to 300ºC.

The EDX spectra in Figure 5.9 shows feature peaks that match the peaks of Zn and O elements, which illustrate the specific composition of ZnO nanoparticles. No contamination in the samples was found as indicated by the EDX analysis.

Table 5.2 shows the weight percentage, atomic percentage and percentage difference for ZnO at 200°C and 300°C temperatures. EDX analysis shows that there is a high deviation in weight percentage for zinc oxide samples sintered at 200°C and 300°C, however a low deviation was observed for the zinc oxide sample annealed at 200°C.
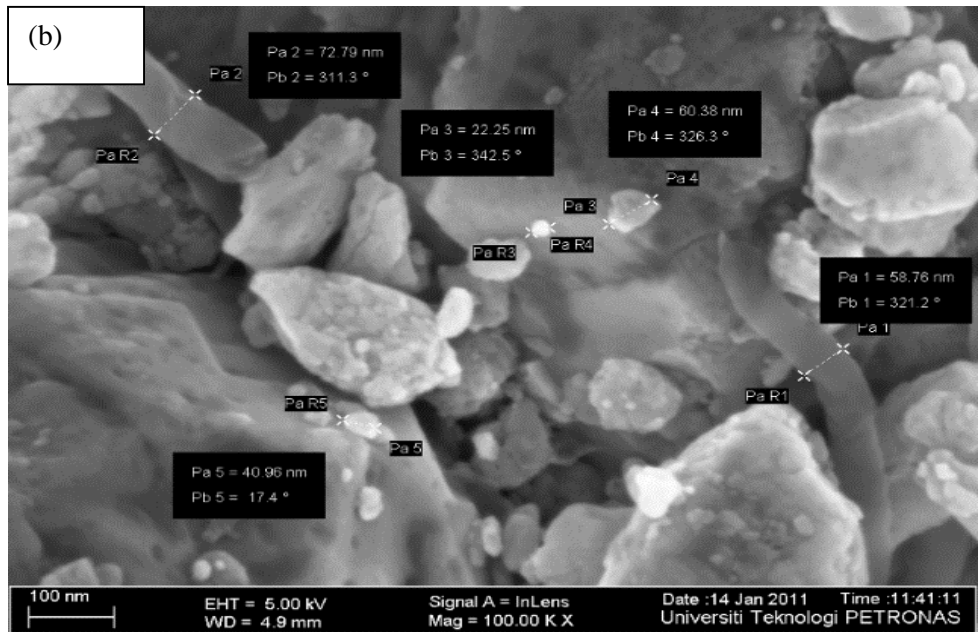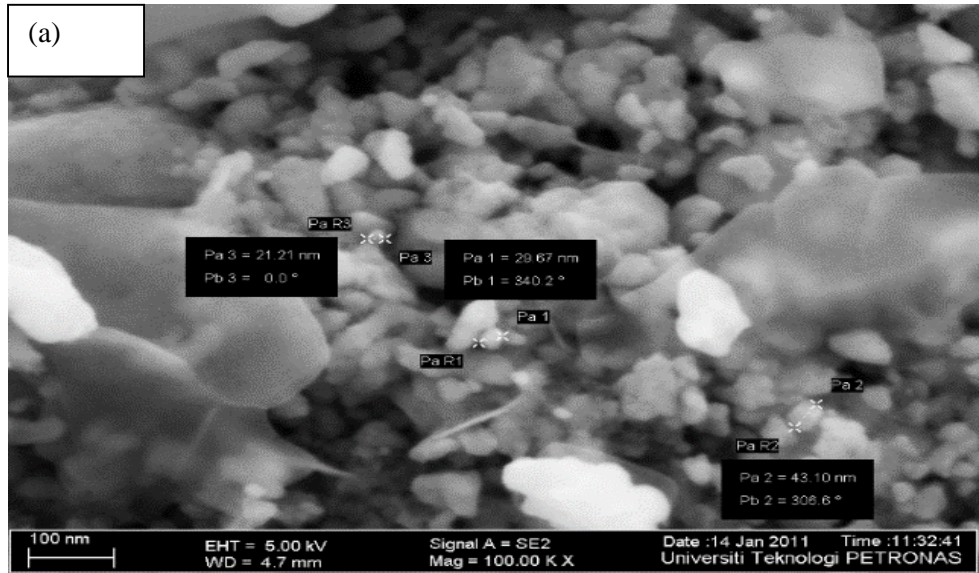
Figure 5.8: FESEM images of ZnO nanoparticles annealed at temperatures (a) 200°C and (b) 300°C
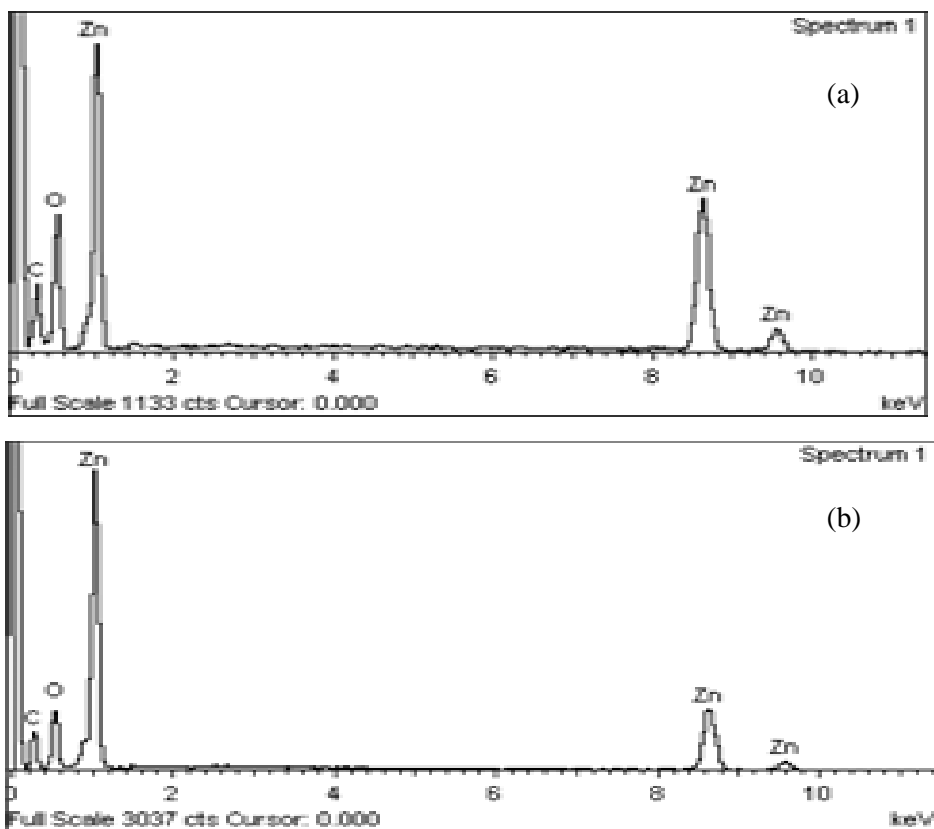
Figure 5.9: EDX analysis of ZnO nanoparticles annealed at temperatures (a) 200°C

and (b) 300°C

Table 5.2: EDX data and percentage difference for ZnO at 200°C and 300°C

Sample	Element	Measured weight (%)	Standard atomic weight (g/mol)	Theoretical percentage of weight (%)	Percentage difference (%)	Measured atomic ratio	Theoretical atomic ratio	Percentage difference (%)
200°C	O	21.84	15.99	19.66	11.08	30.54	50.00	38.92
	Zn	50.08	65.38	80.34	37.66	17.14	50.00	65.72
300°C	O	21.63	15.99	19.66	10.02	28.21	50.00	43.58
	Zn	45.52	65.38	80.34	43.34	14.49	50.00	71.02

5.2.1.2 Transmission Electron Microscope (HRTEM) Results

Figure 5.10 (a) and (b) shows high resolution transmission electron microscope (HRTEM) images of zinc oxide (ZnO)) prepared by the sol gel method. The HRTEM results show that for zinc oxide (ZnO), single phase with good crystallinity was achieved at the sintering temperature of 300ºC; the average size of the ZnO nanoparticles is 34.50 nm.
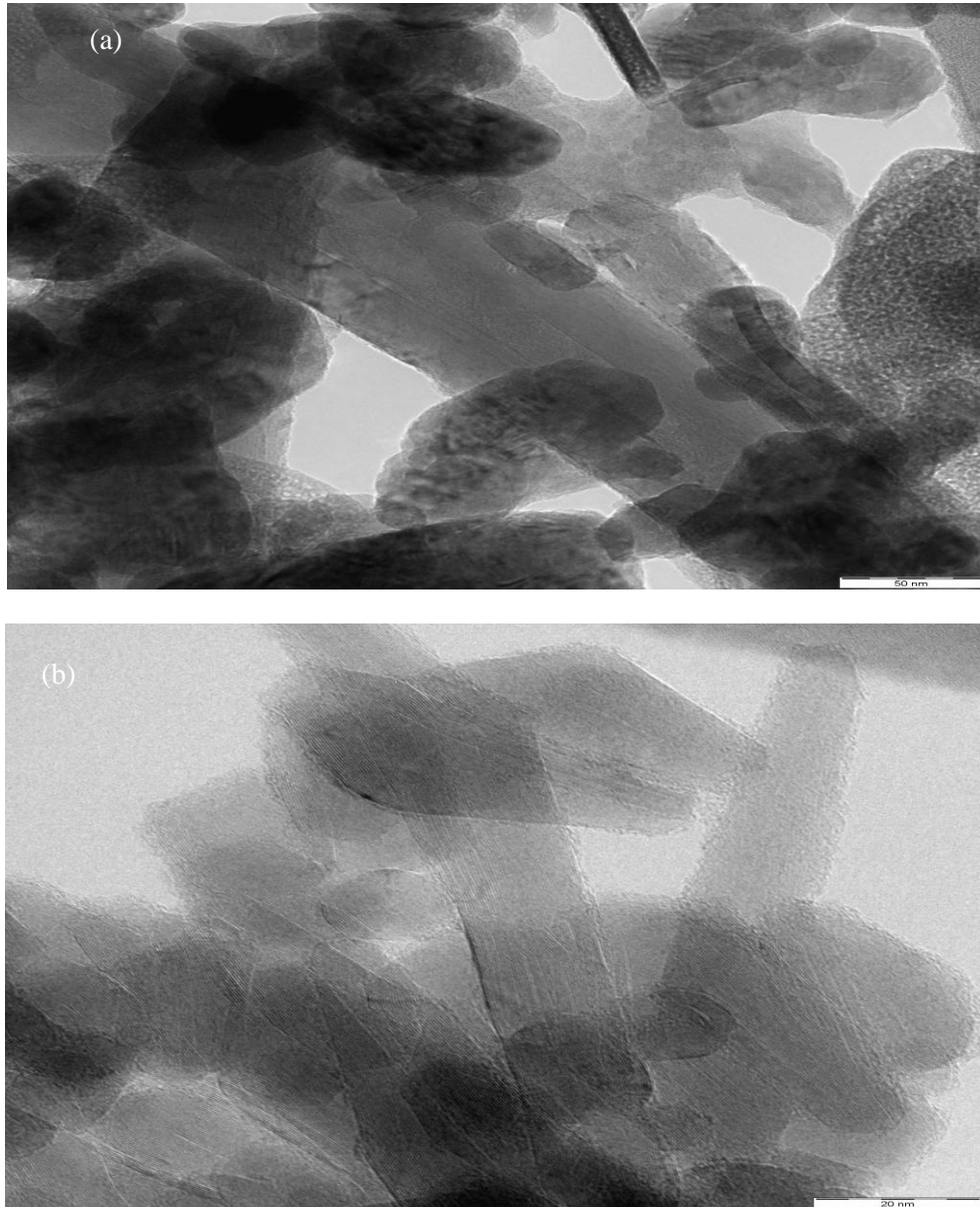
Figure 5.10: HRTEM images of ZnO nanoparticles annealed at temperature (a) 200°C and (b) 300°C

5.2.2 Iron Oxide (Fe_2O_3) Nanoparticles Characterization

The XRD results of iron oxide (Fe_2O_3) nanoparticles sintered at temperature 300°C, 400°C and 500°C are shown in Figure 5.11. The reference patterns are displayed below. Each pattern correlates well with the values of 2θ as well as the relative intensities of each peak signifying the presence of the respective hematite particles. The 2θ (relative intensity) value of three highest peak of the [104], [110], and [116] lines of the sample is 33.3, 35.76, and 54.34, respectively [139].

The XRD patterns show that the samples have a single-phase structure at 400°Cand 500°C. The crystallite size was measured from the X-ray diffraction patterns by using the Debye-Scherer formula as given in Equation 5.2 below,

$$D = \frac{0.9\lambda}{\omega\cos\theta}$$
(5.2)

Where,

k= varies with hkl & crystallite size equal to 0.9.

θ = Bragg's angle.

ω = Full width at half maximum (FWHM).

λ = wavelength of incident radiation.

The crystallite size of iron oxide (Fe_2O_3) samples obtained are 30.27 nm, 34.10 nm and 37.60 nm at 300°C, 400°C and 500°C respectively. It is clear that the crystallite size increased as the sintering temperature was increased from 300°C to 400 and 500°C. Analysis of the XRD patterns showed a single phase crystal structure of iron oxide (Fe_2O_3) with a maximum intensity peak.

Hematite crystal structure contains an organization of Fe^{3+} ions in octahedral coordination with oxygen in hexagonal closest-packing, which consists of no net magnetization. Consequently, there is a loss of magnetic response due to the formation of antiferromagnetic oxides.
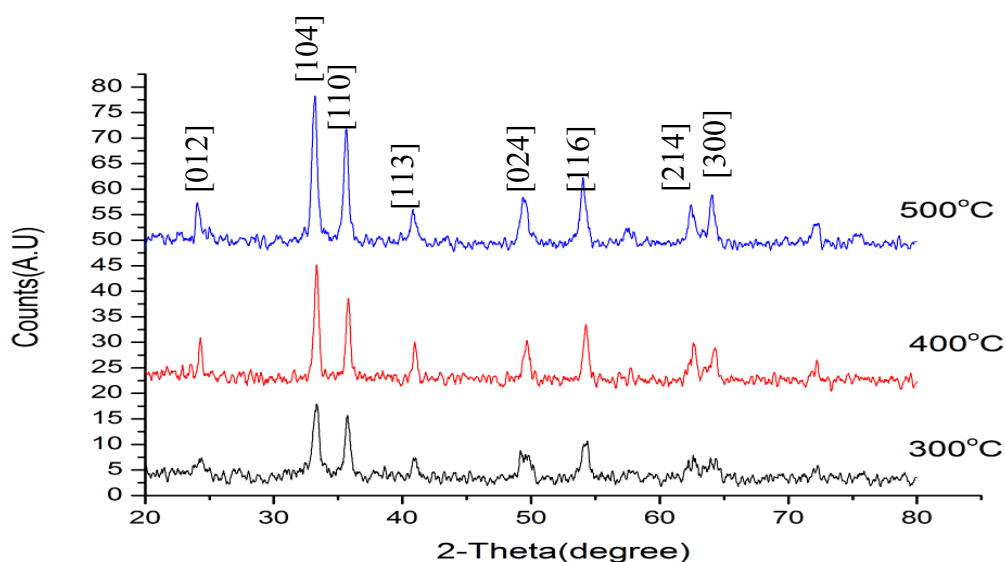
Figure 5.11: XRD results of iron oxide (Fe_2O_3) nanoparticles sintered at temperatures 300°C, 400°C and 500°C.

As shown in Table 5.3, it is observed that there is a small change in the lattice parameters when the sintering temperature is increased. It is also observed that from the angle values, the iron oxide (Fe_2O_3) crystal structure is hexagonal. There is an increase in d-spacing with increasing temperature.

Table 5.3: d-spacing, lattice parameter, angles of iron oxide (Fe_2O_3) nanoparticles sintered at different temperatures

Sample	d space (Å)	lattice parameter			α^o	β^o	γ^o	Reference card
		(a)	(b)	(c)				
Iron oxide 300ºC	2.680	5.032	5.032	13.733	90	90	120	89-0599 (C)
Iron oxide 400ºC	2.686	5.031	5.031	13.737	90	90	120	13-0534 (D)
Iron oxide 500ºC	2.697	5.038	5.038	13.772	90	90	120	24-0072 (D)

87

5.2.2.1 FESEM and EDX Results of Iron Oxide (Fe₂O₃)

Field emission scanning electron microscopy (FESEM) is used to obtain the morphology of nanoparticles and the grain size of the samples. The FESEM graphs of iron oxide (Fe_2O_3) samples annealed at 300ºC, 400ºC and 500ºC are shown in the Figures 5.12 (a), (b) and(c). From the graphs, it is observed that most of the nanoparticles are agglomerated with other nanoparticles due to high surface energy of the nanoparticles and large surface area. However, there is no agglomeration of the nanoparticles sintered at 500ºC which shows uniform grain structure. The average grain size of the sample annealed at 300ºC, 400ºC and 500ºC is 17.21nm, 22.41nm and 38.09 nm respectively. The grain size increased as the temperature was increased from 300ºC to 500ºC.
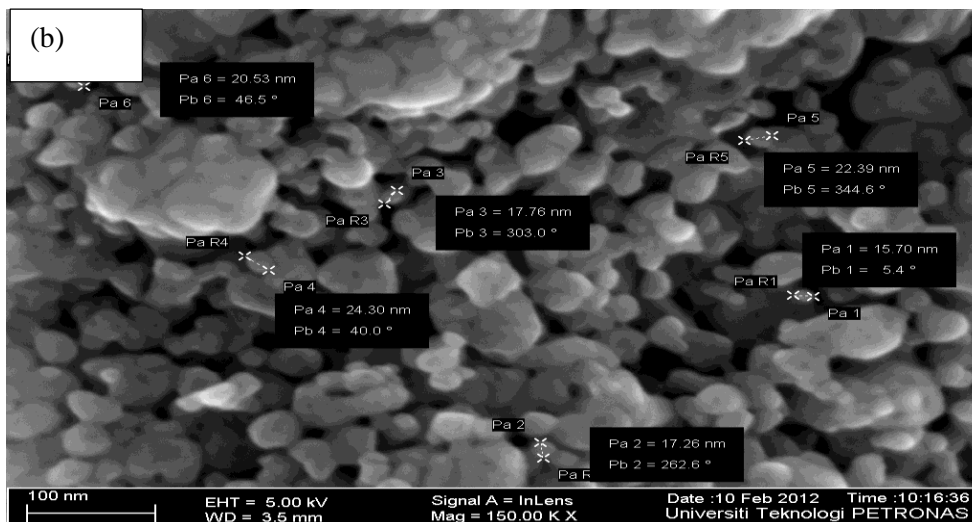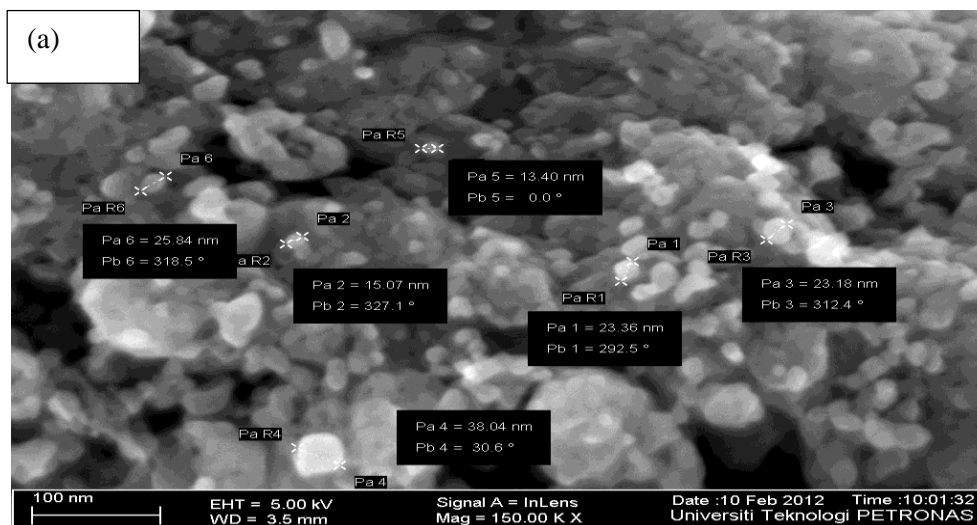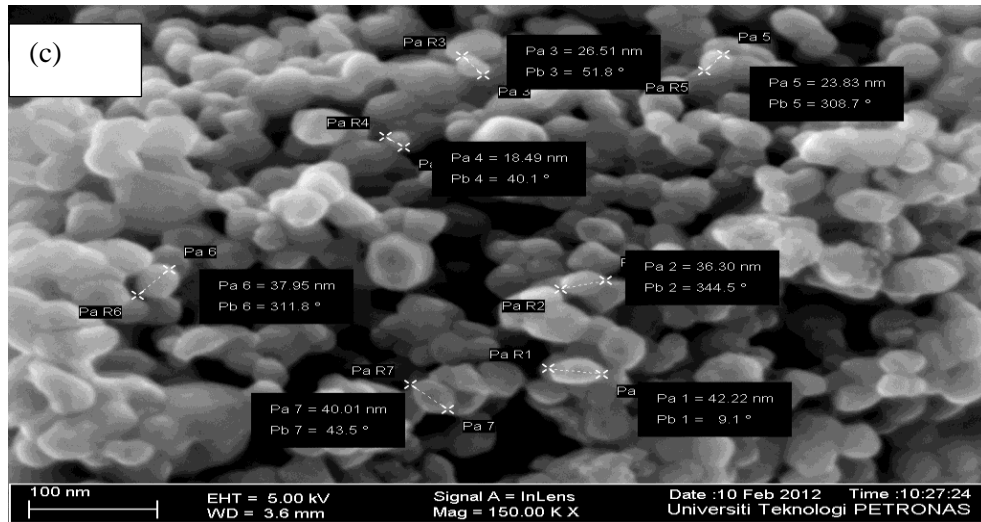
Figure 5.12: FESEM images of Fe_2O_3 annealed at (a) 300°C, (b) 400°C and (c) 500°C

5.2.2.2 EDX Results of Iron Oxide (Fe₂O₃) Samples

The EDX results of iron oxide (Fe_2O_3) show that the iron and oxygen atoms are in the percentage of 51% and 49% respectively at 300ºC. While the percentages of the iron and oxygen atoms are 44.11% and 55.89% at 400ºC and 35.24% and 64.76% at 500ºC respectively. It is observed that there is no impurity detected due to high purity of the starting materials used for synthesizing the samples as shown in Figure 5.13.

The EDX analysis shows, that only Fe and O elements are present with low standard deviation as shown in Table 5.4

.

89

(a)

(b

(c)
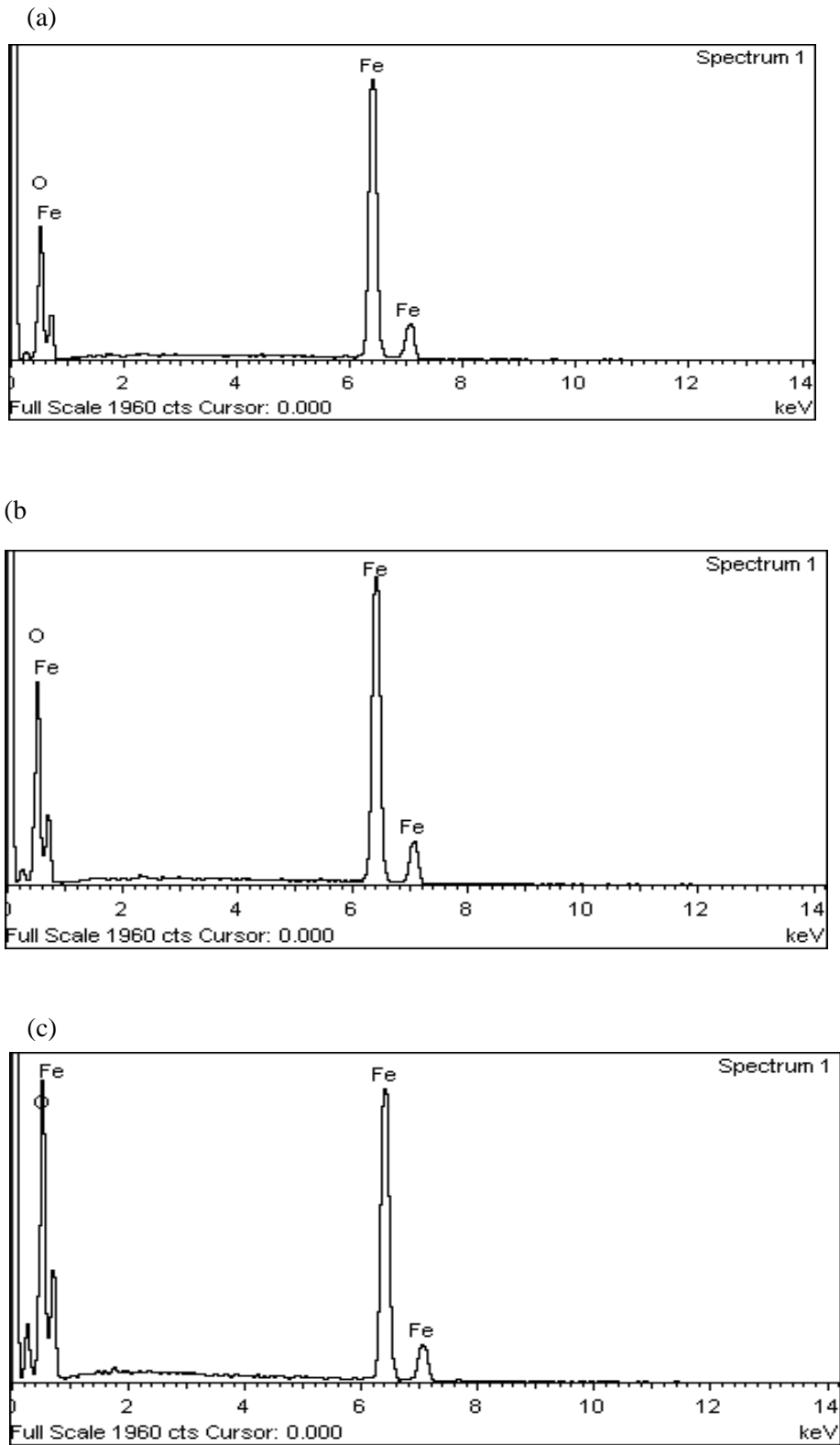
Figure 5.13: EDX analysis of Fe_2O_3 annealed at (a) 300°C, (b) 400°C and (c) 500°C

Table 5.4: EDX data and percentage difference for iron oxide at 300°C, 400°C and 500°C

sample	Element	Measured weight (%)	Measured atomic ratio (%)	Standard deviation (%)
300ºC	O	21.58	49	18.33
	Fe	78.42	51	27.50
400ºC	O	26.63	55.89	6.85
	Fe	73.37	44.11	10.27
500ºC	O	34.49	64.76	7.93
	Fe	65.51	35.24	10.55

5.2.2.3 High Resolution Transmission Electron Microscope (HRTEM) Results

Figure 5.14 shows the high resolution transmission electron microscope (HRTEM) images of iron oxide (Fe_2O_3) prepared by the sol gel method. The HRTEM results show that for iron oxide (Fe_2O_3), single phase with the best crystallinity was attained at the sintering temperature of 500ºC. The average grain size varies between 20nm to 37nm.
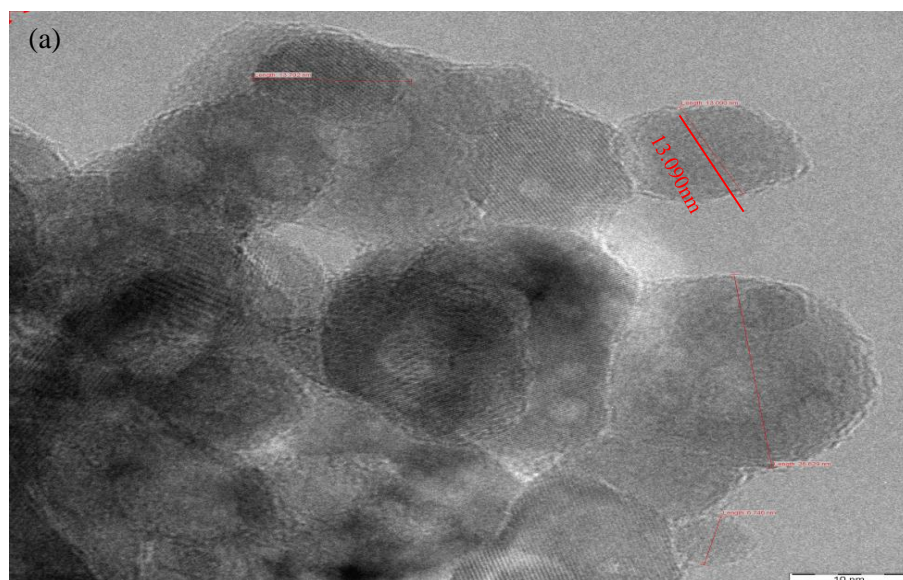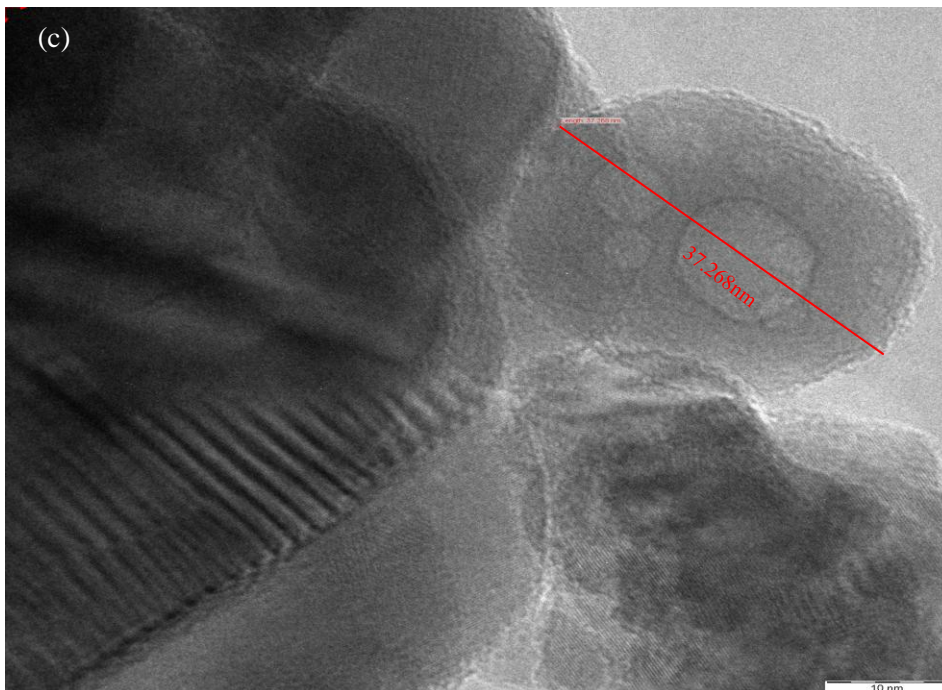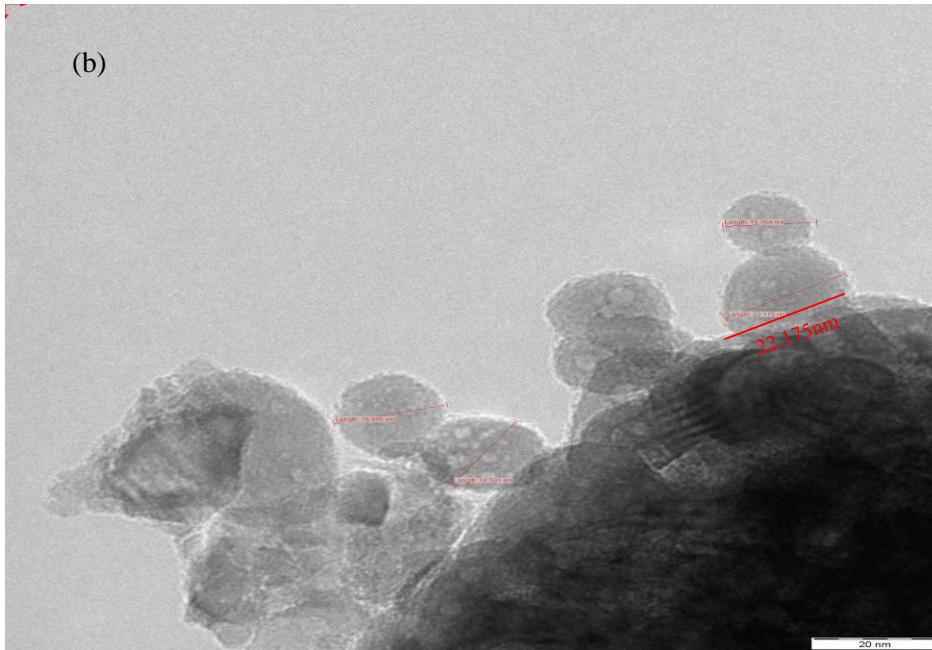
Figure 5.14: TEM images of Fe$_2$O$_3$ annealed at (a) 300°C, (b) 400°C and (c) 500°C

5.2.3 Magnetic Measurements Results

Magnetic properties of the iron oxide (Fe_2O_3) samples such as initial permeability, Q-factor and loss factor of iron oxide (Fe_2O_3) samples were measured using the impedance LCR meter. These properties were measured from a series inductance (L_s) and Q values. Initial permeability is a significant property to observe the qualities of magnetic materials. It is influenced by the morphology, grain size, single phase structure, bulk density, porosity, and spin rotational contributions.

The initial permeability μ_i was calculated by using the following formula.

$$\mu_i = \frac{2\pi L_s}{N^2 \mu_o t \ln\left(D_o / D_i\right)} \tag{5.3}$$

Where L_s is the series inductance, μ_o is the magnetic permeability, D_o is the outer diameter of the toroid, D_i is the inner diameter of the toroid, 'N' is the number of turns and 't' is the thickness of the toroid. As the grain size increased the initial permeability increased in all samples. Figures 5.15 (a), (b) and (c) show the initial permeability, Q factor and relative loss factor of iron oxide (Fe_2O_3) powders in the toroidal form and sintered at 400°C and 500°C. High values of initial permeability and Q-factor were obtained for samples sintered at 500°C, and a low loss factor was observed for sample sintered at 500°C as compare to sample sintered at 400°C.

The loss factor decreases at a higher frequency but the initial permeability increases as shown in Figure 5.15 (a). The relative loss factor decreases up to 10 MHz, and after this it remains smooth for the iron oxide (Fe_2O_3) samples sintered at 400°C and 500°C. The relative loss factor is the ratio of the tanδ to the initial permeability and can be calculated by the following equation given below.

$$RLF = \frac{1}{\mu_i Q} \tag{5.4}$$

The relative loss factor of iron oxide (Fe_2O_3) samples sintered at 400°C and 500°C is higher at low frequency whereas it decreases as the frequency increases as shown in Figure 5.15 (b).
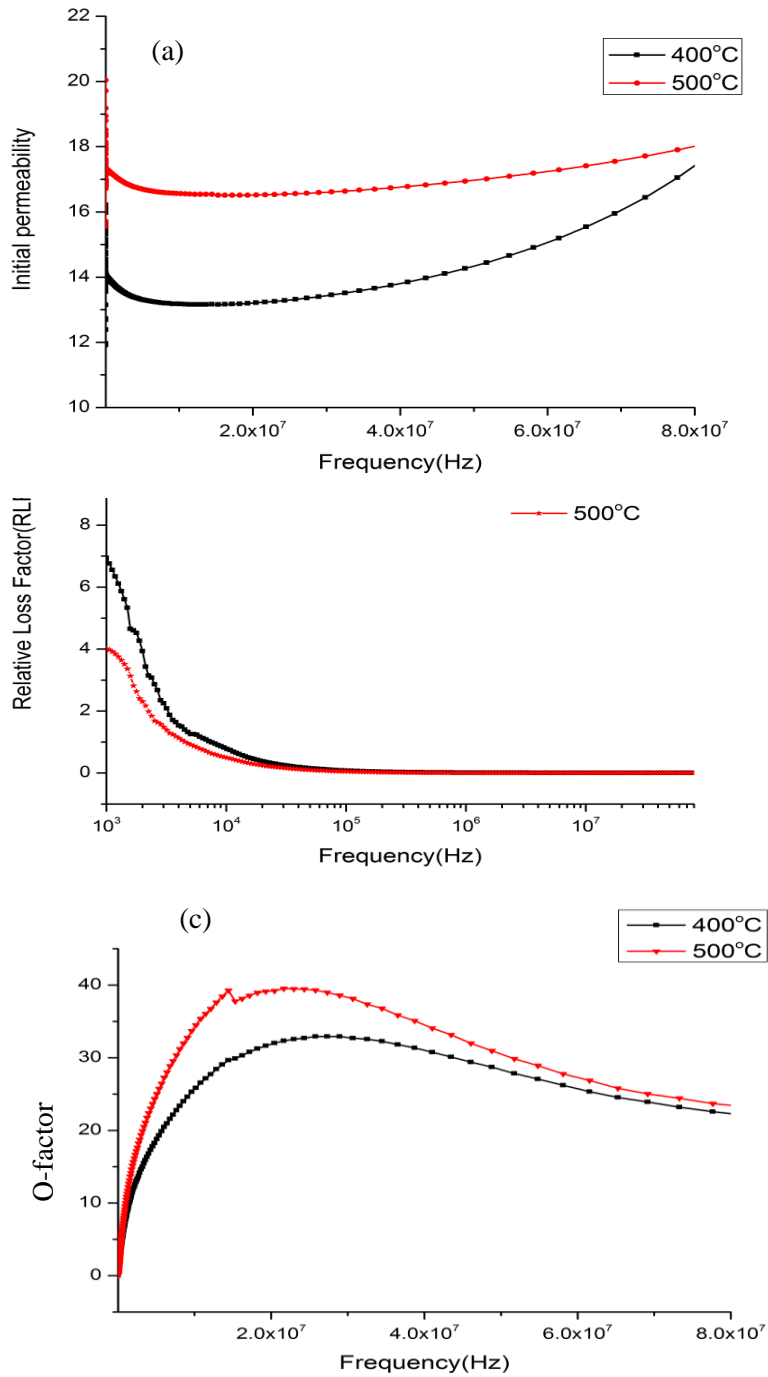
Figure 5.15: (a) Initial permeability (b) relative loss factor and (c) Q-factor of iron oxide (Fe_2O_3) samples annealed at 400°C and 500°C

5.3 Vibrating Sample Magnetometer (VSM) Results

Magnetic properties of the synthesized samples of Fe_2O_3 nanoparticles are studied by using vibrating sample magnetometer (VSM). Figure 5.16 and Figure 5.17 represent the magnetic saturation (Ms) vs. applied magnetic field (B) for Fe_2O_3 nanoparticles at room temperature. The applied magnetic field ranges from +20000 to -20000.

It is observed that magnetization increases with increasing magnetic field and saturates at higher magnetic fields. If the magnetic field is very strong, the magnetic moments of all particles in the field will orient themselves in the direction of the applied field direction giving rise to saturation of magnetization. The magnetic saturation (Ms), magnetic remanent (MR), and coercivity (Hc) were measured and calculated from the hysteresis loop. The values for the sample synthesized at 400°C are coercivity (Hci) = 57.246 G, area = 1551 erg, magnetization (Ms) = 7.7484 emu and retentivity (Mr) = 63.830×10^{-3} emu. The values for the sample synthesized at 500°C are coercivity (Hci) = 32.271 G, area = 0.61306 erg, magnetization (Ms) = 8.5729 emu and retentivity (Mr) = 38.497×10^{-3} emu. The percentage difference of saturation magnetization is 10.64%, which shows that with increasing particle size the magnetic saturation also increases. As the sample synthesized at 500°C has larger particle size, as confirmed from XRD results, compared to the sample synthesized at 500°C, so the sample at 500°C has high magnetic saturation.

As the magnetic field decreases, the saturation magnetization decreases from plateau and becomes zero when the applied magnetic field is zero. This shows that the magnetic moments of the nanoparticles which consist of single-crystal domains are aligned. The reduction of magnetization with particles size is due to the small-particle surface effect. The disorientation of atomic spins on the particle surface is due to reduced coordination and broken exchange bonds between surface spins. As a result the sum of misaligned surface spins is comparatively unresponsive to the applied magnetic field, with some of the surface spins being disoriented even at high magnetic fields. This surface effect is very noticeable for nanosized particles because of their large surface-to-volume ratio.
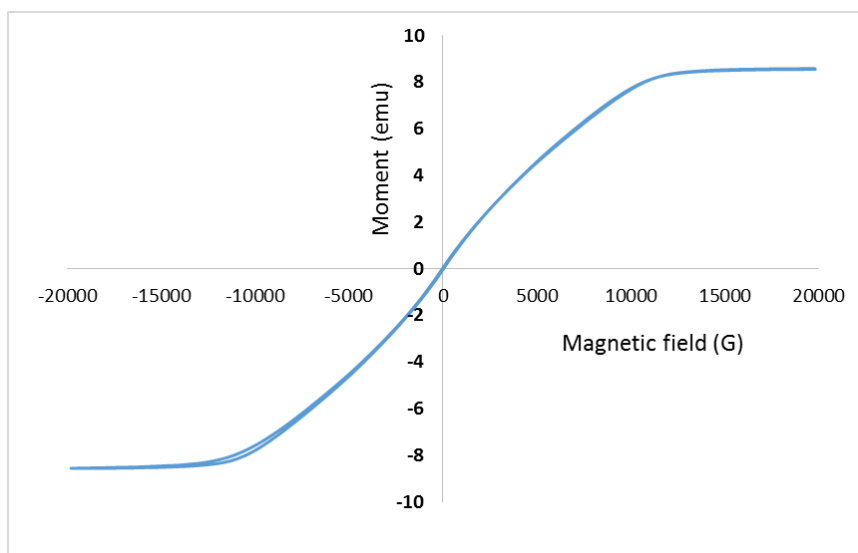
Figure 5.16: VSM results of iron oxide sample at 500°C
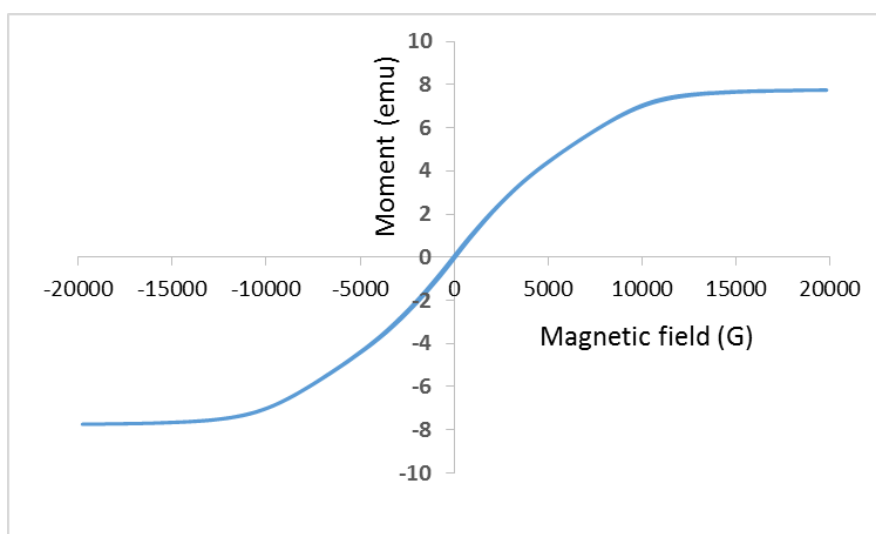
Figure 5.17: VSM results of iron oxide sample at 400°C

5.3.1 Summary

ZnO and iron oxide (Fe_2O_3) nanoparticles were prepared using the sol-gel method. The XRD results of the ZnO and iron oxide (Fe_2O_3) showed a single phase structure with a [101] and [104] major peak respectively. The particle size of the ZnO and iron oxide (Fe_2O_3) nanoparticles is in the range of 30-39 nm and 30.27-37.60nm respectively. FESEM and HRTEM images showed that the samples have good crystallinity and the grain size increased as temperature increased. Iron oxide (Fe_2O_3) samples sintered at

500°C showed a high initial permeability, Q-factor and low loss factor as compared to samples sintered at 500°C. From the hysteresis loop, it was observed that iron oxide (Fe_2O_3) samples sintered at 500°C showed a 10.64% high magnetic saturation (Ms) as compared to the sample sintered at 400°C. The sample had a very high initial permeability and low loss at low frequencies; due to this, it was suitable for the preparation of the nanofluid and oil recovery applications.

5.4 Interfacial Tension (IFT) Measurement of Nanofluids

For IFT measurements of the fluids, reliable density data was required. The refractive index (RI) for a denser phase was also required. Since brine is denser than fluid, therefore the RI of brine can be used in the IFT measurements. The RI of brine was measured at 60°C by refractometer and its value is 1.3323. The density of brine and crude oil without nanofluids were measured at 60°C. The IFT measured at the equilibrium condition is shown in Figure 5.18 and Figure 5.19. The nanofluids were prepared in different concentrations of 0.001%, 0.005% and 0.1% with 0.05% SDS as surfactant. As light increase in IFT was noticed i.e. it can be seen that there is an increase in IFT to some extent as the concentration of the nanoparticles was increased from 0.001% to 0.1%. The interfacial tension increased to 19.77% for iron oxide (Fe_2O_3) and 9.19% for ZnO.
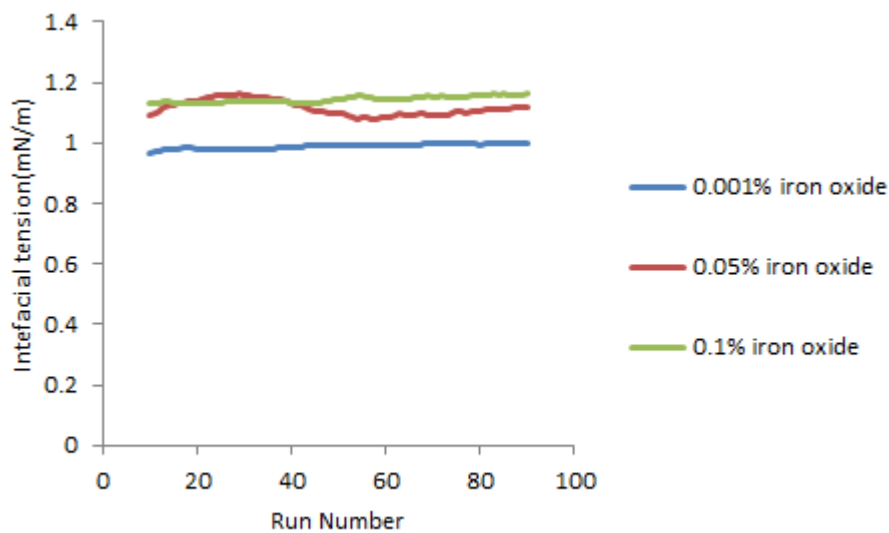
Figure 5.18: Interfacial tension values of the iron oxide (Fe_2O_3)

At the early stages of adsorption of the nanoparticles, the interfacial tension increases and then it reaches equilibrium state after some time.
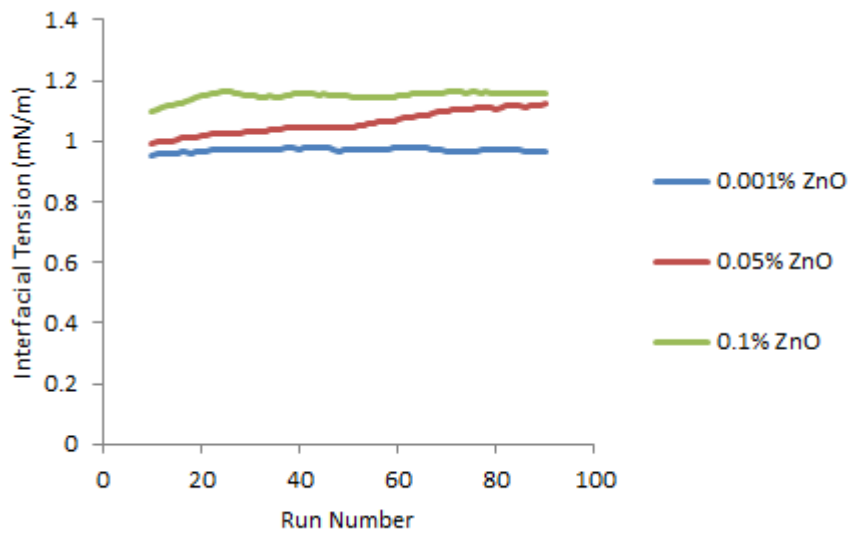
Figure 5.19: Interfacial tension values of the ZnO nanofluids

At the equilibrium stage, the adsorption and desorption of nanoparticles becomes equal. Iron oxide nanoparticles have large nanoparticle size compared to the ZnO nanoparticles as observed from XRD analysis, thus the ZnO nanoparticles with smaller size has smaller rate of adsorption. This phenomenon can be described as follows; due to the agglomeration of nanoparticles at the oil/water (o/w) interface, the total free energy decreases. The initial high interfacial energy E_o, between oil (O) and water (W) can be decreased to E_1. A change of ΔE_1 by the settlement of one nanoparticle with an effective radius 'r' at the interface ΔE_1 is given below [140].

$$E_o - E_1 = \Delta E_1 = -\frac{\pi r^2}{\gamma_{O/W}}\left[\gamma_{O/W} - \left(\gamma_{P/W} - \gamma_{P/O}\right)\right]^2$$

(5.5)

It can be observed that there are three types of interfacial energy that rise from the particle/oil $\gamma_{P/O}$, the particle/water $\gamma_{P/W}$, and the oil/water interfaces $\gamma_{O/W}$. From equation 5.5, it is observed that for a specified system with permanent $\gamma_{P/O}, \gamma_{P/W}$, and $\gamma_{O/W}$ at the same temperature effect in terms of k_{BT}, the stability of the particle

gathering increases with increasing 'r' [140]. The total free energy gained by smaller particles is lower. Therefore, the interfaces with larger particles are more stable.

5.5 Magnetic Field Measurement around Glass Bead Packed Column

The schematic diagram of the experimental setup of the enhanced oil recovery is shown in Figure 5.20 which consists of glass bead packed column and three magnetic field sensor. Figure 5.21 represents the magnetic field measurement using three sensors around the glass bead packed column. The three sensors were placed at three different positions on the column i.e.R_x-1 which is on top, R_x-2 which is at the center and R_x-3 which is at the bottom position. The magnetic field value at the top position (R_x-1) was 74.37 % more than at the (R_x-2) center position of the column. The magnetic field value at the top position (R_x-1) is 98 % more than the bottom position (R_x-3) of the sensor. When the glass bead packed column saturated with oil and brine was placed at the center in the front of the antenna, a decrease in magnetic field strength was observed. This shows that glass bead packed column saturated with oil and brine can absorb electromagnetic waves. When the magnetic field sensor was placed at the top position of the column, the magnetic field strength measured was larger than at the bottom position. The strength of the magnetic field decreases due to the skin depth of electromagnetic waves.
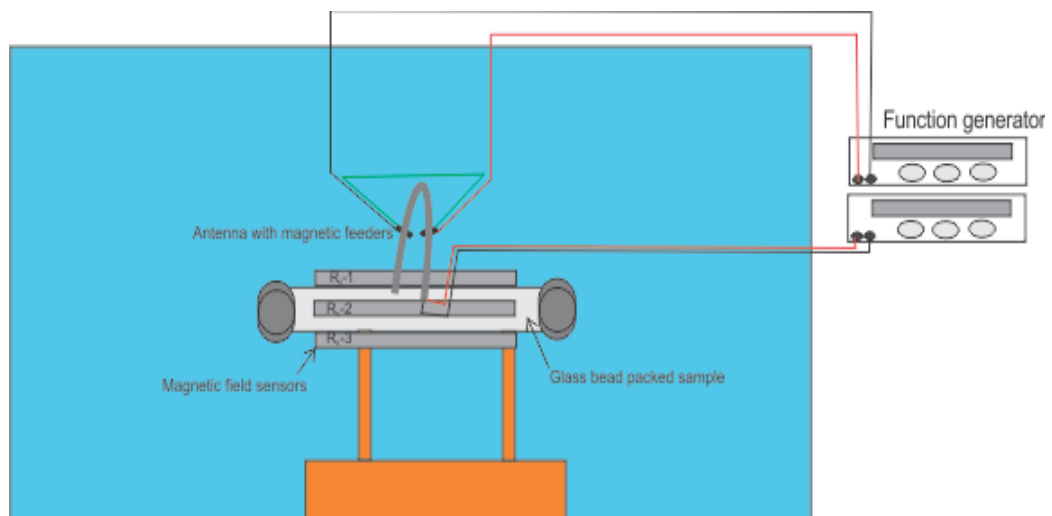
Figure 5.20: Schematic diagram of experimental setup for magnetic field measurement with three sensors
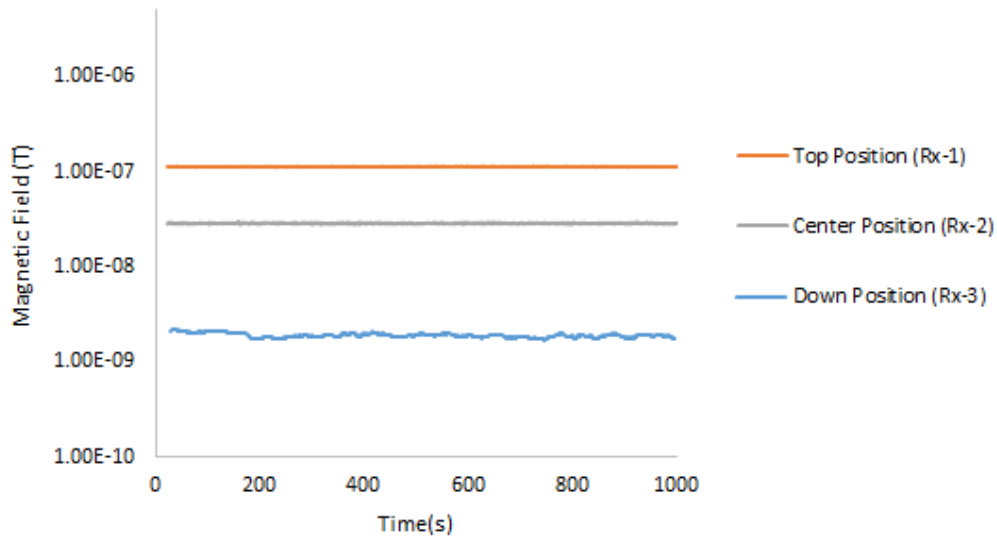
Figure 5.21: Magnetic field strength at three positions around the glass bead packed column

The electromagnetic waves emitted from the antenna can be understood by looking at the radiation pattern of the antenna. An antenna radiation pattern is a graphical representation of the radiation characteristics of the antenna as a function of space coordinates. The simulated radiation patterns of the antenna are presented in Figure 5.22 and Figure 5.23. From the results, it can be seen that the E-field and H-field radiation patterns of the antenna are directional. Figure 5.22 depicts the E-field radiation patterns for the antenna, where it has a main lobe magnitude of 2.44×10^{-15} V/m at 30MHz, and a main lobe direction in 177 degree.
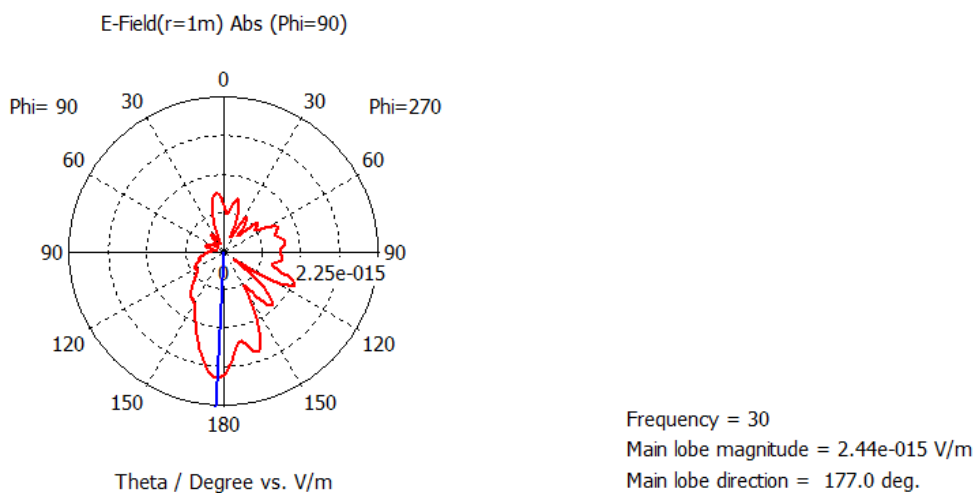
Figure 5.22: E-field radiation pattern of antenna

Figure 5.23 depicts the H-field radiation patterns for the antenna, where it has a main lobe magnitude of 5.8×10^{-17} A/m at 30MHz, and a main lobe direction in 177 degree.
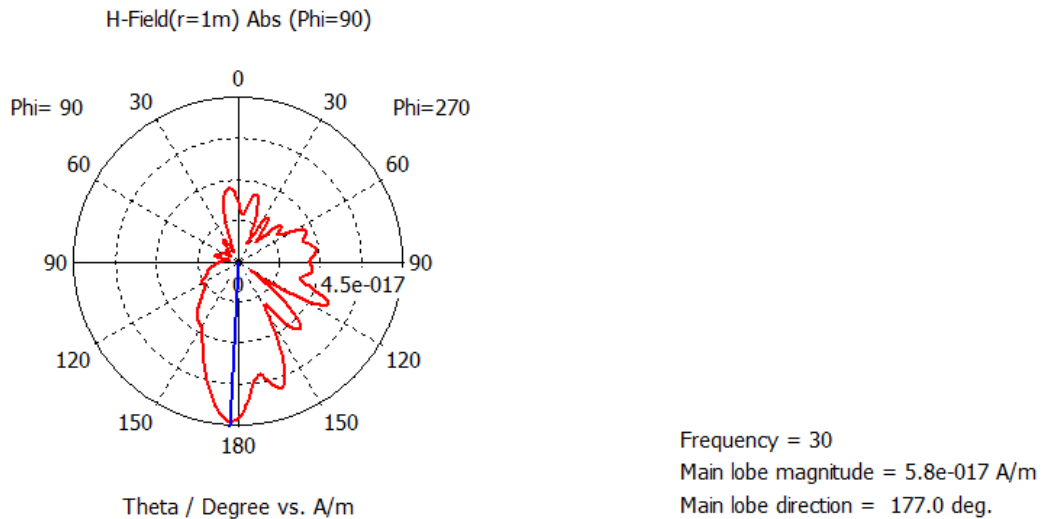
Figure 5.23: H-field radiation pattern of antenna

5.6 Oil Recovery by Using Nanofluids in a Water Flooding System

In this section the experimental results of the oil recovery by using zinc oxide and iron oxide nanofluids in different weight percentages are presented. A comparison of oil recovery between the nanofluids and with the presence of electromagnetic waves is given. The effects of electromagnetic waves and nanofluid on oil recovery were conducted by using a setup as shown in Figure 4.2. It should be noted that;

1. The simulated porous medium (glass bead packed column) was saturated by brine that was displaced by crude oil.

2. When only crude oil was produced at the outlet, the residual water volume was calculated.

3. Then crude oil was displaced by the nanofluids in the presence of electromagnetic waves.

4. For the purpose of comparison the same tests were conducted using nanofluids alone.

5.6.1 Oil Recovery Using Nanofluids without the Presence of Electromagnetic Waves

In this section the effect of three different concentrations 0.001, 0.05, 0.1 wt.% of zinc oxide (ZnO) and iron oxide (Fe_2O_3) nanofluids on oil recovery efficiency without applying electromagnetic waves will be discussed.

5.6.1.1 Zinc Oxide (ZnO) Nanofluid at 0.001 wt.%

Using ZnO nanofluid of 0.001wt.% the efficiency of oil recovery obtained was 48.87 % ROIP as shown in Figure 5.24. The characteristics of glass bead packed column and amount of original oil in place (OOIP) and residual oil in place are shown in Table.5.5. Due to the hydrophilic nature of ZnO nanoparticles, these particles can adsorb on the surface of glass beads. In enhanced oil recovery process, a change in wettability can affect the relative permeability for brine, which affects oil recovery efficiency due to a change in wettability from oilwet to partially water wet surface. ZnO can change the wettability; in this process, oxygen vacancies at the surface of ZnO nanoparticles are occupied by water molecule. This result in generation of OH groups, which makes the surface hydrophilic. The wettability of the surface is controlled by the equilibrium of oxygen vacancy on the ZnO and hydroxyl group. Due to oxygen vacancy at reservoir conditions, the equilibrium between water and oxygen vacancy must be change to hydroxyl group and due to aliphatic chains in aqueous medium it must be same. Therefore, ZnO nanoparticles play the role of hydrophilic material in oil reservoir conditions. Due to the adsorption of ZnO nanoparticles on the rock surface, the system energy is decreased.

Figure 5.24: Oil recovery with respect to zinc oxide (ZnO) nanofluid injection without EM waves

Table 5.5: Characteristics of the glass bead packed column and oil recovery for 0.001 wt% zinc oxide (ZnO) nanofluid

	NF Without EM
Porosity (%)	24.00
Permeability (mD)	87214.47
Original oil in place (OOIP) (ml)	18.70
Residual oil in place(ROIP)(ml)	6.20
Volume recovered during water flooding (ml)	12.50
Recovery (ROIP)	48.87%

5.6.1.2 Zinc Oxide (ZnO) Nanofluid at 0.05 wt.%

Using ZnO nanofluid at 0.05wt.%, the oil recovery efficiency obtained was 44.03 % ROIP as shown in Figure 5.25. The characteristics of the glass bead packed column, amount of original oil in place (OOIP) and residual oil in place are shown in Table 5.6. Increasing the concentration of ZnO nanofluid from 0.001wt.% to 0.05wt.% decreased the posibility of fluid flow through the porous medium which affected the oil recovery efficiency. Due this, the permeability of the flow can be decreased which can also affect the efficiency of oil recovery. From the results, it is observed the oil recovery at nanofluid concentration of 0.05wt.% is less than that at 0.001wt.%. This decrease in oil recovery with increase in the nanofluid concentration can also be related to interfacial tension between the nanofluids and oil. As from the interfacial tension results, we observed that the interfacial tension at 0.05wt.% concentration of nanofluid is greater than at 0.001wt.%. Therefore, the oil recovery at nanofluid concentration of 0.05wt.% is less than that obtained at nanofluid concentration of 0.001wt.%.

Figure 5.25: Oil recovery with respect to zinc oxide (ZnO) nanofluid injection without EM waves

Table 5.6: Characteristics of the glass bead packed column and oil recovery for
0.05 wt% zinc oxide (ZnO) nanofluid

	NF Without EM
Porosity (%)	23.94
Permeability (mD)	85830.12
OOIP	18.80
ROIP	6.20
Vol recovered during WF	12.60
Recovery (ROIP)	44.03%

5.6.1.3 Zinc Oxide (ZnO) Nanofluid at 0.1 wt.%

Using ZnO nanofluid at 0.1wt.%, the oil recovery efficiency obtained was 39.19 %
ROIP as shown in Figure 5.26. The characteristics of the glass bead packed column,
amount of original oil in place (OOIP) and residual oil in place is shown in Table 5.7.
Increasing the concentration of ZnO nanofluid from 0.001wt.% to 0.1wt.% decreased
the posibility of fluid flow through the porous medium which affected the oil recovery
efficiency. From the results, it is observed that the oil recovery at nanofluid
concentration of 0.1wt.%   is less than at 0.001wt.%. This decrease in oil recovery with
increase in the nanofluid concentration can also be related to interfacial tension between
the nanofluids and oil. From the interfacial tension results, we observed that the
interfacial tension at 0.1wt.% concentration of nanofluid is greater than at 0.001wt.%.
Therefore, the oil recovery at nanofluid concentration of 0.1wt.% is less than at the
nanofluid concentration of 0.001wt.%.

Figure 5.26: Oil recovery with respect to zinc oxide (ZnO) nanofluid injection without EM waves

Table 5.7: Characteristics of the glass bead packed column and oil recovery for 0.1 wt% zinc oxide (ZnO) nanofluid

	NF Without EM
Porosity (%)	22.74
Permeability (mD)	83189.19
Original oil in place (OOIP) (ml)	18.10
Residual oil in place(ROIP)(ml)	6.20
Volume recovered during water flooding (ml)	11.90
Recovery (ROIP)	39.19%

5.6.1.4 Effect of ZnO Nanofluid Concentration On Fluid Mobility and Recovery
    Efficiency

 The fluid mobility is affected by the injection of nanofluids in different concentration. In this section, the effect of three different concentrations 0.001, 0.05, and 0.1 wt.% of ZnO nanofluid on fluid mobility will be discussed. From Figure 5.27, it is observed that pressure increases with increase in concentration of the nanofluids.
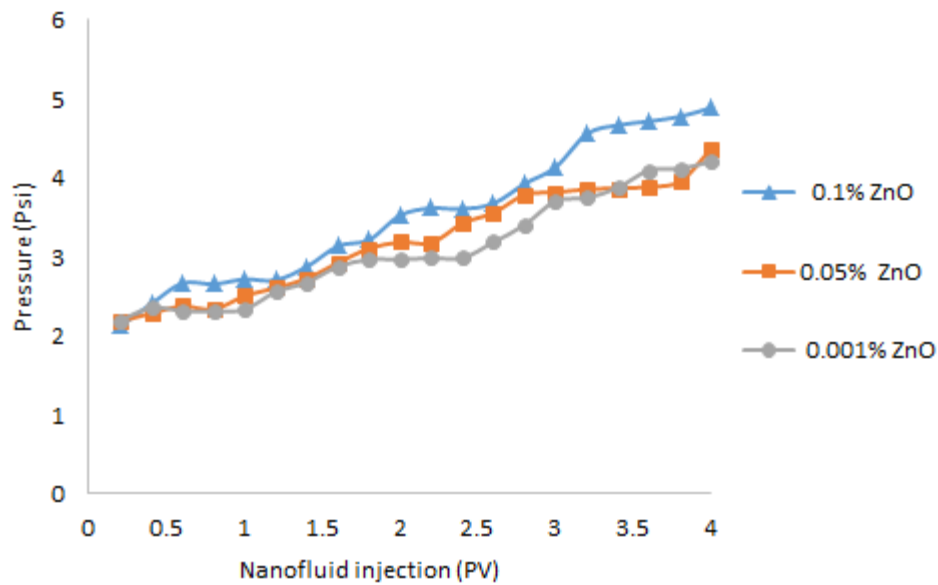
Figure 5.27: Pressure versus pore volume of ZnO nanofluid injected in different concentration

Fluid mobility can be calculated by Mobility Reduction Factor (MRF),

$$MRF = \frac{\Delta P_1}{\Delta P_2} \qquad (5.6)$$

Where; ΔP_1 is the pressure difference after water flooding stage. ΔP_2 is the pressure difference before nanofluid injection (EOR stage). Mobility Reduction Factor (MRF) value greater than '1' shows that the nanofluid causes blogging to the pores and channels.

Table 5.8: Value of mobility reduction factor for different concentration of ZnO nanofluid

	0.001 wt.%	0.05wt.%	0.1wt.%
Mobility reduction factor (MRF)	1.91	1.99	2.29

From the Table 5.8, it can be seen that with increasing concentration of nanofluids, the mobility reduction factor is also increasing. This increase in the mobility reduction factor affected the permeability of porous medium such as glass bead packed column during nanofluid injection. Increasing the concentration of ZnO nanofluids reduced the chances of fluid flow through the porous medium which affected the oil recovery efficiency. This difficulty of fluid flow indicates that the permeability of the porous medium is reduced.

Due to the hydrophilic nature of ZnO nanoparticles, these particles can adsorb on the surface of the glass beads. Therefore by increasing the concentration of ZnO nanoparticles, the chances of more adsorption of ZnO nanoparticles increase. Due to the high adsorption of ZnO nanoparticles, fluid flow through the porous medium becomes difficult. The electro statistic charges on the surface of ZnO nanoparticles becomes neutralized at high concentration of ZnO nanofluid resulting in accumulation of nanoparticles in the medium, which blogs the channels and pore throats. Therefore the recovery efficiency at the highest concentration of 0.1wt.% is low as compared to the recovery at the lowest concentration of 0.001% which produced high recovery efficiency.

5.6.1.5 Iron Oxide (Fe_2O_3) Nanofluid at 0.001 wt.%

Using iron oxide (Fe_2O_3) nanofluid at 0.001wt.%, the oil recovery efficiency obtained was 48.87 % ROIP as shown in Figure 5.28. The characteristics of the glass bead packed column, amount of original oil in place (OOIP) and residual oil in place is shown in Table 5.9. Due to the hydrophilic nature of iron oxide nanoparticles, these particles can adsorb on the surface of the glass beads. Iron oxide can change the wettability; in this process, oxygen vacancies at the surface of iron oxide nanoparticles are occupied by water molecule. This results in the generation of OH groups, which makes the

surface hydrophilic. The wettability of the surface is controlled by the equilibrium of oxygen vacancy on the iron oxide and the hydroxyl group.
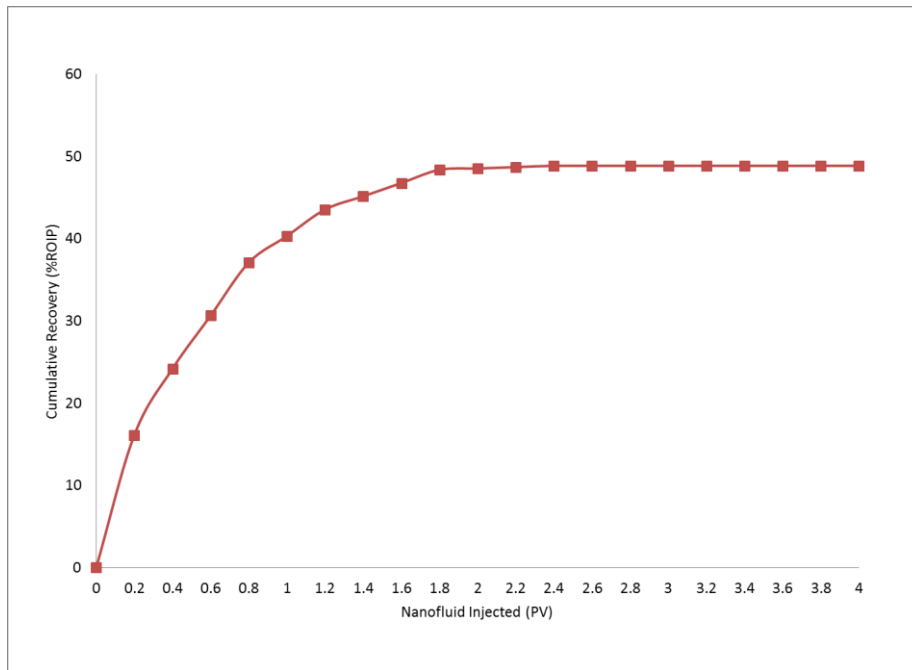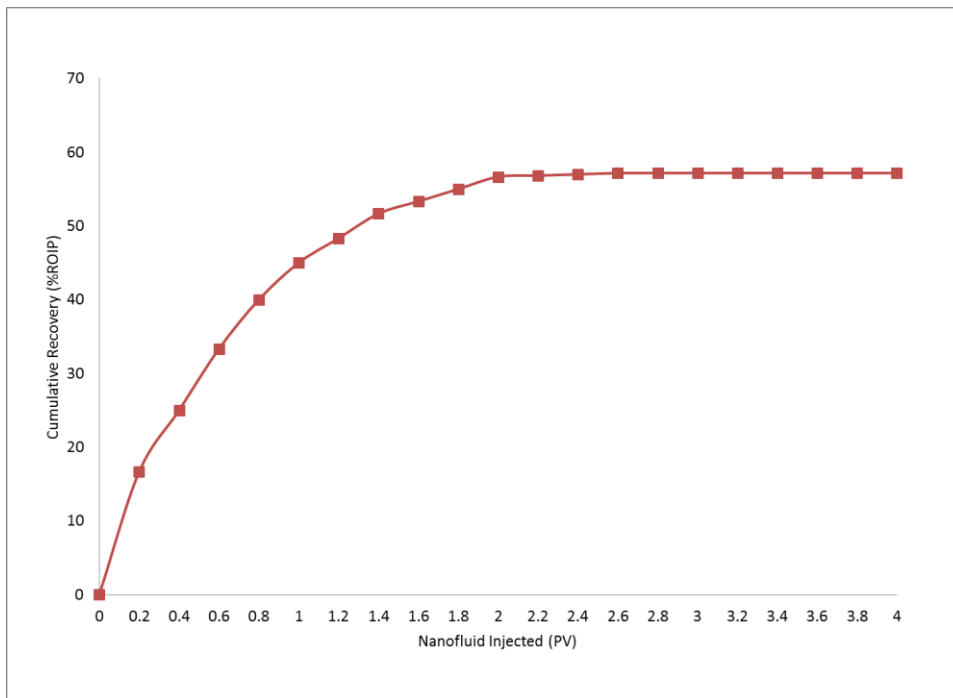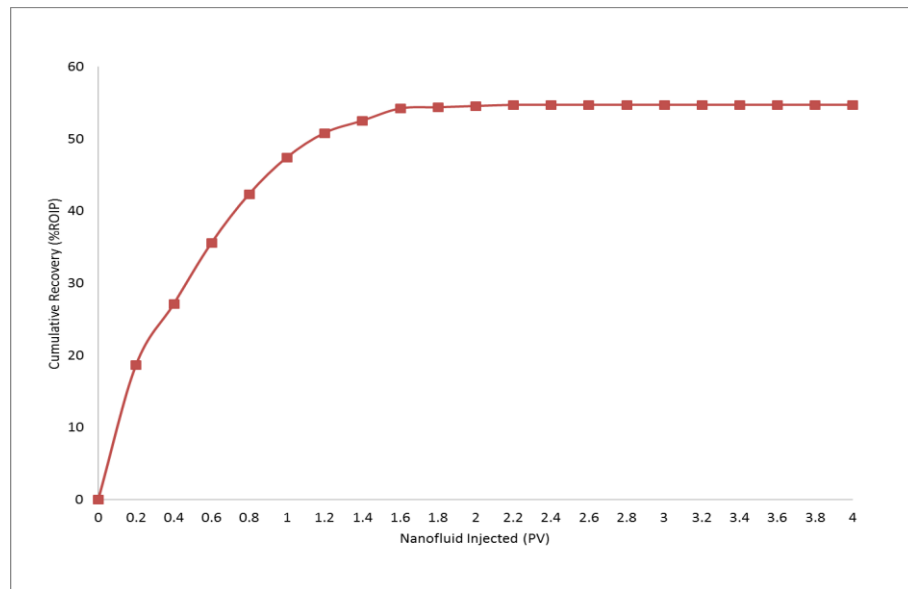

Figure 5.28: Oil recovery with respect to iron oxide (Fe_2O_3) nanofluid injection without EM waves

Table 5.9: Characteristics of the glass bead packed column and oil recovery for 0.001 wt% iron oxide (Fe_2O_3) nanofluid

	NF without EM
Porosity (%)	24.31
Permeability (mD)	84489.02
Original oil in place (OOIP) (ml)	18.70
Residual oil in place(ROIP)(ml)	5.90
Volume recovered during water flooding (ml)	12.80
Recovery (ROIP)	54.74%

5.6.1.6 Iron Oxide (Fe₂O₃) Nanofluid at 0.05 wt.%

Using iron oxide (Fe_2O_3) nanofluid at 0.05wt.%, the oil recovery efficiency obtained was 47.86 % ROIP as shown in Figure 5.29. The characteristics of the glass bead packed column, amount of original oil in place (OOIP) and residual oil in place are shown in Table 5.10. Increasing the concentration of iron nanofluid from 0.001wt.% to 0.05wt.% decreased the posibility of fluid flow through the porous medium which affected the oil recovery efficiency. From the interfacial tension results, we observed that interfacial tension at 0.05wt.% concentration of nanofluid is greater than at the nanofluid concentration of 0.001wt.%. Therefore, the oil recovery at nanofluid concentration of 0.05wt.% is less than at nanofluid concentration of 0.001wt.%.
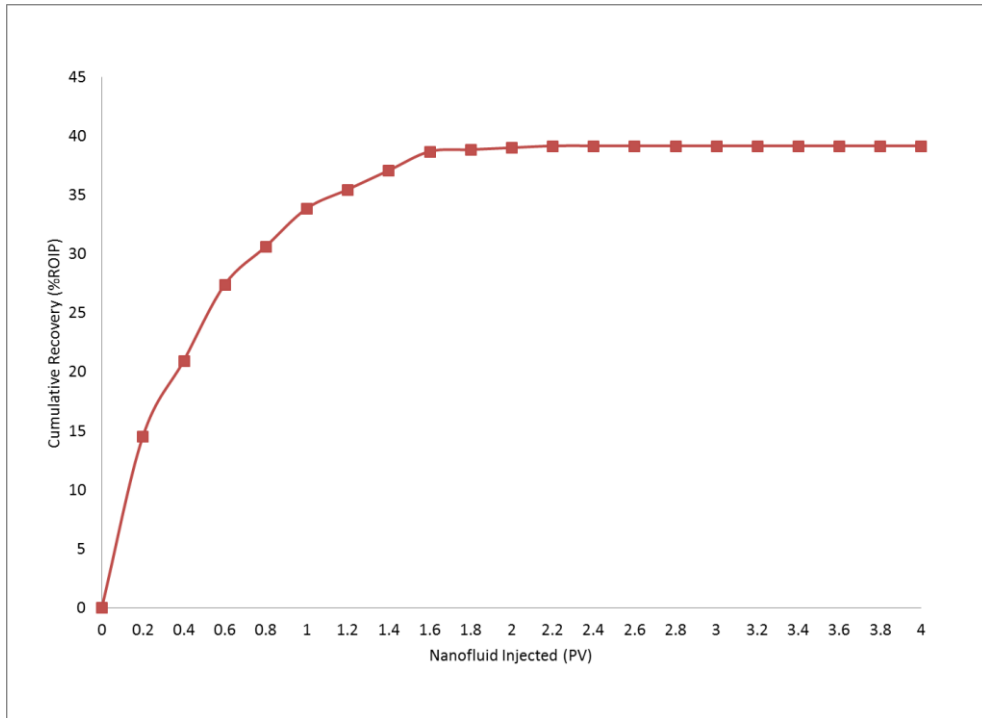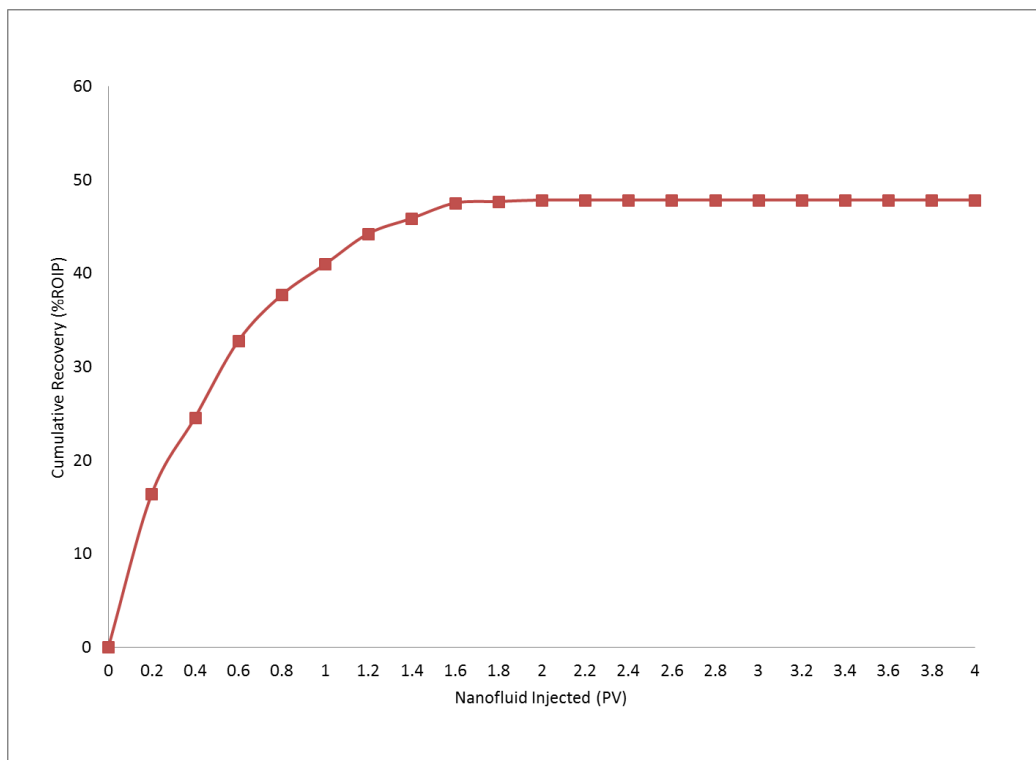

Figure 5.29: Oil recovery with respect to iron oxide (Fe₂O₃) nanofluid injection without EM waves

Table 5.10: Characteristics of the glass bead packed column and oil recovery for 0.05 wt% iron oxide (Fe_2O_3) nanofluid

	NF without EM
Porosity (%)	24.31
Permeability (mD)	84489.02
Original oil in place (OOIP) (ml)	18.8
Residual oil in place(ROIP)(ml)	6.1
Volume recovered during water flooding (ml)	12.7
Recovery (ROIP)	47.86%

5.6.1.7 Iron Oxide (Fe_2O_3) Nanofluid at 0.1 wt.%

Using iron oxide (Fe_2O_3) nanofluid at 0.1wt.%, the oil recovery efficiency obtained was 43.44 % ROIP as shown in Figure 5.30. The characteristics of the glass bead packed column, amount of original oil in place (OOIP) and residual oil in placeare shown in Table 5.11. Increasing the concentration of iron oxide nanofluid from 0.001wt.% to 0.1wt.% decreased the posibility of fluid flow through the porous medium which affected the oil recovery efficiency. From the interfacial tension results, we observed that the interfacial tension at 0.1wt.% concentration of nanofluid is greater than at nanofluid concentration of 0.001wt.%. Therefore, oil recovery at nanofluid concentration of 0.1wt.% is less than at nanofluid concentration of 0.001wt.%.

Figure 5.30: Oil recovery with respect to iron oxide (Fe_2O_3) nanofluid injection without EM waves

Table 5.11: Characteristics of the glass bead packed column and oil recovery for 0.1 wt% iron oxide (Fe_2O_3) nanofluid

	NF without EM
Porosity (%)	24.48
Permeability (mD)	84489.02
Original oil in place (OOIP) (ml)	18.70
Residual oil in place (ROIP)(ml)	5.80
Volume recovered during water flooding (ml)	12.90
Recovery (ROIP)	43.44%

5.6.1.8 Effect of Iron Oxide (Fe$_2$O$_3$) Nanofluid Concentration on Fluid Mobility and Recovery Efficiency

The fluid mobility is affected by the injection of nanofluids at different concentration. In this section, the effect of three different concentrations 0.001, 0.05, 0.1 wt.% of iron oxide nanofluid on fluid mobility will be discussed. From the Figure 5.31, it is observed that pressure increases with increase in concentration of the nanofluids.
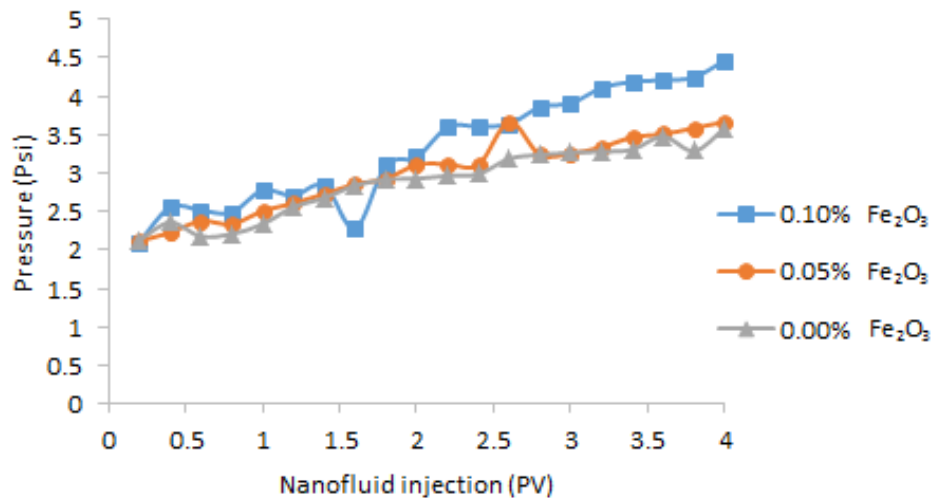
Figure 5.31: Pressure versus pore volume of iron oxide nanofluid injected in different concentration

Table 5.12: Value of mobility reduction factor for different concentration of iron oxide nanofluid

	0.001 wt.%	0.05wt.%	0.1wt.%
Mobility reduction factor (MRF)	1.68	1.73	2.12

From the Table 5.12, it can be seen that by increasing the concentration of the iron oxide nanofluids the mobility reduction factor is also increasing. This increase in the mobility reduction factor affected the permeability of porous medium such as the glass bead packed column during nanofluid injection. Increasing the concentration of iron oxide nanofluids reduced the chances of fluid flow through the porous medium which affected the oil recovery efficiency. This difficulty of fluid flow indicates that permeability of the porous medium is reduced.

113

Due to the hydrophilic nature of iron oxide nanoparticles, these particles can adsorb on the surface of the glass beads. Therefore, by increasing the concentration of iron oxide nanoparticles, the chances of more adsorption of iron oxide nanoparticles increase. Due the high adsorption of iron oxide nanoparticles, fluid flow through the porous medium becomes difficult which blogs the channels and pore throats. Therefore the recovery efficiency at the highest concentration of 0.1% is low as compared to the lowest concentration of 0.001%, which produced high recovery efficiency.

5.6.2 Oil Recovery Using Nanofluids in the Presence of Electromagnetic Waves

In this section, the effect of three different concentrations 0.001, 0.05, 0.1 wt.% of Zinc oxide (ZnO) and iron oxide (Fe_2O_3) nanofluids on oil recovery efficiency in the presence of electromagnetic waves will be discussed.

5.6.2.1 Zinc Oxide (ZnO) Nanofluid at 0.001 wt.%

Zinc oxide (ZnO) nanofluid at 0.001 wt.% in the presence of electromagnetic waves produced oil recovery of 64.26% as shown in Figure 5.32. The test result of using zinc oxide (ZnO) nanofluid at 0.001 wt.% are shown on Table 5.13. It is evident that the production rate of oil displaced by the nanofluid in the presence of electromagnetic waves was increased by 15.39% in comparison to using the nanofluid only.

The effective moment is expressed by the following equation,

$$p_{eff} = 4\pi\varepsilon_f K a^3 E_o \tag{5.7}$$

Where, $K = \dfrac{\varepsilon_p - \varepsilon_f}{\varepsilon_p + 2\varepsilon_f}$ is the Clausius-Mossotti function, 'a' is the radius of the particle.

The equation for instantaneous force applied on a dipole by a time-dependent electric field is given below,

114

$$\vec{F}_{dep}(t) = \vec{p}_{eff} \cdot \nabla \vec{E}(t)$$

<div align="right">(5.8)</div>

$\vec{F}_{dep}$ is called dielectrophoretic (DEP) force which is applied on a polarizable particle when it is exposed to a non-uniform electric field. When nanoparticles are either adsorbed by the oil/water boundary or spread in fluid phase in reservoir rock pores, and exposed to external electromagnetic field, the resulting particle movements displace the interface.This equation shows that particles will displaced the oil water interface if the particles are attached to the oil water interface due to force experienced by the nanoparticles. This dielectrophoretic force depends on the particle size which shows that by increasing the particle size the dielectrophoretic force experienced by the nanoparticles will also increase. These particles with large particle size experience large magnetic force when they were exposed to the electromagnetic waves. The dielectrophoretic force experienced by zinc oxide (ZnO) nanoparticles produced interfacial movement which improved the oil recovery. The oil/water interfacial tension can show the elastic response to electromagnetic field oscillation. From the band structure of zinc oxide (ZnO), the band gap value obtained is 0.808ev as shown in Figure 5.3. The number of electron of zinc oxide (ZnO) which took part to produce the band structures are 36. The band gap is also related to dielectric constant, where the dielectric constant increases with decreasing band gap [135, 136]. As zinc oxide (ZnO) has the highst band gap, it has low dielectric constant. This shows that zinc oxide (ZnO) nanofluid in the presence of electromagnetic waves has low polarization due to high band gap value. The apparent viscosity of nanofluid increases due to the polarization of ZnO nanoparticles which also increases the capillary number due to reduction of the capillary forces. Therefore oil displacement efficiency increases and it produced oil recovery of 64.26%
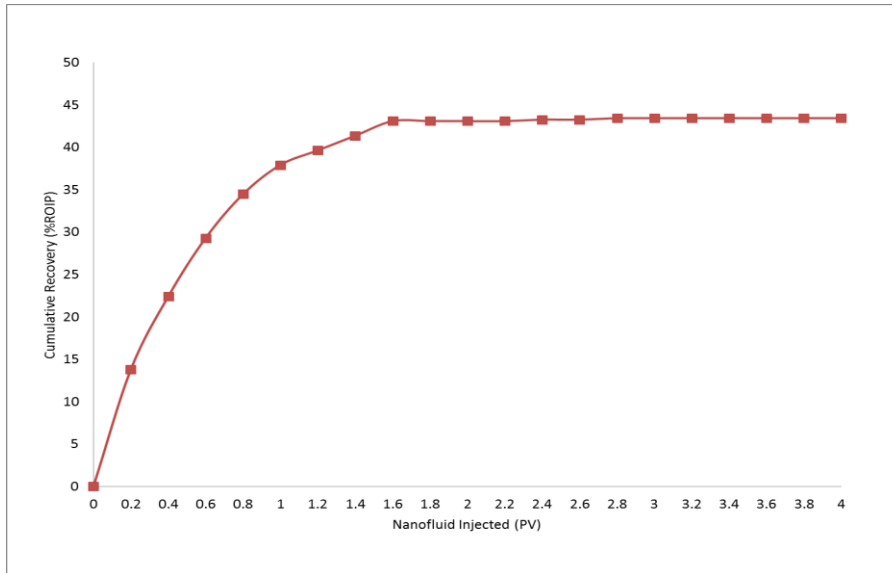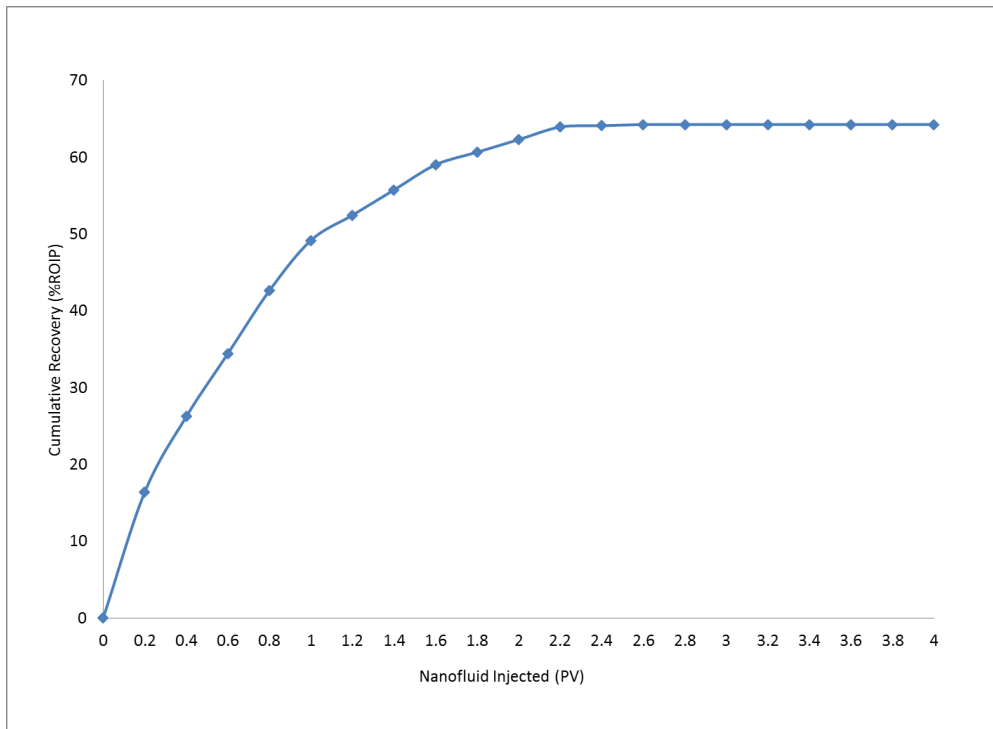
Figure 5.32: Oil recovery with respect to zinc oxide (ZnO) nanofluid injection with EM waves

Table 5.13: Characteristics of the glass bead packed column and oil recovery for zinc oxide (ZnO) nanofluid at 0.001 wt%

	NF With EM
Porosity (%)	24.22
Permeability (mD)	85830.12
Original oil in place (OOIP) (ml)	18.60
Residual oil in place(ROIP)(ml)	6.10
Volume recovered during water flooding (ml)	12.50
Recovery (ROIP)	64.26%

5.6.2.2 Zinc Oxide (ZnO) Nanofluid at 0.05 wt.%

Zinc oxide (ZnO) nanofluid at 0.05 wt.% in the presence of electromagnetic waves produced oil recovery of 57.16% as shown in Figure 5.33. The test result of using zinc oxide (ZnO) nanofluid at 0.05 wt.% are shown on Table 5.14. Taking into account that the interfacial tension of zinc oxide (ZnO) nanoparticles had increased with increasing concentration of the nanoparticles. The zinc oxide (ZnO) nanofluid at concentration of 0.001% has low interfacial tension as compared to the iron oxide (Fe_2O_3) nanofluid at concentration of 0.05%. Therefore, the nanofluid at 0.001% concentration showed high oil recovery as compared to the nanofluid at 0.05% concentration.
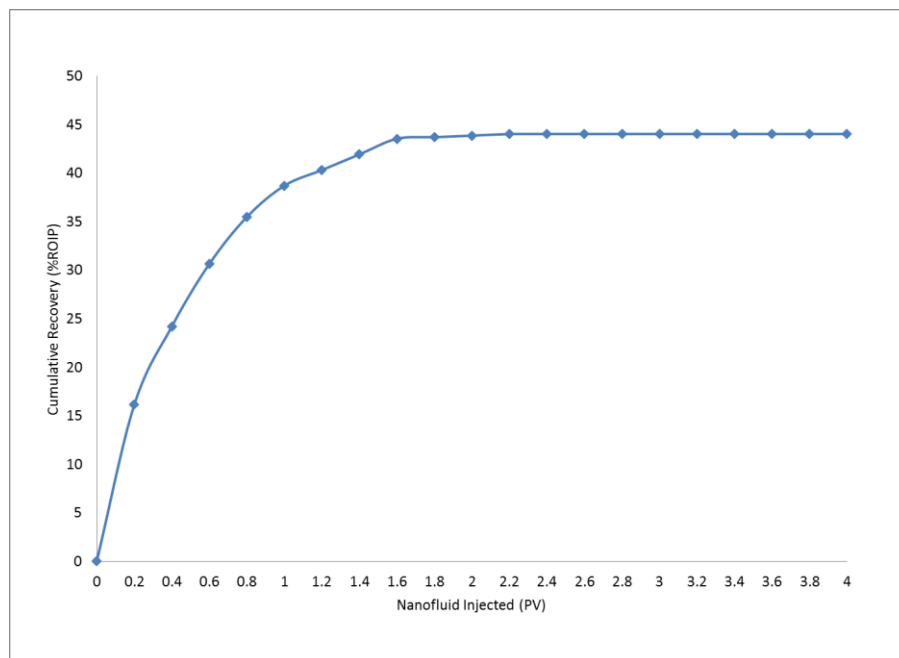
Figure 5.33: Oil recovery with respect to zinc oxide (ZnO) nanofluid injection with EM waves

117

Table 5.14: Characteristics of the glass bead packed column and oil recovery for zinc oxide (ZnO) nanofluid at 0.05 wt%

	NF With EM
Porosity (%)	24.58
Permeability (mD)	83189.19
Original oil in place (OOIP) (ml)	18.70
Residual oil in place(ROIP)(ml)	6
Volume recovered during water flooding (ml)	12.70
Recovery (ROIP)	57.16%

5.6.2.3 Zinc Oxide (ZnO) Nanofluid at 0.1 wt.%

Zinc oxide (ZnO) nanofluid at 0.1wt.% in the presence of electromagnetic waves produced oil recovery of 49.53% and with nanofluid only the oil recovery is 39.19% as shown in Table 5.15. As shown in Figure 5.34, the production rate of oil displaced by the nanofluid in the presence of electromagnetic increased by 10.34% in comparison with nanofluid only. The interfacial tension of zinc oxide (ZnO) nanoparticles was observed to increase with increasing concentration of nanoparticles. This was observed as the zinc oxide (ZnO) nanofluid at the concentration of 0.1wt.% recorded high interfacial tension as compared to the zinc oxide (ZnO) nanofluid at concentrations of 0.001wt.% and 0.05wt.%. Therefore, the nanofluid at 0.1wt.% concentration showed the lowest oil recovery as compared to the nanofluid at 0.001wt.% and 0.05wt.% concentration.

Figure 5.34: Oil recovery with respect to zinc oxide (ZnO) nanofluid injection with EM waves

Table 5.15: Characteristics of the glass bead packed column and oil recovery for zinc oxide (ZnO) nanofluid at 0.1 wt%

	NF With EM
Porosity (%)	23.87
Permeability (mD)	81928
Original oil in place (OOIP) (ml)	18.90
Residual oil in place(ROIP)(ml)	6.40
Volume recovered during water flooding (ml)	12.50
Recovery (ROIP)	49.53%

5.6.2.4 Effect of ZnO Nanofluid Concentration On Fluid Mobility and Recovery Efficiency

For ZnO nanofluid, the highest recovery efficiency of 64.26% ROIP with the application of electromagnetic waves and 48.87% ROIP without electromagnetic waves application was obtained from the lowest concentration of ZnO nanoparticles in the fluid (0.001 wt.%). At the concentrationof 0.05wt.%, the effieciency obtained was 57.16% ROIP with electromagnetic waves and 44.03% ROIP without electromagnetic waves. At 0.1wt.% of nanofluid concentration, the effiency of recovery obtained was 49.53% ROIP with electromagnetic waves and 39.19% ROIP without electromagnetic waves. The oil recovery efficiency of ZnO nanofluid with electromagnetic waves is higher than the oil recovery without electromagnetic waves. The pressure increased with electromagnetic waves as compared to without electromagnetic waves during nanofluid injection as shown in Figure 5.35.
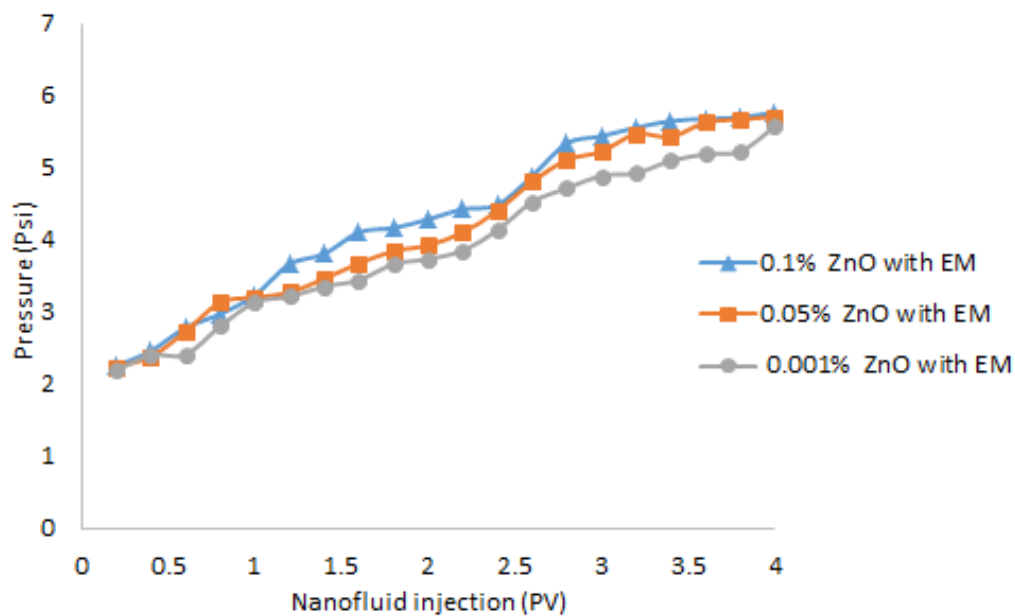
Figure 5.35: Pressure versus pore volume of ZnO nanofluid injected in different concentration with EM

From the Darcy's equation (5.9)

$$\mu = \frac{KA}{Lq}\Delta P \qquad (5.9)$$

It is observed that the increase in pressure is related to the increase in apparent viscosity of the fluid.

The apparent viscosity increases due to the polarization of ZnO nanoparticles; in the presence of the electromagnetic waves the nanoparticles align themselves in the direction of the electromagnetic field. This polarization produces momentarily chain like structure which increases the resistance of the fluid flow resulting in increasing the viscosity of the fluid; therefore pressure also increases. This increase in viscosity increases the capillary number which reduces the capillary forces.

5.6.2.5 Iron Oxide (Fe$_2$O$_3$) Nanofluid at 0.001 wt.%

Iron oxide (Fe$_2$O$_3$) nanofluid at 0.001 wt% in the presence of electromagnetic waves produce oil recovery of 71.66 % as shown in Figure 5.36. The test results for iron oxide (Fe$_2$O$_3$) nanofluid at 0.001 wt% are shown on Table 5.16. It is evident that the production rate of oil displaced by the nanofluid with electromagnetic was increased by 16.92% in comparison to using nanofluid only. When magnetic nanoparticles are spread in fluid phase or adsorbed at the oil/water interface in reservoir rock pores, and exposed to external magnetic field, the subsequent particle movements displaces the interface.

$$F_m = \mu_o V_p (M_p \cdot \nabla) H$$

$$F_m = V_p (M_p \cdot \nabla) B \qquad (5.10)$$

This equation shows that the nanofluid particles will be displaced from the oil water interface if the particles are attached to the oil water interface due to force experienced by the magnetic nanoparticles. This magnetic force depends on the particle size which shows that as the particle size increases, the magnetic force experienced by the nanoparticles will also be increased. These particles with large particle size experience

large magnetic force when these particles were exposed to electromagnetic waves. Due to the magnetic force experienced by iron oxide (Fe_2O_3), the nanoparticles produced interfacial movement which improved the oil recovery. From the band structure of iron oxide (Fe_2O_3), the band gap value obtained is 0.201ev as shown in Figure 5.5. The number of electron of iron oxide (Fe_2O_3) which took part to produce the band structures are 68. The lowest band gap value of iron oxide (Fe_2O_3) shows that iron oxide requires smaller electromagnetic energy to shift its valence electrons to conduction band. The band gap is also related to dielectric constant, where the dielectric constant increases with decreasing band gap [135, 136]. As iron oxide has the lowest band gap, it has high dielectric constant. This shows that iron oxide (Fe_2O_3) nanofluid in the presence of electromagnetic waves has high polarization due to low band gap. This high polarization effect the apparent viscosity of nanofluid which increase the oil displacement efficiency and it produced oil recovery of 71.66%
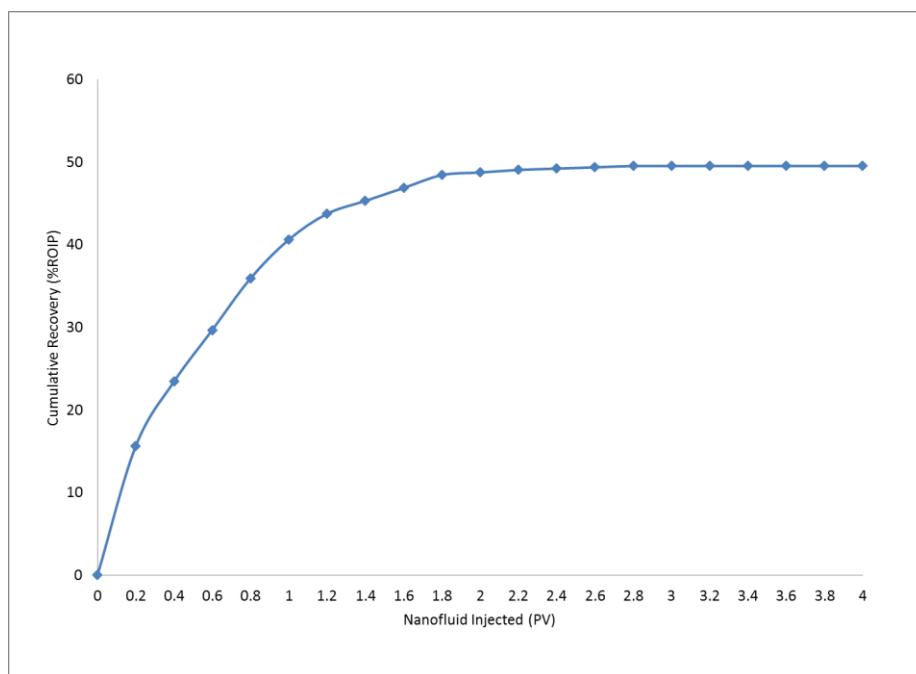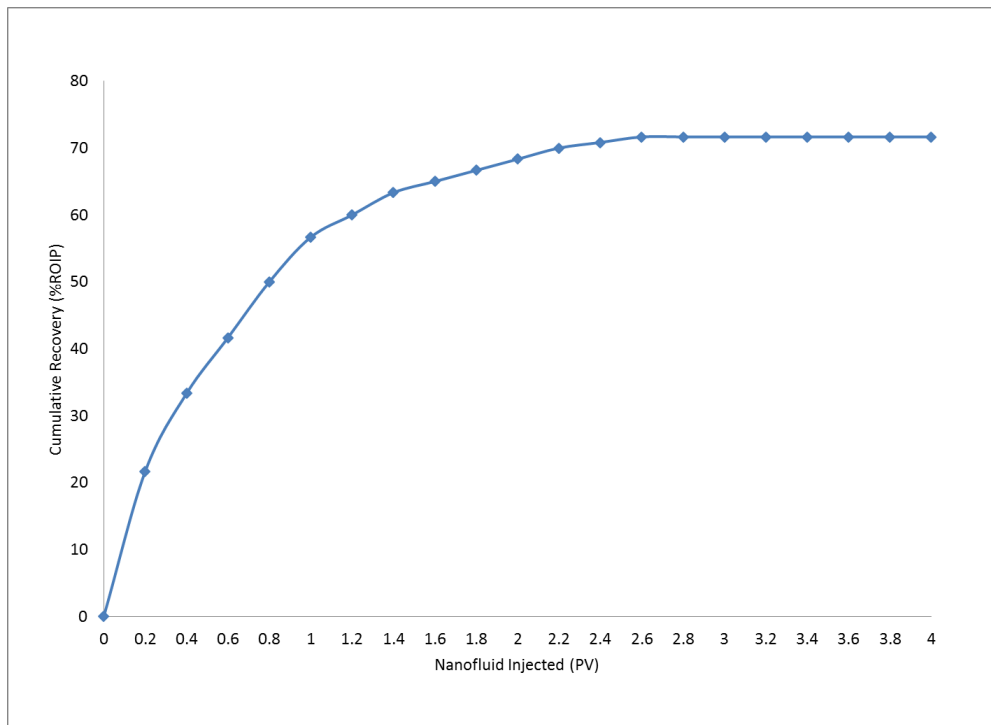

Figure 5.36: Oil recovery with respect to iron oxide (Fe_2O_3) nanofluid injection with EM waves

Table 5.16: Characteristics of the glass bead packed column and oil recovery for iron oxide (Fe_2O_3) nanofluid at 0.001 wt%

	NF with EM
Porosity (%)	24.03
Permeability (mD)	83189.19
Original oil in place (OOIP) (ml)	18.60
Residual oil in place(ROIP)(ml)	6
Volume recovered during water flooding (ml)	12.60
Recovery (ROIP)	71.66%

5.6.2.6 Iron Oxide (Fe$_2$O$_3$) Nanofluid at 0.05 wt.%

Iron oxide (Fe_2O_3) nanofluid at 0.05 wt.% in the presence of electromagnetic waves produced oil recovery of 65.25 % as shown in Figure 5.37. The iron oxide (Fe_2O_3) nanofluid test results are shown on Table 5.17. The interfacial tension of iron oxide (Fe_2O_3) nanoparticles increases with increasing concentration of nanoparticles. The iron oxide (Fe_2O_3) nanofluid at the concentration of 0.001% has low interfacial tension as compared to the iron oxide (Fe_2O_3) nanofluid at the concentration of 0.05%. Therefore, the nanofluid at 0.001wt.% concentration showed high oil recovery as compared to the nanofluid at 0.05wt.% concentration as shown in Figure 5.37. It is evident that the reduction of interfacial tension at the nanofluid–oil interface and enhancement of pore wettability produced an energy decline of oil in linking with the porous medium surface due to which the oil flow rate increased.
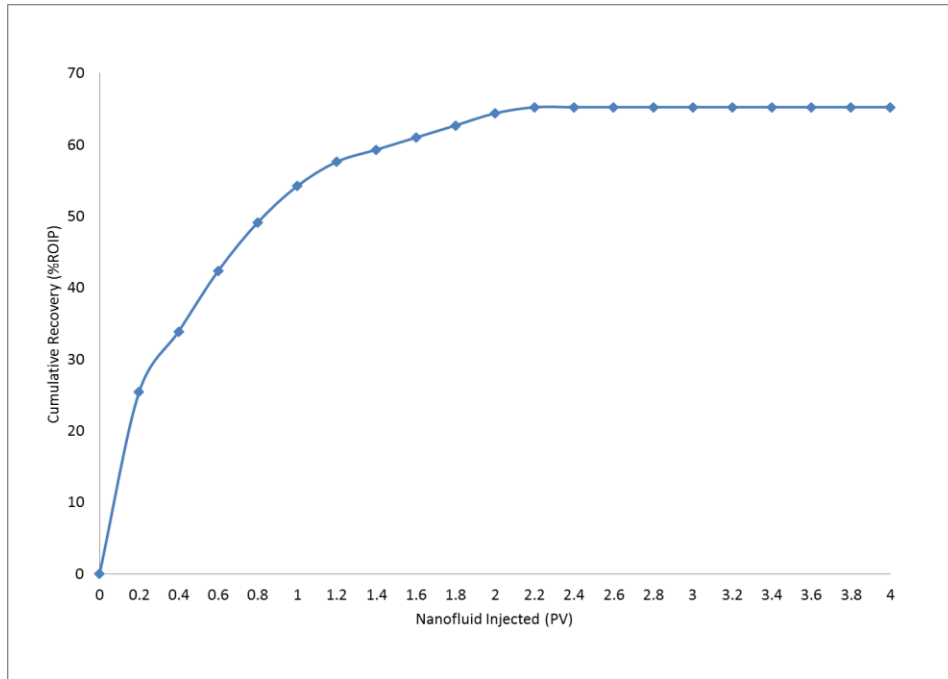
Figure 5.37: Oil recovery with respect to iron oxide (Fe$_2$O$_3$) nanofluid injection with EM waves

Table 5.17: Characteristics of the glass bead packed column and oil recovery for iron oxide (Fe$_2$O$_3$) nanofluid at 0.05 wt%

	NF with EM
Porosity (%)	24.37
Permeability (mD)	85830.12
OOIP (ml)	18.7
ROIP	5.9
Vol recovered during WF	12.8
Recovery (ROIP)	65.25

5.6.2.7 Iron Oxide (Fe₂O₃) Nanofluid at 0.1 wt.%

Iron oxide (Fe₂O₃) nanofluid at 0.1 wt.% in the presence of electromagnetic waves produced oil recovery of 55.24%. The iron oxide (Fe₂O₃) nanofluid test result is shown in Figure 5.38 and in Table 5.18. The interfacial tension of iron oxide (Fe₂O₃) nanoparticles increases with increasing concentration of nanoparticles. The iron oxide (Fe₂O₃) nanofluid at the concentration of 0.1wt.% has high interfacial tension as compared to the iron oxide (Fe₂O₃) nanofluid at concentrations of 0.001wt.% and 0.05wt.%. Therefore, the nanofluid at 0.1wt.% concentration showed low oil recovery as compared to the nanofluid at 0.001wt.% and 0.05wt.% concentration.
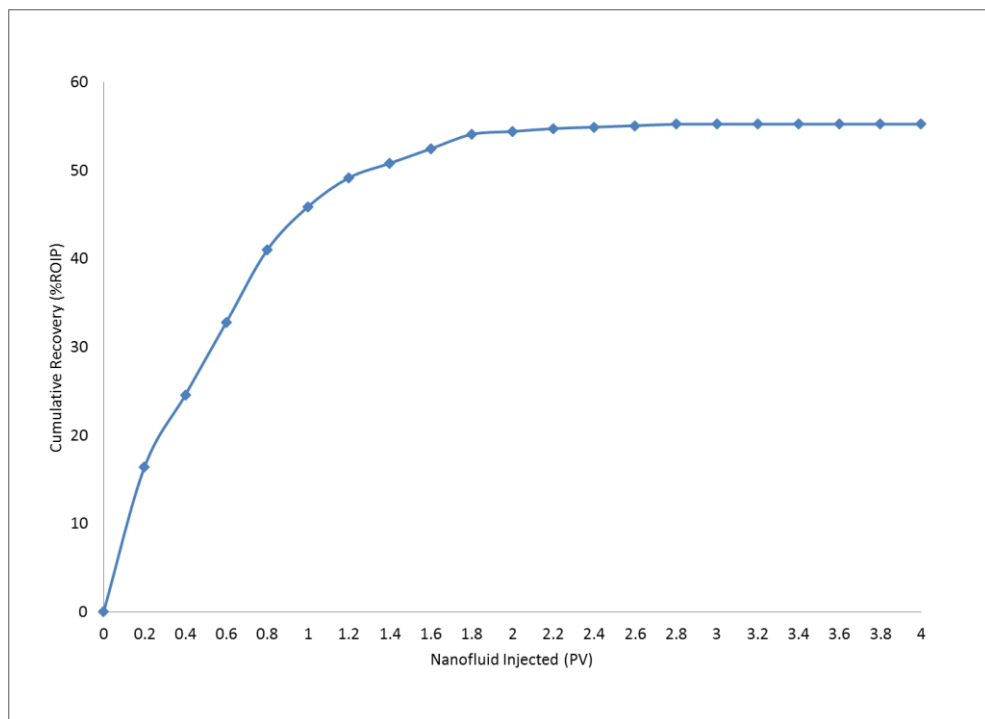
Figure 5.38: Oil recovery with respect to iron oxide (Fe₂O₃) nanofluid injection without EM waves

Table 5.18: Characteristics of the glass bead packed column and oil recovery for iron oxide (Fe_2O_3) nanofluid at 0.1 wt%

	NF with EM
Porosity (%)	24.41
Permeability (mD)	83189.19
Original oil in place (OOIP) (ml)	18.90
Residual oil in place (ROIP)(ml)	6.10
Volume recovered during water flooding (ml)	12.80
Recovery (ROIP)	55.24%

5.6.2.8 Effect of Iron Oxide (Fe$_2$O$_3$) Nanofluid Concentration on Fluid Mobility and Recovery Efficiency

The highest recovery efficiency of 71.66% ROIP with electromagnetic waves and 54.74% ROIP without electromagnetic waves was obtained from the lowest concentration of iron oxide nanoparticles in the fluid (0.001 wt.%). The concentration 0.05 wt.%. produced 65.25% ROIP with electromagnetic waves and 47.86% ROIP without electromagnetic waves. The nanofluid at 0.1wt.% concentration produced 55.24% ROIP with electromagnetic waves and 43.44% ROIP without electromagnetic waves. The oil recovery efficiency of iron nanofluid with electromagnetic waves is higher than the oil recovery without electromagnetic waves. The pressure increased with electromagnetic waves as compared to without electromagnetic waves during nanofluid injection as shown in Figure 5.39.

126
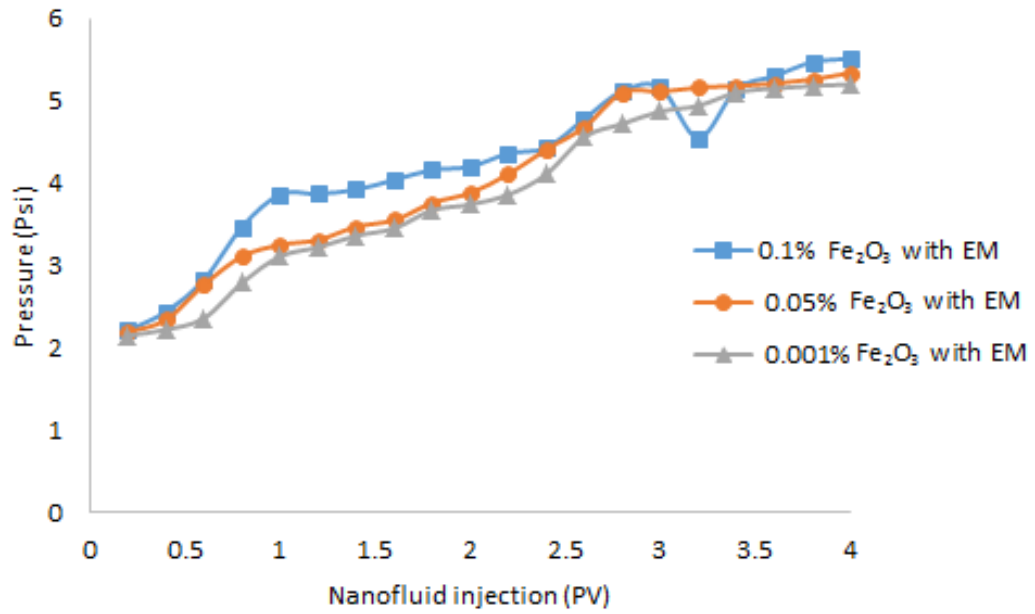
Figure 5.39: Pressure versus pore volume of iron oxide nanofluid injected in different concentration with EM

From the Darcy's equation (5.10)

$$\mu = \frac{KA}{Lq}\Delta P \qquad (5.10)$$

It is observed that the increase in pressure is related to the increase in apparent viscosity of the fluid.

The apparent viscosity increases due to the magnetic spin of the iron oxide nanoparticles; in the presence of electromagnetic waves the nanoparticles orient themselves in the direction of the electromagnetic field. This magnetic spin orientation produces momentarily chain like structure which increases the resistance of the fluid flow which results in increasing the viscosity of the fluid, therefore pressure is also increases. This increase in viscosity increases the capillary number but the capillary forces are reduced.

Table 5.19: Summary of the oil recovery with nanofluids and sample characteristics parameter

	zinc oxide (ZnO) nanofluid at 0.001 wt.%		zinc oxide (ZnO) nanofluid at 0.05 wt.%		zinc oxide nanofluid at 0.1 wt.%		iron oxide (Fe_2O_3) nanofluid at 0.001 wt.%		iron oxide (Fe_2O_3) nanofluid at 0.05 wt.%		iron oxide (Fe_2O_3) nanofluid at 0.1 wt.%	
	NF With EM	NF Without EM	NF With EM	NF Without EM	NF With EM	NF Without EM	NF With EM	NF Without EM	NF With EM	NF Without EM	NF With EM	NF Without EM
Porosity (%)	24.22	24.00	24.58	23.94	23.87	22.74	24.03	24.31	24.37	24.31	24.41	24.48
Permeability (mD)	85830.12	87214.47	83189.19	85830.12	81928	83189.19	83189.19	84489.02	85830.12	84489.02	83189.19	84489.02
OOIP(ml)	18.6	18.7	18.7	18.8	18.9	18.1	18.6	18.7	18.7	18.8	18.9	18.7
ROIP(ml)	6.1	6.2	6.0	6.2	6.4	6.2	6.0	5.9	5.9	6.1	6.1	5.8
Volume recovered during WF (ml)	12.5	12.5	12.7	12.6	12.5	11.9	12.6	12.8	12.8	12.7	12.8	12.9
Recovery (ROIP) %	64.26	48.87	57.16	44.03	49.53	39.19	71.66	54.74	65.25	47.86	55.24	43.44

Table 5.20: Summary of the density of state, band structure, hysteresis loss, and mobility reduction factor of nanofluids and ROIP

	Density of state (DOS)		Band structure	Particle size	Crystal plane	Mobility reduction factor (MRF)	ROIP	
							NF With EM	NF Without EM
ZnO	Zn = 3d104s2, O = 2s2p4,	number of electron = 36	0.808ev	30-39nm	[101]	1.91	64.26%	48.87%
Fe_2O_3	Fe = 3p6d64s2, O = 2s2p4,	number of electron = 68	0.201ev	30.27-37.60nm	[104]	1.68	71.66%	54.74%

5.7 Summary

The oil recovery by using iron oxide (Fe_2O_3) nanofluid at concentration of 0.001wt.% with EM was 71.66% of ROIP and without EM was 54.74% of ROIP. At 0.001% zinc oxide (ZnO) nanofluid, with EM the recovery of oil was 64.26 % of ROIP and without EM it was 48.87% of ROIP. These results imply that injecting iron oxide nanofluid of 0.001wt.% coupled with electromagnetic waves has potential for enhanced oil recovery. From the density of state, it is observed that the electronic configuration for zinc oxide (ZnO) is Zn = 3d104s2, O = 2s2p4 and the number of electron of zinc oxide (ZnO) which took part to produce the band structures are 36. The electronic configuration for iron oxide (Fe_2O_3) is Fe = 3p6d64s2, O = 2s2p4 and the number of electron of iron oxide (Fe_2O_3) which took part to produce the band structures are 68. This shows that the number of electrons in iron oxide is higher than in zinc oxide which activates at the valence band and conduction band. From the band structure of zinc oxide (ZnO), the band gap value obtained is 0.808ev and for iron oxide, the band gap value is 0.201ev. The percentage difference between the band gap of zinc oxide and iron oxide (Fe_2O_3) is 301%. For the zinc oxide (ZnO), the band structure Zn 4s states predominates the lowest conduction band and O 2p states are predominantly found in the uppermost valence band. For iron oxide (Fe_2O_3), it is observed that the valence band is a mixture of O 2p states and a majority of Fe 3d states orbitals, while the conduction band consists of small amount of Fe 3d states orbitals. The lowest band gap value of iron oxide (Fe_2O_3) shows that iron oxide requires smaller electromagnetic energy to shift its valence electrons to conduction band. In comparison, zinc oxide (ZnO) requires high electromagnetic energy for shifting its valence electrons to conduction band. The band gap is also related to dielectric constant, where the dielectric constant increases with decreasing band gap. As iron oxide has the lowest band gap, it has greater dielectric constant than zinc oxide (ZnO) which has the highest band gap and therefore the lowest dielectric constant. This shows that iron oxide (Fe_2O_3) nanofluid in the presence of electromagnetic waves has high polarization due to low band gap. Due to that, it produced high oil recovery of 71.66 % as compared to zinc oxide (ZnO) which has low polarization due to high band gap and consequently low oil recovery of 64.26%.

The XRD results of zinc oxide (ZnO) and iron oxide (Fe_2O_3) showed a single phase structure with a [101] and [104] major peak respectively. The particle size of zinc oxide (ZnO) and iron oxide (Fe_2O_3) nanoparticles are in the range of 30-39 nm and 30.27-37.60nm respectively. Iron oxide (Fe_2O_3) samples sintered at 500°C showed a high initial permeability, Q-factor and low loss factor as compared to samples sintered at 400°C. From the hysteresis loop, it was observed that iron oxide (Fe_2O_3) samples sintered at 500°C showed a 10.64% high magnetic saturation (Ms) as compared to the samples sintered at 400°C. In the new electromagnetic flooding system, it was observed that the magnetic field value at the top position (R_x-1) of the glass bead packed column is 74.37 % more than at the (R_x-2) center position of the column. While the magnetic field value at the top position (R_x-1) is 98 % more than at the bottom position (R_x-3) of the column. This shows that glass bead packed column saturated with oil, brine or nanofluids can absorb electromagnetic waves. From the simulation of radiation pattern of the antenna, it was observed that the E-field magnitude in the main lobe direction is 2.44×10^{-15} V/m and the H-field magnitude in the main lobe direction is 5.8×10^{-17} A/m.

Mobility reduction factor (MRF) value greater than '1' shows that the nanofluid cause cause blogging to the pores and channels. This increase in the mobility reduction factor affected the permeability of porous medium such as glass bead packed column during nanofluid injection. This difficulty of fluid flow indicates that the permeability of the porous medium is reduced. As the mobility reduction factor of zinc oxide (ZnO) is greater since the particle size of ZnO is larger than that of iron oxide (Fe_2O_3), therefore oil recovery due to zinc oxide (ZnO) is less than iron oxide (Fe_2O_3). In the presence of electromagnetic field, the apparent viscosity increases due to the polarization of nanoparticles which align themselves in the direction of the electromagnetic field. This increase in viscosity increases the capillary number which results in reduction of the capillary forces. As the capillary number increases, the oil displacement efficiency also increases. Therefore oil recovery with electromagnetic waves is higher than oil recovery without electromagnetic waves. These results imply that injecting the iron oxide nanofluid at the concentration of 0.001wt.% coupled with electromagnetic waves has potential for enhanced oil recovery. This is due to high strength of the magnetic force that acts on the nanoparticles which

is proportional to the magnetic field strength, and low band structure of iron oxide (Fe_2O_3) which produces high polarization as compared to zinc oxide (ZnO).

CHAPTER 6

CONCLUSION

A new water flooding system has been designed to study the recovery of oil. ZnO and Fe_2O_3 nanoparticles were synthesized and their properties were obtained in terms of density of state and band structure. These nanoparticles with good dielectric and magnetic properties can recover oil. From the simulation, it is observed that from the band structure of zinc oxide (ZnO), the band gap value obtained is 0.808ev and for iron oxide the band gap value is 0.201ev. The percentage difference between the band gap of zinc oxide and iron oxide is 301%.

From the nanoparticles characterization, the XRD results of zinc oxide (ZnO) and iron oxide (Fe_2O_3) prepared by sol gel method showed a single phase structure with a [101] and [104] major peak respectively. From the hysteresis loop, it is observed that iron oxide (Fe_2O_3) samples sintered at 500°C showed a 10.64% high magnetic saturation (Ms) compared to the sample sintered at 400°C.

In the new electromagnetic flooding system, it is observed that the magnetic field value at the top position (R_x-1) of the glass bead packed column is 74.37 % more than at the (R_x-2) center position of the column. . While the magnetic field value at the top position (R_x-1) is 98 % more than the bottom position (R_x-3) of the column.

Oil recovery through the usage of iron oxide (Fe_2O_3) nanofluid at 0.001wt.% and electromagnetic waves generated from the antenna was 71.66% ROIP. Oil recovery through the usage of 0.001wt.% zinc oxide (ZnO) nanofluid and electromagnetic waves was 64.26 % ROIP. It is demonstrated that the new electromagnetic water flooding system with nanofluids have potential application in enhanced oil recovery. Therefore, it is concluded that the new electromagnetic system have potential for application in enhanced oil recovery process.

RESEARCH CONTRIBUTIONS

The major contributions of this thesis are:

1. CASTEP simulation shows that the band gap value of ZnO obtained is 0.808ev and for Fe_2O_3, the band gap value is 0.201ev. The percentage difference between the band gap of ZnO and Fe_2O_3 is 301%. For the ZnO band structure, Zn 4s state contributes to conduction band and O 2p state contributes to valence band. As for Fe_2O_3, the valence band is a mixture of O 2p state and a majority of Fe 3d state while the conduction band consists of Fe 3d state.

2. New electromagnetic water flooding system with antenna and nanofluids.

3. Zinc oxide (ZnO) and iron oxide (Fe_2O_3) nanoparticles with particle sizes of 30-39nm and 30.27-37.60nm have been demonstrated as able to improve oil recovery when used in conjunction with electromagnetic waves.

4. The induced electromagnetic field interacts with iron oxide (Fe_2O_3) nanoparticles at 0.001% wt.% to produce 71.66% of ROIP oil recovery.

RECOMENDATIONS

Further works should be carried out in order to improve oil recovery by using nanofluids and antenna:

1. Different metal oxide nanoparticles can be used to achieve higher oil recovery.

2. Different kinds of nanofluids concentration can be experimented to find the optimum values for higher oil recovery.

3. The stability of nanoparticles suspension should be quantitatively analyzed including the effect of temperature and/or pressure on the stability.

4. The improvement in suspension stability would be achieved with the choice of additives and surface coating techniques.

5. Optimized parameters such as nanofluid concentration, EM wave frequency, type and morphology of nanoparticles should be used.

REFERENCES

[1]   K. S. Deffeyes, *Hubbert's peak: the impending world oil shortage*: Princeton Univ Pr, 2008.

[2]   D. B. Reynolds, *Scarcity and Growth Considering Oil and Energy: An Alternative Neo-Classical View*: E. Mellen Press, 2002.

[3]   K. K. Mohanty, "The near-term energy challenge," *AIChE journal,* vol. 49, pp. 2454-2460, 2003.

[4]   R. Hirsch, R. Bezdek, and R. Wendling, "Peaking of world oil production," *in Proceeding of the IV International Workshop on Oil and Gas Depletion,* 2005, pp. 19-20.

[5]   R. Schmidt, "Thermal enhanced oil recovery current status and future needs," *Chemical Engineering Progress;(USA),* vol. 86, 1990.

[6]   B. D. Al-Anazi, "Enhanced Oil Recovery Techniques and Nitrogen Injection," *CSEG Recorder,* pp. 28-33, 2007.

[7]   D. W. Green and G. P. Willhite, *Enhanced oil recovery*: Richardson, Tex.: Henry L. Doherty Memorial Fund of AIME, Society of Petroleum Engineers, 1998.

[8]   E. Rodriguez Pin, M. Roberts, H. Yu, C. Huh, and S. Bryant, "Enhanced Migration of Surface-Treated Nanoparticles in Sedimentary Rocks," in *SPE Annual Technical Conference and Exhibition. Society of Petroleum Engineers*, 2009.

[9]   M. Prodanovic, S. Ryoo, A. R. Rahmani, R. V. Kuranov, C. Kotsmar, T. E. Milner, K. P. Johnston, S.L. Bryant, and C. Huh. "Effects of Magnetic Field on the Motion of Multiphase Fluids Containing Paramagnetic Nanoparticles in Porous Media," in *SPE Improved Oil Recovery Symposium. Society of Petroleum Engineers*, 2010.

[10]   E. Furlani and K. Ng, "Analytical model of magnetic nanoparticle transport and capture in the microvasculature," *Physical review E,* vol. 73, p. 061919, 2006.

[11]   J. E. Bridges, "Optimum antenna-like exciters for heating earth media to recover thermally responsive constituents," U.S. Patent No. 5,293,936, 1994.

[12]   J. Bridges, A. Taflove, and R. Snow, "Method for in situ heat processing of hydrocarbonaceous formations," U.S. Patent No. 4,140,180. 20 1979.

[13]   R. W. P. King, G. S. Smith, M. Owens, and T. Wu, "Antennas in matter: Fundamentals, theory, and applications," *NASA STI/Recon Technical Report A,* vol. 812, p. 29690, 1981.

[14]   D. S. Jones, "Methods in electromagnetic wave propagation," *Chemical Physics,* vol. 1, 1979.

[15]   C. A. Balanis, *Antenna theory: analysis and design*: Harper & Row New York, 1982.

[16]   N. Yahya and T. W. Zhu, "Development Of YFeO Nano-Magnetic Feeder For EM Source Of An Intelligent Horizontal Twin Dipoles," in *International Conference on Nanoscience and Nanotechnology*, 2009, p. 269.

[17]   N. Nasir, N. Yahya, M. N. Akhtar, M. Kashif, A. Shafie, H. Daud, H.M.Zaid, "Magnitude Versus Offset Study with EM Transmitter in Different Resistive Medium," *Journal of Applied Sciences,* vol. 11, pp. 1309-1314, 2011.

[18]   N. Nasir, N. Yahya, M. Kashif, H. Daud, M. N. Akhtar, H. M. Zaid, A.Shafie, L.C.Teng,"Observation of a Cubical-Like Microstructure of Strontium Iron Garnet and Yttrium Iron Garnet Prepared via SolGel Technique," *Journal of Nanoscience and Nanotechnology,* vol. 11, pp. 2551-2554, 2011.

[19]   H. Mohd Zaid, N. Yahya, M. N. Akhtar, M. Kashif, H. Daud, S. Brahim Belhaouari, A.Shafie, M.Hanif, N.H.Hany, A.A.Zorkepli, "1D EM Modeling for Onshore Hydrocarbon Detection Using Matlab," *Journal of Applied Sciences,* vol. 11, pp. 1136-1142, 2011.

[20]   M. N. Akhtar, N. Yahya, and N. Nasir, "Novel EM antenna based on $Y_3Fe_5O_{12}$ magnetic feeders for improved MVO," in *Electronics, Communications and Photonics Conference (SIECPC),* 2011, pp. 1-6.

[21]   V. Benischek, R. Basantkumar, M. Currie, and G. Lyasko, "Electromagnetic Based System And Method For Enhancing Subsurface Recovery Of Fluid Within A Permeable Formation," WO Patent 2,010,022,295, 2010.

[22]   F. E. Parsche, "Triaxial Linear Induction Antenna Array for Increased Heavy Oil Recovery," WO Patent 2,012,067,769, 2012.

[23]   E. C. Donaldson, G. V. Chilingarian, and T. F. Yen, *Enhanced oil recovery, II: Processes and operations*: Elsevier, 1989.

[24] S. A. Shedid, R. Al-Meheideb, and A. Y. Zekri, "Microscopic rock characterization and influence of slug size on oil recovery by CO_2 miscible flooding in carbonate oil reservoir," in *SPE International Improved Oil Recovery Conference in Asia Pacific*, 2005.

[25] Y. Wu, P. J. Shuler, M. Blanco, Y. Tang, and W. A. Goddard, "A study of branched alcohol propoxylate sulfate surfactants for improved oil recovery," in *SPE Annual Technical Conference and Exhibition*, 2005.

[26] A. Sahni, M. Kumar, and R. Knapp, "Electromagnetic heating methods for heavy oil reservoirs," *paper SPE 62550*, 2000.

[27] E. Rangel-German, J. Schembre, C. Sandberg, and A. Kovscek, "Electrical-heating-assisted recovery for heavy oil," *Journal of Petroleum Science and Engineering,* vol. 45, pp. 213-231, 2004.

[28] O. Gizem Gunal and M. Islam, "Alteration of asphaltic crude rheology with electromagnetic and ultrasonic irradiation," *Journal of Petroleum Science and Engineering,* vol. 26, pp. 263-272, 2000.

[29] A. Chhetri and M. Islam, "A critical review of electromagnetic heating for enhanced oil recovery," *Petroleum Science and Technology,* vol. 26, pp. 1619-1631, 2008.

[30] F. Vermeulen and B. McGee, "In-Situ Electromagnetic Heating for Hydrocarbon Recovery and Environmental Remediation," *Journal of Canadian Petroleum Technology,* vol. 39, 2000.

[31] G. Sresty, H. Dev, R. Snow, and J. Bridges, "Recovery of bitumen from tar sand deposits with the radio frequency process," *SPE Reservoir Engineering,* vol. 1, pp. 85-94, 1986.

[32] K. Jha and A. Chakma, "Heavy-oil recovery from thin pay zones by electromagnetic heating," *Energy sources,* vol. 21, pp. 63-73, 1999.

[33] C. Jackson, "Upgrading a heavy oil using variable frequency microwave energy," in *SPE International Thermal Operations and Heavy Oil Symposium and International Horizontal Well Technology Conference. Society of Petroleum Engineers*, 2002.

[34]   M. Kashif, N. Yahya, H. Zaid, A. Shafie, M. Jasamai, N. Nasir, M.N. Akhtar, "Oil Recovery by Using Electromagnetic Waves," *Journal of Applied Sciences,* vol. 11, pp. 1366-1370, 2011.

[35]   E. Abernethy, "Production increase of heavy oils by electromagnetic heating," *Journal of Canadian Petroleum Technology,* vol. 15, 1976.

[36]   J. Fanchi, "Feasibility of reservoir heating by electromagnetic irradiation," in *SPE Annual Technical Conference and Exhibition. Society of Petroleum Engineers*, 1990.

[37]   N. Bjorndalen, S. Mustafiz, and M. Islam, "Numerical modeling of petroleum fluids under microwave irradiation for improved horizontal well performance," *International communications in heat and mass transfer,* vol. 30, pp. 765-774, 2003.

[38]   N. Bjorndalen and M. Islam, "The effect of microwave and ultrasonic irradiation on crude oil during production with a horizontal well," *Journal of Petroleum Science and Engineering,* vol. 43, pp. 139-150, 2004.

[39]   M. Soliman, "Approximate solutions for flow of oil heated using microwaves," *Journal of Petroleum Science and Engineering,* vol. 18, pp. 93-100, 1997.

[40]   M. Islam and A. Chakma, "A new recovery technique for heavy-oil reservoirs with bottomwater," *SPE Reservoir Engineering,* vol. 7, pp. 180-186, 1992.

[41]   M. R. Islam and A. Chakma, "New Concepts of Combining Electromagnetic Heating with Horizontal Wells," in *13th World Petroleum Congress*, 1991.

[42]   M. Carrizales, L. Lake, and R. Johns, "Multiphase Fluid Flow Simulation of Heavy Oil Recovery by Electromagnetic Heating," in *SPE Improved Oil Recovery Symposium. Society of Petroleum Engineers*, 2010.

[43]   R. Kasevich, S. Price, D. Faust, and M. Fontaine, "Pilot testing of a radio frequency heating system for enhanced oil recovery from diatomaceous earth," in *SPE Annual Technical Conference and Exhibition. Society of Petroleum Engineers*, 1994.

[44]   J. Pizarro and O. Trevisan, "Electrical heating of oil reservoirs: numerical simulation and field test results," *Journal of Petroleum Technology,* vol. 42, pp. 1320-1326, 1990.

[45] J. Bridges, J. Krstansky, A. Taflove, and G. Sresty, "The IITRI In Situ RF Fuel Recovery Process," *Journal of Microwave Power,* vol. 18, p. 1, 1983.

[46] P. Zhang, A. Kan, C. Fan, S. Work, H. Lu, J. Yu, H. Al-Saiari, M. B. Tomson."Silica-templated synthesis of novel zinc-DTPMP nanoparticles, their transport in carbonate and sandstone porous media and scale inhibition," in *SPE International Conference on Oilfield Scale. Society of Petroleum Engineers*, 2010.

[47] H. Yu, C. Kotsmar, K. Y. Yoon, D. R. Ingram, K. Johnston, S. Bryant, C. Huh"Transport and retention of aqueous dispersions of paramagnetic nanoparticles in reservoir rocks," in *SPE Improved Oil Recovery Symposium. Society of Petroleum Engineers*, 2010.

[48] T. Zhang, D. Davidson, S. Bryant, and C. Huh, "Nanoparticle-Stabilized Emulsions for Applications in Enhanced Oil Recovery," in *SPE Improved Oil Recovery Symposium. Society of Petroleum Engineers*, 2010.

[49] N. Al-Manasir, A. L. Kjøniksen, and B. Nyström, "Preparation and characterization of cross-linked polymeric nanoparticles for enhanced oil recovery applications," *Journal of Applied Polymer Science,* vol. 113, pp. 1916-1924, 2009.

[50] B. Ju, T. Fan, and M. Ma, "Enhanced oil recovery by flooding with hydrophilic nanoparticles," *China Particuology,* vol. 4, pp. 41-46, 2006.

[51] B. Ju and T. Fan, "Experimental study and mathematical model of nanoparticle transport in porous media," *Powder Technology,* vol. 192, pp. 195-202, 2009.

[52] S. Chol, "Enhancing thermal conductivity of fluids with nanoparticles," *ASME-Publications-FED,* vol. 231, pp. 99-106, 1995.

[53] S. P. Jang and S. U. S. Choi, "Role of Brownian motion in the enhanced thermal conductivity of nanofluids," *Applied Physics Letters,* vol. 84, p. 4316, 2004.

[54] C. H. Chon, K. D. Kihm, S. P. Lee, and S. U. S. Choi, "Empirical correlation finding the role of temperature and particle size for nanofluid (Al_2O_3) thermal conductivity enhancement," *Applied Physics Letters,* vol. 87, p. 153107, 2005.

[55] R. K. Neogy and A. Raychaudhuri, "Frequency dependent enhancement of heat transport in a nanofluid with ZnO nanoparticles," *Nanotechnology,* vol. 20, p. 305706, 2009.

[56] S. Ferrouillat, A. Bontemps, O. Poncelet, O. S. Gruss, and JA, "Influence of Nanoparticle Shape Factor on Convective Heat Transfer of Water-Based ZnO Nanofluids. Performance Evaluation Criterion," *International Journal of Mechanical and Industrial Engineering,* vol. 1, pp. 7-13, 2011

[57] H. T. Zhu, C. Y. Zhang, Y. M. Tang, and J. X. Wang, "Novel synthesis and thermal conductivity of CuO nanofluid," *The Journal of Physical Chemistry C,* vol. 111, pp. 1646-1650, 2007.

[58] N. Karthikeyan, J. Philip, and B. Raj, "Effect of clustering on the thermal conductivity of nanofluids," *Materials Chemistry and Physics,* vol. 109, pp. 50-55, 2008.

[59] H. Xie, J. Wang, T. Xi, Y. Liu, F. Ai, and Q. Wu, "Thermal conductivity enhancement of suspensions containing nanosized alumina particles," *Journal of Applied Physics,* vol. 91, pp. 4568-4572, 2002.

[60] L. Colla, L. Fedele, M. Scattolini, and S. Bobbo, "Water-Based Fe_2O_3 Nanofluid Characterization: Thermal Conductivity and Viscosity Measurements and Correlation," *Advances in Mechanical Engineering,* vol. 2012, 2011.

[61] P. Shima, J. Philip, and B. Raj, "Synthesis of aqueous and nonaqueous iron oxide nanofluids and study of temperature dependence on thermal conductivity and viscosity," *The Journal of Physical Chemistry C,* vol. 114, pp. 18825-18833, 2010.

[62] J. R. Hook and H. E. Hall, "Solid State Physics (The Manchester Physics Series)," ed: John Wiley and Sons Ltd, 2000.

[63] C. Kittel and P. McEuen, *Introduction to solid state physics* vol. 8: Wiley New York, 1986.

[64] N. W. Ashcroft and N. D. Mermin, "Solid State Phys," *Saunders, Philadelphia,* 1976.

[65] J. M. Ziman, *Principles of the Theory of Solids*: Cambridge university press, 1972.

[66] M. Omar, "Elementary Solid State Physics: Principles and Applications. 1993," ed: New York: Addison-Wesley.

[67] H. Ibach and H. Luth, "Solid-State Physics. 1993," ed: Springer-Verlag, New York.

[68] A. P. Sutton, *Electronic structure of materials*: Oxford University Press, 1993.

[69] Y. Dai, Y. Zhang, and Z. L. Wang, "The octa-twin tetraleg ZnO nanostructures," *Solid State Communications,* vol. 126, pp. 629-633, 2003.

[70] J. Sun, Y. Lu, Y. Liu, D. Shen, Z. Zhang, B. Li, J. Y. Zhang, B. Yao, D. X. Zhao, X. W. Fan, "Excitonic electroluminescence from ZnO-based heterojunction light emitting diodes," *Journal of Physics D: Applied Physics,* vol. 41, p. 155103, 2008.

[71] Z. Wang, "Novel nanostructures of ZnO for nanoscale photonics, optoelectronics, piezoelectricity, and sensing," *Applied Physics A,* vol. 88, pp. 7-15, 2007.

[72] N. Hasuike, K. Nishio, H. Katoh, A. Suzuki, T. Isshiki, K. Kisoda, H. Harima, "Structural and electronic properties of ZnO polycrystals doped with Co," *Journal of Physics: Condensed Matter,* vol. 21, p. 064215, 2009.

[73] C. Jia, Y. Chen, G. Liu, X. Liu, S. Yang, and Z. Wang, "Structural and optical properties of ZnO films on SrTiO3 substrates by MOCVD," *Journal of Physics D: Applied Physics,* vol. 42, p. 015415, 2009.

[74] M. Aronniemi, J. Lahtinen, and P. Hautojärvi, "Characterization of iron oxide thin films," *Surface and interface analysis,* vol. 36, pp. 1004-1006, 2004.

[75] U. Schwertmann and R. M. Cornell, *Iron oxides in the laboratory: preparation and characterization*: John Wiley & Sons, 2008.

[76] R. M. Cornell and U. Schwertmann, *The iron oxides: structure, properties, reactions, occurrences and uses*: John Wiley & Sons, 2003.

[77] L. Machala, J. Tucek, and R. Zboril, "Polymorphous transformations of nanometric iron (III) oxide: a review," *Chemistry of Materials,* vol. 23, pp. 3255-3272, 2011.

[78] (20 April). Available:
http://www.geocities.jp/ohba_lab_ob_page/Structure/Hematite bond.JPG

[79] M. Getzlaff, *Fundamentals of magnetism*: Springer Verlag, 2008.

[80] D. Jiles, *Introduction to magnetism and magnetic materials*: CRC, 1998.

[81] S. Chikazumi and C. D. Graham, *Physics of ferromagnetism* vol. 94: Oxford University Press, USA, 1997.

[82] K. Sahay, S. Pathak, and K. Sahay, *Basic concepts of electrical engineering*: New Age International, 2006.

[83] H. Warad, S. Ghosh, B. Hemtanon, C. Thanachayanont, and J. Dutta, "Luminescent nanoparticles of Mn doped ZnS passivated with sodium hexametaphosphate," *Science and Technology of Advanced Materials,* vol. 6, pp. 296-301, 2005.

[84] H. Rensmo, A. Ongaro, D. Ryan, and D. Fitzmaurice, "Self-assembly of alkane capped silver and silica nanoparticles," *J. Mater. Chem.,* vol. 12, pp. 2762-2768, 2002.

[85] T. Pal, T. K. Sau, and N. R. Jana, "Reversible formation and dissolution of silver nanoparticles in aqueous surfactant media," *Langmuir,* vol. 13, pp. 1481-1485, 1997.

[86] J. D. Aiken III and R. G. Finke, "A review of modern transition-metal nanoclusters: their synthesis, characterization, and applications in catalysis," *Journal of Molecular Catalysis A: Chemical,* vol. 145, pp. 1-44, 1999.

[87] M. Malmsten, *Surfactants and polymers in drug delivery*: Marcel Dekker New York, 2002.

[88] D. Karsa, "Surfactants in polymers, coatings, inks and adhesives (Applied surfactant series, vol. 1)," 2003.

[89] K. Holmberg, *Novel surfactants: preparation, applications, and biodegradability* vol. 114: CRC, 2003.

[90] P. Mukerjee, "Critical micelle concentrations of aqueous surfactant systems," DTIC Document1971.

[91] M. Egermayer, J. Norrman, and L. Piculell, "Gels of hydrophobically modified hydroxyethyl cellulose cross-linked by amylose: Competition by added surfactants," *Langmuir,* vol. 19, pp. 10036-10043, 2003.

[92] E. Abuin, E. Lissi, and C. Borsarelli, "Tl+/Na+ Competitive Binding at the Surface of Dodecylsulfate Micelles in Water-Urea Mixtures," *Journal of colloid and interface science,* vol. 184, pp. 652-657, 1996.

[93] T. Al-Sahhaf, A. S. Ahmed, and A. Elkamel, "Producing ultralow interfacial tension at the oil/water interface," *Petroleum Science and Technology,* vol. 20, pp. 773-788, 2002.

[94]   A. Y. Dandekar, *Petroleum reservoir rock and fluid properties*: CRC, 2006.

[95]   J. Drelich, C. Fang, and C. White, "Measurement of interfacial tension in fluid-fluid systems," *Encyclopedia of Surface and Colloid Science,* pp. 3152-3166, 2002.

[96]   N. T. Nguyen, A. Beyzavi, K. M. Ng, and X. Huang, "Kinematics and deformation of ferrofluid droplets under magnetic actuation," *Microfluidics and Nanofluidics,* vol. 3, pp. 571-579, 2007.

[97]   F. Ikazaki, A. Kawai, K. Uchida, T. Kawakami, K. Edamura, K. Sakurai*, et al.*, "Mechanisms of electrorheology: the effect of the dielectric property," *Journal of Physics D: Applied Physics,* vol. 31, p. 336, 1998.

[98]   H. Block, J. Kelly, A. Qin, and T. Watson, "Materials and mechanisms in electrorheology," *Langmuir,* vol. 6, pp. 6-14, 1990.

[99]   P. Atten, J. Foulc, and N. Felici, "A conduction model of the electrorheological effect," *International Journal of Modern Physics B,* vol. 8, pp. 2731-2746, 1994.

[100]   C. Wu and H. Conrad, "A modified conduction model for the electrorheological effect," *Journal of Physics D: Applied Physics,* vol. 29, p. 3147, 1996.

[101]   T. Hao, A. Kawai, and F. Ikazaki, "Mechanism of the electrorheological effect: evidence from the conductive, dielectric, and surface characteristics of water-free electrorheological fluids," *Langmuir,* vol. 14, pp. 1256-1262, 1998.

[102]   J. N. Foulc, P. Atten, and N. Felici, "Macroscopic model of interaction between particles in an electrorheological fluid," *Journal of electrostatics,* vol. 33, pp. 103-112, 1994.

[103]   Y. Lan, S. Men, X. Xu, and K. Lu, "Experimental study of dielectric constant influence on electrorheological effect," *Journal of Physics D: Applied Physics,* vol. 33, p. 1239, 2000.

[104]   H. Ma, W. Wen, W. Y. Tam, and P. Sheng, "Dielectric electrorheological fluids: theory and experiment," *Advances in physics,* vol. 52, pp. 343-383, 2003.

[105]   L. Rejon, I. Castaņeda-Aranda, and O. Manero, "Rheological behavior of electrorheological fluids: effect of the dielectric properties of liquid phase," *Colloids and Surfaces A: Physicochemical and Engineering Aspects,* vol. 182, pp. 93-107, 2001.

[106]   T. B. Jones, *Electromechanics of particles*: Cambridge Univ Pr, 2005.

144

[107] J. A. Kong, "Theory of electromagnetic waves," *New York, Wiley-Interscience, 1975. 348 p.,* vol. 1, 1975.

[108] D. J. Griffiths and R. College, *Introduction to electrodynamics* vol. 3: prentice Hall New Jersey:, 1999.

[109] F. T. Ulaby, *Electromagnetics for engineers*: Upper Saddle River, 2005.

[110] J. A. Stratton, *Electromagnetic theory* vol. 33: Wiley-IEEE Press, 2007.

[111] D. K. Cheng, "Field and Wave Electromagnetics, 1989," ed: Addison-Wesley, Reading, Massachusetts.

[112] N. Ida, *Engineering electromagnetics*: Springer Verlag, 2004.

[113] J. P. Perdew, K. Burke, and M. Ernzerhof, "Generalized gradient approximation made simple," *Physical review letters,* vol. 77, p. 3865, 1996.

[114] M. Segall, P. J. Lindan, M. Probert, C. Pickard, P. Hasnip, S. Clark, M. C. Payne, "First-principles simulation: ideas, illustrations and the CASTEP code," *Journal of Physics: Condensed Matter,* vol. 14, p. 2717, 2002.

[115] S. J. Clark, M. D. Segall, C. J. Pickard, P. J. Hasnip, M. I. Probert, K. Refson*, M. C. Payne, "First principles methods using CASTEP," *Zeitschrift für Kristallographie,* vol. 220, pp. 567-570, 2005.

[116] X. Wang, X. Chen, R. Dong, Y. Huang, and W. Lu, "Ferromagnetism in carbon-doped ZnO films from first-principle study," *Physics Letters A,* vol. 373, pp. 3091-3096, 2009.

[117] M. C. Payne, M. P. Teter, D. C. Allan, T. Arias, and J. Joannopoulos, "Iterative minimization techniques for ab initio total-energy calculations: molecular dynamics and conjugate gradients," *Reviews of Modern Physics,* vol. 64, pp. 1045-1097, 1992.

[118] D. Vanderbilt, "Soft self-consistent pseudopotentials in a generalized eigenvalue formalism," *Physical Review B,* vol. 41, p. 7892, 1990.

[119] D. Ceperley and B. Alder, "Exchange-correlation potential and energy for density-functional calculation," *Phys. Rev. Lett,* vol. 45, pp. 567-581, 1980.

[120] H. J. Monkhorst and J. D. Pack, "Special points for Brillouin-zone integrations," *Physical Review B,* vol. 13, pp. 5188-5192, 1976.

[121] B. D. Cullity and S. R. Stock, *Elements of X-ray Diffraction* vol. 3: Prentice Hall Upper Saddle River, NJ, 2001.

[122] R. Resnick, D. Halliday, and J. Walker, "Fundamentals of physics," *John Wiley & Sons, New York, Part,* vol. 1, p. 16, 2004.

[123] P. Naik, *Principles of Physics*: PHI Learning Pvt. Ltd., 2010.

[124] M. De Graef and M. E. McHenry, *Structure of materials: an introduction to crystallography, diffraction and symmetry*: Cambridge University Press, 2007.

[125] (15 May). *Scanning Electron Microscope*. Available: http://www.purdue.edu/rem/rs/sem.htm

[126] W. Zhou and Z. L. Wang, *Scanning microscopy for nanotechnology: techniques and applications*: Springer Verlag, 2007.

[127] J. Goldstein, *Scanning electron microscopy and X-ray microanalysis* vol. 1: Springer Us, 2003.

[128] A. R. Clarke and C. N. Eberhardt, *Microscopy techniques for materials science*: Woodhead Publishing, 2002.

[129] R. F. Egerton, *Physical principles of electron microscopy: an introduction to TEM, SEM, and AEM*: Springer, 2005.

[130] S. Amelinckx, D. van Dyck, J. van Landuyt, and G. van Tendeloo, *Electron microscopy: principles and fundamentals*: Weinheim, 1997.

[131] J. Mayer, L. A. Giannuzzi, T. Kamino, and J. Michael, "TEM sample preparation and FIB-induced damage," *Mrs Bulletin,* vol. 32, pp. 400-407, 2007.

[132] C. R. Brundle, C. A. Evans, and S. Wilson, *Encyclopedia of materials characterization: surfaces, interfaces, thin films*: Gulf Professional Publishing, 1992.

[133] J. M. Thomas and C. Ducati, *Transmission electron microscopy*: Wiley Online Library, 1979.

[134] L. Reimer and H. Kohl, *Transmission electron microscopy: physics of image formation* vol. 36: Springer, 2008.

[135] Y. H. Yu, S. C. Lee, C. S. Yang, C. K. Choi, And W. K. Jung, "Mobility, energy gap and dielectric constant in SiOC films," *Journal of the Korean Physical Society,* vol. 42, pp. 682-685, 2003.

[136] H. Huff and D. Gilmer, *High dielectric constant materials: VLSI MOSFET applications* vol. 16: Springer, 2006.

[137] D. Sridev and K. Rajendran, "Synthesis and optical characteristics of ZnO nanocrystals," *Bulletin of Materials Science,* vol. 32, pp. 165-168, 2009.

[138] K. S. Babu and V. Narayanan, "Hydrothermal Synthesis of Hydrated Zinc Oxide Nanoparticles and its Characterization," *Chemical Science Transactions* vol. 2, pp. S33-S36, 2013.

[139] M. Joya, J. Barón-Jaimez, and J. Barba-Ortega, "Preparation and characterization of Fe_2O_3 nanoparticles," in *Journal of Physics: Conference Series*, 2013, p. 012004.

[140] S. Kutuzov, J. He, R. Tangirala, T. Emrick, T. Russell, and A. Böker, "On the kinetics of nanoparticle self-assembly at liquid/liquid interfaces," *Physical Chemistry Chemical Physics,* vol. 9, pp. 6351-6358, 2007.

PUBLICATIONS

1. Noorhana Yahya, **Muhammad Kashif**, Afza Shafie, Hassan Solemani, Hasnah M Zaid and Noor Rasyada Ahmad Latiff "Improved Oil Recovery by High Magnetic Flux Density Subjected to Iron Oxide Nanofluids" Journal of Nano Research 26 (2014): 89-99.

2. Afza Shafie, Noorhana Yahya, **Muhammad Kashif**, Hasnah M Zaid, Hassan Solemani,and Mohamed Narabijy, "The Band Structures of Single-Walled Carbon Nanotubes (SWCNTs) and ZnO Nanoparticles used for Oil Recovery in Water Flooding System" Journal of Nano Research 26 (2014): 101-110.

3. Nasir, N., Yahya, N. Akhtar, M.N., **Kashif,M.**"Antenna for offshore hydrocarbon exploration." Electronics, Communications and Photonics Conference. Saudi International. 2013. (SIECPC 2013) 27-30 April 2013, Riyadh, Saudi Arabia. (DOI=10.1109/SIECPC.2013.6550767)

4. **Muhammad Kashif**, Noorhana Yahya, Nadeem Nasir, Majid Niaz Akhtar, Hasnah Mohd Zaid, Afza Shafie"Full Scale Modeling of an Antenna in Offshore Environment for Electromagnetic Enhanced Oil Recovery" AIP Conf. Proc. 1482, 164 (2012); International Conference On Fundamental And Applied Sciences 2012: (ICFAS2012)

5. Majid Niaz Akhtar, Noorhana Yahya, Afza Shafie, Nadeem Nasir, **Muhammad Kashif**, and Hasnah Mohd Zaid "Development of novel electromagnetic antenna for deep target marine CSEM survey" AIP Conf. Proc. 1482, pp. 157-163; International Conference On Fundamental And Applied Sciences 2012: (ICFAS2012)

6. Noorhana Yahya, Nadeem Nasir, Majid Niaz Akhtar, **Muhammad Kashif**, Tanvir Hussain, Hasnah Mohd Zaid, Afza Shafie "Electromagnetic Response Studies of the Antenna for Deep Water Deep Target CSEM Environments" Journal of Electromagnetic Analysis and Applications, 2012, 4, 513-522

7. Noorhana Yahya, **Muhammad Kashif**, Nadeem Nasir, Majid Niaz Akhtar "Cobalt Ferrite Nanoparticles An Innovative Approach for Enhanced Oil Recovery Application" 2012, Journal of Nano Research, 17, 115

8. Noorhana Yahya, Nadeem Nasir, Majid Niaz Akhtar, **Muhammad Kashif**, Hasnah Mohd Zaid, Afza Shafie "Modeling of Antenna for Deep Target Hydrocarbon Exploration" Journal of Electromagnetic Analysis and Applications, 4, 30-41, 2012.

9. Noorhana Yahya, Majid Niaz Akhtar, Nadeem Nasir, **Muhammad Kashif**, Hasnah Mohd Zaid, Afza Shafie "Guided and Direct Wave Evaluation of Controlled Source Electromagnetic Survey Using Finite Element Method" Journal of Electromagnetic Analysis and Applications, Vol.4 No.3, March, 2012

10. **Muhammad Kashif**, Noorhana Yahya, Nadeem Nasir, Majid Niaz Akhtar "Experimental Study of Electromagnetic Waves Affects on Enhanced Oil Recovery" 19-20 September 2011, National Postgraduate Conference (NPC),Universiti Teknologi PETRONAS, IEEE Xplore Conference Proceeding (DOI= 10.1109/NatPC.2011.6136434)

11. Majid Niaz Akhtar, Noorhana Yahya, Nadeem Nasir and **Muhammad Kashif**, "Synthesis and Characterizations of $Y_3Fe_5O_{12}$-MWCNTs composites for SBL application" 19-20 September 2011, National Postgraduate Conference (NPC),Universiti Teknologi PETRONAS, IEEE Xplore Conference Proceeding (DOI= 10.1109/NatPC.2011.6136451)

12. Nadeem Nasir, Noorhana Yahya, Majid Niaz Akhtar and **Muhammad Kashif**, "MVO Study of Antenna for Deep Target Hydrocarbon Exploration" 19-20 September 2011, National Postgraduate Conference (NPC),Universiti Teknologi PETRONAS, IEEE Xplore Conference Proceeding (DOI=10.1109/NatPC.2011.6136452)

13. **Muhammad Kashif**, Noorhana Yahya, Hasnah Mohd Zaid, Afza Shafie, Mazuin Jasamai, Nadeem Nasir, Majid Niaz Akhter, "Oil Recovery by Using Electromagnetic waves" Journal of Applied Sciences, vol 1, 2011.

14. Nadeem Nasir, Noorhana Yahya, Majid Niaz Akhtar, **Muhammad Kashif**, Afza Shafie,Hanita Daud, Hasnah Mohd Zaid Magnitude Verses Offset (MVO) Study with EM Transmitter in Different Resistive Medium, Journal of Applied Sciences, vol 1, 2011.

15. Majid Niaz Akhtar, Noorhana Yahya, Hanita Daud, Afza Shafie, Hasnah Mohd Zaid, **Muhammad Kashif**, Nadeem Nasir,"Development of EM wave guide amplifier potentially used for sea bed logging (SBL), Journal of Applied Sciences, vol 1, 2011)

16. Hasnah Mohd Zaid, Noorhana Yahya, Majid Niaz Akhtar, **M.Kashif**, Hanita Daud et.al, "1D EM modelling for onshore hydrocarbon detection using Matlab", Journal of Applied Sciences, Vol 11, 1136-1142, 2011.

17. Noorhana Yahya, Majid Niaz Akhtar, A.F.Masuri and **M.Kashif**," Synthesis and Characterization of ZnO-CNTs Filled PVA Composite as EM Detector" Journal of Applied Sciences, vol 11, 1303-1308, 2011.

18. Nadeem Nasir, Noorhana yahya, **Muhammad Kashif**, Hanita Daud, Majid Niaz Akhtar, Hasnah Mohd Zaid, Afza Shafie, and Lee Cha Teng Observation of a Cubical-Like Microstructure of Strontium Iron Garnet and Yttrium Iron Garnet Prepared via Sol–Gel Technique, Journal of Nanoscience and Nanotechnology, Vol. 10. 1-4, 2010

19. Noorhana Yahya, Ramadan Masoud Al Habashi, Krzysztof Koziol, Rafal Dunin Borkowski, Majid Niaz Akhtar, **Muhammad Kashif**, and Mansor Hashim, Morphology and Magnetic Characterisation of Aluminium Substituted Yttrium-Iron Garnet Nanoparticles Prepared Using Sol Gel Technique,"Journal of Nanoscience and Nanotechnology, Vol. 10. 1-5, 2010

20. Noorhana Yahya, **Muhammad Kashif**, Hanita Daud, Hasnah Mohd Zaid, Afza Shafie,Nadeem Nasir, and Alex See Fabrication and Characterization of $Y_{3.0-x}La_xFe_5O_{12}$ - PVA Composite as EM Waves Detector International Journal of Basic & Applied Sciences IJBAS Vol: 9 No: 9 131-134 (2009)

21. Noorhana Yahya, **Muhammad Kashif**, Hanita Daud, Nadeem Nasir, Maryam Shafri Jebeli, Hasnah Mohd Zaid, Afza Shafie and Tah Lee Teng, A Comparative Study of Yttrium Iron Garnet ($Y_3Fe_5O_{12}$) Prepared Using Sol-Gel, Mechanical Alloying and Conventional Techniques, 4th International Conference on Recent Advances in Materials, Minerals Environment and 2nd Asian Symposium on Materials and Processing (2009)

BOOK CHAPTER:

Muhammad Kashif, Majid Niaz Akhtar, Nadeem Nasir, and Noorhana Yahya, "Versatility of ZnO Nanostructures" Adv Struct Mater, DOI 10.1007/8611, Springer Verlag Berlin Heidelberg (2011)

APPENDIX A

NANOPARTICLES SYNTHESIZES CALCULATIONS

Zinc Oxide Nanoparticles

Zinc oxide nanoparticles are synthesized by using zinc nitrate hexahydrate, $Zn(NO_3)_2.6H_2O$ as starting material and 65% nitric acid. The calculation for the synthesizing the ZnO is based on the molecular weight for zinc nitrate hexahydrate.

The calculation is shown below:

Molecular weight of zinc nitrate hexahydrate, $Zn(NO_3)_2.6H_2O$

Molecular weight of $Zn(NO_3)_2.6H_2O = 297.48$ g

Molecular weight of zinc nitrate, $Zn(NO_3)_2$,

Molecular weight of $Zn(NO_3)_2 = 189.39$ g

In order to prepare 10 g of zinc oxide nanopowders, the estimated amount of zinc nitrate hexahydrate required as starting material is calculated by using the formula given:

$$\text{Amount of zinc nitrate hexahydrate} = \frac{\text{Molecular weight of zinc nitrate hexahydrate}}{\text{Molecular weight of zinc nitrate}} \times \text{Amount of Zinc Oxide to be synthesize}$$

$$\text{Amount of Zinc Nitrate Hexahydrate} = \frac{297.48g}{189.39g} \times 10g$$
$$= 15.70 \text{ g}$$

Amount of 65% nitric acid (HNO_3) that needs to be used to prepare 10g of zinc oxide nanoparticles is five times the amount of zinc nitrate hexahydrate.

$$\text{Amount of 65\% Nitric Acid} = 15.70 \times 5 ml$$
$$= 78.5 ml$$

By using the formula above, the estimated amount of zinc nitrate hexahydrate and 65% nitric acid to be used to produce 10 g of zinc oxide nanopowders are 15.70 g and 78.5 mL respectively.

Iron Oxide (Fe₂O₃) Nanoparticles

Iron oxide (Fe_2O_3) nanoparticles are synthesized by using iron nitrate ($Fe(NO_3)_3$ $9H_2O$) as starting material and 65% nitric acid. The calculation for the synthesizing the iron oxide (Fe_2O_3) is based on the molecular weight for iron nitrate ($Fe(NO_3)_3$ $9H_2O$).

The calculation is shown below:

Molecular weight of Iron nitrate ($Fe(NO_3)_3$ $9H_2O$).,

Molecular weight of $Fe(NO_3)_3$ $9H_2O$ = 404g

Molecular weight of iron nitrate $Fe(NO_3)_3$,

Molecular weight of iron nitrate $Fe(NO_3)_3$ = 241.86 g

In order to prepare 10 g of iron oxide (Fe_2O_3) nanopowders, the estimated amount of iron nitrate ($Fe(NO_3)_3$ $9H_2O$) required as starting material is calculated by using the formula given:

$$\text{Amount of Iron nitrate } \left(Fe(NO_3)_3 \, 9H_2O\right) = \frac{\text{Molecular weight of Iron nitrate } \left(Fe(NO_3)_3 \, 9H_2O\right)}{\text{Molecular weight of Iron nitrate}} \times \text{Amount of Iron oxide } (Fe_2O_3) \text{ to be synthesize}$$

$$\text{Amount of Iron nitrate } \left(Fe(NO_3)_3 \, 9H_2O\right) = \frac{404g}{241.86g} \times 10g$$
$$= 16.70g$$

Amount of 65% nitric acid (HNO_3) that needs to be used to prepare 10g of iron oxide (Fe_2O_3)nanoparticles is five times the amount of Iron nitrate ($Fe(NO_3)_3$ $9H_2O$).

$$\text{Amount of 65\% Nitric Acid} = 16.70 \times 5ml$$
$$= 83.5ml$$

By using the formula above, the estimated amount of iron nitrate ($Fe(NO_3)_3$ $9H_2O$) and 65% nitric acid to be used to produce 10 g of iron oxide (Fe_2O_3) nanopowders are 16.70 g and 83.5 mL respectively.